Near-Field Microwave Tomography Systems and the Use of a Scatterer Probe Technique

by

Majid Ostadrahimi

A Thesis submitted to the Faculty of Graduate Studies of

The University of Manitoba

in partial fulfilment of the requirements of the degree of

DOCTOR OF PHILOSOPHY

Department of Electrical and Computer Engineering

University of Manitoba

Winnipeg, Manitoba, Canada

ABSTRACT

This dissertation presents the contributions and the research conducted in developing and implementing Microwave Tomography (MWT) systems. MWT is an imaging modality which aims to interrogate an object of interest by microwave energy, and quantitatively "find" the interior spatial distribution of its dielectric properties using field measurements taken outside the object. Due to the inherent non-linearity of the MWT problem, a substantial amount of electromagnetic scattering data is required to ensure a robust inversion and quantitatively accurate imaging results. This research benefits a variety of applications including biomedical imaging, industrial non-destructive testing, and security applications.

Developing a MWT system, requires many critical components including the bandwidth and polarization purity of the collected fields as well as calibration of the fields scattered by the object of interest. Two generations of MWT systems were designed, implemented, calibrated and tested at the University of Manitoba (UM). These systems aim different approaches for near-field measurements which are referred to as the direct and indirect methods.

With regard to the antenna design, a novel methodology applicable to broadband planar antennas is introduced. This technique is based on a combination of field modelling, herein, the finite element method and transmission line modelling. In the first generation of the UM MWT systems, a suitable antenna system was utilized. The system under study was a prototype, where twenty-four co-resident antennas encircle the object of interest to directly measure the fields.

In the second generation of the UM MWT systems, the feasibility of using a novel technique to indirectly measure the fields by a secondary array of near-field scatterer probes was studied. The technique is based on the Modulated Scatterer Technique (MST). In this system, antennas are called "collectors", since the role of antennas are changed to collecting probes' scattered fields. A number of PIN diodes were utilized to activate the probes.

Finally, the capability of the probe system was investigated and its performance with the previously constructed tomography systems was compared. Various dielectric phantoms were utilized to test the accuracy of the systems.

CONTRIBUTIONS

This thesis outlines the implementation of microwave tomography systems at the University of Manitoba. As a member of the University of Manitoba imaging group, the author has collaborated with other colleagues to accomplish the contributions listed here. My colleagues' contributions to this work are identified. The relevant results of these contributions are published or submitted for publications as listed in appendix C.

- Designing, fabricating and measuring several antenna structures and comparing with theoretical results. Introducing a novel technique for designing broadband, low cross-polarized planar antennas by utilizing combination of the finite element method for field modeling and transmission line theory.

- Implementing a 24-element broadband air-based microwave tomography system, where co-resident antennas are located in a circular configuration. These co-resident antennas and the imaging domain are in the near-field region. The data acquisition program for this system was developed by Mr. Cameron Jon Kaye and Mr. Amer Zakaria. Inversion algorithms were developed by Dr. Puyan Mojabi and Dr. Colin Gilmore.

- Introducing a novel method to determine particular frequencies with the weakest mutual coupling between co-resident antennas. This method provides some information on possible *well-behaved* imaging frequencies with the highest chance of successful image reconstruction.

- Introducing a novel tomography system based on the concept of scatterer probe technique. This system includes an array of collector antennas in conjunction with near-field probes encircling the object of interest.

- Designing, simulating and optimizing near-field scatterer probes for minimum interference when used in a tomography system.

- Designing and implementing a tomography system with an equal number of probes and collectors as well as one with a greater number of probes as compared to collectors. Developing a data acquisition program to control the collectors and probes. A successful image reconstruction of different objects was achieved with this system. The inversion task was performed by Dr. Puyan Mojabi.

- Studying of the modeling error incurred when using 2D TM inversions with these systems. Fully simulating the free-space tomography system in order to compute an accurate incident field. Applying different calibration techniques to the measured data and comparing the inversion results. The inversion task was performed by Dr. Puyan Mojabi.

ACKNOWLEDGMENTS

If I have seen further it is only by standing on the shoulders of giants.
(Isaac Newton [1])

First and foremost, I would like to thank Prof. Sima Noghanian and Prof. Joe LoVetri for their continuous advice, guidance, and valuable suggestions which led me to achieve a better understanding of my research, and main contributions of this doctoral work. I am very thankful to Prof. Lotfollah Shafai, and Prof. Stephen Pistorius for their support, encouragement and insightful reviews and comments.

I also would like to thank Prof. Jean-Jacques Laurin, the external examiner, for reviewing the thesis in great details.

One of my most unique opportunities was to work with fellow colleagues at the University of Manitoba and I would like to thank all of the students and technical staff for their friendly support. Among my colleagues, I am especially grateful to Dr. Puyan Mojabi, Dr. Colin Gilmore, Amer Zakaria, Cameron Kaye, Dr. Ian Jeffrey, Gabriel Faucher, Abas Sabouni, Arman Vahedi, and Dr. Alireza Foroozesh, and among the University of Manitoba staff, Shelly Girardin, Brad Tabachnick, Cory Smit, Amy Dario, Judy Noble, Sinisa Janjic, Zoran Trajkoski, Mount-First Ng, and Alan McKay.

I am also very grateful for financial supports received from CancerCare Manitoba, Manitoba Hydro, Natural Sciences and Engineering Research Council of Canada (NSERC), Mathematics of Information Technology and Complex Systems (MITACS), the University of Manitoba (Graduate Fellowship, UMGF), and the Manitoba Ministry of Advanced Education and Literacy (Manitoba Graduate Scholarship, MGS).

I would like to express my heartfelt thanks to Saeed, Omid, Matineh and my parents, who have done everything for me. My parents' love and blessings have always been an important part of my life and they made it possible for me to start this journey. Last, but not least, my deepest and sincere appreciation goes to my eternal companion and angel, Faezeh, for her love, kindness, gentleness, help, and continued encouragements during this work.

Majid Ostadrahimi

Table of Contents

List of Figures

Notation and Acronyms

Throughout this thesis the IEEE style for bibliography and when citing references is used. Scaler variables are denoted by lower case *italic* letters. Capital letters are used to denote the phasor form of electromagnetic fields. A matrix or a set of variables are denoted by underline. Vectors are denoted by **bold** letters.

Symbol	**Description**
$\mathbf{r}$	Position vector.
$\mathbb{R}$	Set of real numbers.
$\mathbb{C}$	Set of complex numbers.
$\mathcal{D}$	Imaging domain.
$\mathcal{S}$	Measurement domain.
ϵ_0	Dielectric permittivity of free-space: $\frac{1}{36\pi} \times 10^{-9}$ (F/m).
ϵ_r	Relative complex permittivity of the OI.
ϵ_b	Relative complex permittivity of the background medium.
μ_0	Permeability of free-space: $4\pi \times 10^{-7}$ (H/m).
f	Frequency (Hz).
ω	Radial frequency: $2\pi f$ (rad/s).
k	Wavenumber: $k^2 = w^2\mu\epsilon$.
k_b or k_0	Wavenumber of the background medium.
χ	Contrast variable.

Acronym	Description
2D	Two-dimensional.
3D	Three-dimensional.
3G-CPW	Three-ground coplanar waveguide.
APP	Asymmetric parallel plate.
BA	Born approximation.
BIM	Born iterative method.
$\mathcal{C}_{\mathcal{F}}$	Calibration factor.
CG	Conjugate gradient.
Co-pol	Co polarized radiation.
CPW	Coplanar waveguide.
CSI	Contrast source inversion.
DBIM	Distorted Born iterative method.
DLVA	Double layered Vivaldi antenna.
EFVA	Eagle feed Vivaldi antenna.
FEM	Finite element method.
GNI	Gauss-Newton inversion method.
GPIB	General purpose interface bus.
HPBW	Half power beam width.
IM	Iterative methods.
MI	Microwave imaging.
MR	Multiplicatively regularized.
MST	Modulated scatterer technique.
MWT	Microwave tomography.
OI	Object of interest.
PDE	Partial differential equation.
PEC	Perfect electric conductor.
PIN	p-i-n diode: *p*-type *intrinsic* *n*-type semiconductor.
RF	Radio frequency.
Rx	Receiver.

SLYVA	Single layered Y-Y fed Vivaldi antenna.
SNR	Signal to noise ratio.
TE	Transverse electric.
TL	Transmission line.
TM	Transverse magnetic.
TSA	Tapered slot antenna.
Tx	Transmitter.
UM	University of Manitoba.
VNA	Vector network analyzer.
X-pol	Cross polarized radiation.

Chapter 1

Introduction

In many experimental investigations a frequent task is to assume a functional relation between *inputs* and outputs (*response*) of the system and then to evaluate unknown parameters of the relationship. It is assumed that the known functional relation can be described in the form of an equation:

$$\mathbf{Y} = f(\mathbf{r}, \chi) \tag{1.1}$$

where a set of n inputs $\mathbf{r}$, and k unknown parameters χ, correspond to m observed responses $\mathbf{Y}$. Usually an optimization algorithm is employed to minimize the residual error, $[\mathbf{Y} - f(\mathbf{r}, \chi)]$, over the unknown χ. In an inverse scattering problem, χ is a set of characteristics of the object, such as its location, material profile, shape, *etc.* and $\mathbf{Y}$ is obtained by measurement. Depending on the imaging modality, validity of the governing functional relation, or model, f, is a basic assumption. Within the wide framework of imaging problems, this thesis presents research work conducted in the area of developing different imaging systems and techniques for Microwave Imaging (MI) and Microwave Tomography (MWT).

With regard to equation (1.1), in MWT the Object of Interest (OI) is placed in a pre-defined imaging domain which is discretized into n pixels of known coordinates $\mathbf{r}$, and is illuminated by microwave energy. The resulting scattered fields are collected at m probing sites outside the OI, corresponding to $\mathbf{Y}$, and an imaging algorithm is uti-

lized to reconstruct the interior spatial distribution of dielectric properties of the OI, χ, referred to as an *image* of the OI. Frequencies utilized for electromagnetic imaging can vary from a couple of Hertz [2] up to Tera Hertz [3]. In the microwave range, MWT can be utilized for numerous applications, such as *non-destructive testing* for industrial and manufacturing applications [4], *geophysical surveying* or *remote sensing* in oil and earth sciences applications [2, 5], and *non-invasive biomedical imaging* in clinical applications [6, 7].

1.1 Motivation

Throughout this thesis, the process of quantifying the interior of an OI in a non-invasive manner is called *imaging*, where the interior spatial characteristics of the OI, such as dielectric properties are determined.

Of particular interest, the ability to reconstruct a quantitative and/or qualitative *image* of biological tissues has been investigated for decades. Different imaging modalities have been utilized to screen body tissues, including X-ray and Computed Tomography (CT), Ultrasound, and Magnetic Resonance Imaging (MRI) [8]. These modalities have drawbacks. For example, not only is X-ray mammography ionizing radiation, but it also suffers from a high false-positive rate in breast cancer detection. The high false-positive rate leads to an increased use of radiotherapy that can damage vessels and increase heart failure [9]. On the other hand, although MRI and ultrasound are non-ionizing radiation methods, they are not suitable for large scale screening of breast cancer. Considering these disadvantages, the need for improved and complementary cost effective imaging systems has led to further research into new imaging systems. As a result, MI/MWT, a relatively new imaging modality compared to X-ray, CT and MRI was introduced. The relatively low cost implemen-

tation of MWT, its use of non-ionizing radiation, portability and the capability to create quantitative images are the advantages of MI and MWT. The application of MWT for various biomedical imaging and screening applications is promising. This includes screening of breast [6, 10, 11], brain, and bone [7].

1.2 Imaging Algorithms

There are two fundamental approaches for MI: radar type methods and inverse scattering based methods. In radar methods, reflections of strong scatterers are searched within the imaging domain. The use of these algorithms for potential biological application was started in the late '90s [12]. The algorithms can be applied to either mono-static [13] and multi-static [14] measurements where a single transceiver or separate transmitter-receivers, collect the data. These methods can sometimes retrieve the shape and location of various inhomogeneities within the OI with computationally efficient algorithms [15], however, they do not generate quantitative images. Radar methods are not further discussed herein, but a recent review is available in [16].

Fully non-linear inverse scattering algorithms try to reconstruct the image of the OI through relatively intensive optimization methods, where typically a cross-sectional slice of the OI is reconstructed. Due to the 2D reconstruction, these methods are also known as tomography algorithms (MWT)*. Unlike X-ray tomography, where the wavelength of radiation is much smaller than the object and a ray propagation assumption can be made, in MWT, the relationship between the field propagation and the dielectric distribution of the OI is non-linear ($\mathbf{Y}$ and χ in equation (1.1)). The non-linearity is due to the multiple path scattering of fields inside the OI. In

* "tomo" is a Greek word which means slice. Please note that 3D methods are also being developed under the terminology of MWT [17].

addition to being non-linear, the inversion problem is ill-posed.

One of the earliest inversion methods used is the Born Approximation (BA) [18]. BA assumes that the OI is a weak scatterer and does not much disturb the incident field, so that the field inside the imaging domain is assumed to be the incident field which is known. The BA was improved in late '80s by introducing an iterative version for updating the fields [19]. This method is known as the Born Iterative Method (BIM). In the beginning of the '90s, an improvement of BIM, the Distorted BIM (DBIM) was introduced in which the Green's function was updated during the iterative optimization for more accurate calculation of scattered fields [20, 21].

In this thesis, two approaches are used for inversion. In the first approach, a forward solver is required to calculate the field due to a given dielectric distribution. It is coupled to an optimization procedure that updates the dielectric properties. This approach is based on the Gauss-Newton optimization scheme and is called Gauss-Newton Inversion method (GNI) [22]. In the second approach, no forward solver is required. The inversion problem is formulated using contrast sources as well as the contrast. This approach is called Contrast Source Inversion (CSI) [23]. Multiplicative Regularization (MR) is utilized with both methods to deal with the ill-posedness of the problem [22].

1.3 Imaging Systems

A typical configuration of MWT systems requires a transmitter antenna (Tx) to illuminate the OI and a receiver antenna (Rx) to collect the scattered fields. In order to ensure a robust and quantitatively accurate inversion a substantial amount of electromagnetic field measurements are required. Rotating the antennas introduces stresses on the cables resulting in phase error in the measurements. Moreover, rotating

the antennas requires a long acquisition time. The solution is to use a number of co-resident Tx and Rx antennas located along a line or a circle around the OI. There have been two common approaches for data acquisition in MWT systems, both of which measure the received voltage at the port of one or more of the receiving antennas:

- In the first approach, the measured voltage is used to infer the electromagnetic field impinging *directly* on the receiving antenna. This requires that an antenna factor, implicitly or explicitly, be part of the calibration procedure. It also requires that the receiving antenna be located at the points where the electromagnetic field needs to be measured. This has been accomplished by either repositioning the receiving antenna, or using an array of co-resident receiving antennas.

- The second approach uses the measured voltage at the receiving antenna to infer the electromagnetic field impinging on a *probe* positioned at some distance from the receiving antenna. This approach requires a Tx antenna and a *collector* antenna to interact with the probes.

One of the earliest biomedical MWT systems was developed in the late '70s [24] where the transmission coefficient of two parallel antennas was used *directly* to reconstruct images of a canine kidney [25]. In the beginning of the '80s, the first tomography system based on the Modulated Scatterer Technique (MST) and *indirect* measurement was developed [26], where an array of probes in conjunction with a collector antenna captured the scattering fields. The development of this system led to an imaging system which was demonstrated for imaging of the human hand and has also been used for non-destructive testing of concrete structures [27]. At the same time, a *direct* tomography system, consisting of 64 antennas, was reported where the human forearm was imaged [28]. The possibility of body temperature monitoring and

hyperthermia treatment was also studied in '80s and '90s [29, 30], and resulted in an 8-antenna *direct* tomography system [31]. Also, imaging of *in-vivo* tissues such as the canine heart was reported in [32]. These imaging systems were improved during the '90s until the first clinical prototype *direct* system for breast screening was introduced in 2000 [6]. In addition, some precise *direct* measurement systems were developed for both 2D [33] and 3D [34] scattering measurements.

The University of Manitoba (UM) imaging group has been active in MWT research. This group conducted research on *direct* as well as a combination of *direct* and *indirect* systems. Throughout this thesis, the development of an "air-based" MWT system as a part of UM imaging systems is reported. Several antennas were proposed and designed, fabricated and accurately tested. Finally, a system based on 24 Double Layered Vivaldi Antennas (DLVAs) was developed. The frequency behavior of this system was carefully studied in conjunction with different inversion algorithms. This air-based prototype system has been enhanced with a novel near-field technique based on the *indirect* scatterer probe technique, in which a secondary array of probes were added to the system to capture the scattered fields. In the preliminary *indirect* system, the number of probes and collectors were equal and the probe-collector distance was constant. Moreover, a system with a greater number of probes than collectors and different probe-collector separations was designed. The performance of these systems are compared in this thesis.

1.4 Thesis Organization

- In Chapter 2 the mathematical formulation and background theory related to MWT is briefly discussed. Herein, GNI and CSI methods are utilized for inversion, both are regularized using the MR method. Currently, the University of

Manitoba air-based MWT system utilizes Transverse Magnetic (TM) polarization and accordingly the algorithms in this thesis are also TM-based. A study of the 2D approximation of 3D objects is provided in [35] for cylindrical objects. A full description of the algorithms is available in [22, 23].

- In Chapter 3 the design of the *direct* air-based MWT system including three different antenna designs is explained. The antennas' performance is studied theoretically and experimentally. A frequency selection criteria and inversion results of different dielectric phantoms are presented. This chapter is concluded by indicating the disadvantages of *direct* MWT systems which are the limited number of measurement sites and the ambiguity of the measured polarization and locations.

- In Chapter 4 analysis of two different incident field models, the line source approximation and an accurate full 3D simulation of the air-based MWT system, with two different calibration techniques, the incident and the scattered is provided. The mean and the standard deviation of resultant images of all four combinations of the incident field models and the calibration techniques are compared. This study provides information for verifying the incident field modeling in the air-based system.

- A possible solution to increase the data is by utilizing near field probes and implementing an *indirect* system. This technique is based on MST. In Chapter 5, a review of near-field measurement techniques and MST is provided.

- In Chapter 6, a novel MWT system based on the scatterer probe technique is introduced which is a combination of the *direct* and *indirect* methods. This chapter outlines the design of the probes and the system. This chapter also

presents imaging results of different phantoms. The performance of this system with a non-uniform distribution of probes is then investigated. Different dielectric phantoms for this study are used.

- In Chapter 7, conclusions and suggestions for future work are outlined.

Chapter 2

Problem Statement and Mathematical Formulation

Maxwell's equations govern the propagation of electric ($\mathbf{E}$) and magnetic ($\mathbf{H}$) fields. The time-harmonic form of Maxwell's equations depend implicitly on $e^{j\omega t}$, where ω is the radial frequency (rad/s). Without the presence of a magnetic source, these equations can be written as [36, 37]:

$$\nabla \times \mathbf{E}(\mathbf{r}) = -j\omega\mu(\mathbf{r})\mathbf{H}(\mathbf{r}) \tag{2.1}$$

$$\nabla \times \mathbf{H}(\mathbf{r}) = j\omega\epsilon(\mathbf{r})\mathbf{E}(\mathbf{r}) + \mathbf{J}_i(\mathbf{r}) \tag{2.2}$$

$$\nabla \cdot \epsilon(\mathbf{r})\mathbf{E}(\mathbf{r}) = \rho(\mathbf{r}) \tag{2.3}$$

$$\nabla \cdot \mu(\mathbf{r})\mathbf{H}(\mathbf{r}) = 0 \tag{2.4}$$

where $\mathbf{E}$, $\mathbf{H}$, ϵ, μ, $\mathbf{J}_i$, and ρ, are the electric field intensity (V/m), magnetic field intensity (A/m), permittivity (F/m), permeability (H/m), volume current density of impressed current ($\mathrm{A \cdot s/m^2}$), and charge density ($\mathrm{A \cdot s/m^3}$), respectively. $\mathbf{r}$ is the position vector. In the Cartesian coordinate system $\mathbf{r} = x\hat{\mathbf{x}} + y\hat{\mathbf{y}} + z\hat{\mathbf{z}}$ and $\nabla = \frac{\partial}{\partial x}\hat{\mathbf{x}} + \frac{\partial}{\partial y}\hat{\mathbf{y}} + \frac{\partial}{\partial z}\hat{\mathbf{z}}$.

The medium conductivity, $\sigma(\mathbf{r})$ (S/m), is implicitly incorporated into the complex

permittivity:

$$\epsilon(\mathbf{r}) = \epsilon_0(\epsilon_r(\mathbf{r}) - j\frac{\sigma(\mathbf{r})}{\omega\epsilon_0}) = \epsilon'(\mathbf{r}) - j\epsilon''(\mathbf{r}) \tag{2.5}$$

In theory, all electromagnetic phenomenon can be formulated via Maxwell's equations. In fact, there is no theoretical limitation in applying 3D formulations to MI problems. However, solving these equations for a problem that includes both radiation from antennas and scattering by different objects, in 3D, is extremely computationally intensive. Therefore, usually some assumptions are applied to simplify the MI formulation. In this thesis, the following assumptions are made:

- The medium is non magnetic so that the permeability is the same as that of air: $\mu(\mathbf{r}) = \mu_0$ or simply μ.
- The inversion problem can be formulated in 2D, thus, the assumption is that the dielectric properties along $\hat{\mathbf{z}}$ are uniform and that $\epsilon(\mathbf{r}) = \epsilon(x, y)$.
- The fields are TM_z polarized which means: $E_x\hat{\mathbf{x}} = 0$ and $E_y\hat{\mathbf{y}} = 0$.

2.1 MWT Governing Equations

A typical schematic of an MWT system is shown in Figure 2.1. The unknown OI is placed inside an imaging domain, $\mathcal{D}$. The OI is illuminated successively by Tx antennas, from different angles. For each angle of illumination, the Rx antennas collect the scattered field in a *measurement* or *data* region $\mathcal{S}$, outside the OI. Γ represents the boundary: in free-space, the fields vanish ($\mathbf{E}$ and $\mathbf{H} \to 0$) at infinity ($\mathbf{r} \to \infty$). The fields in the absence and presence of the OI, are called the *incident* $\mathbf{E}^{inc}$, and the *total* field $\mathbf{E}^{tot}$, respectively. The difference between the incident and

total field is called the *scattered* field $\mathbf{E}^{sct}$:

$$\mathbf{E}^{sct}(\mathbf{r}) = \mathbf{E}^{tot}(\mathbf{r}) - \mathbf{E}^{inc}(\mathbf{r}) \tag{2.6}$$

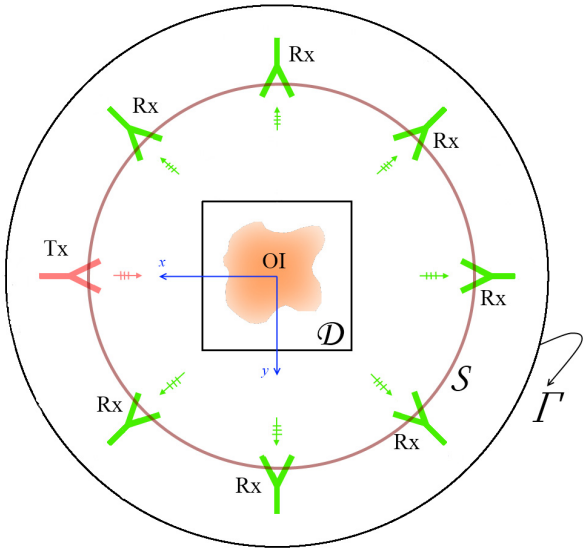

Figure 2.1: Schematic of a typical MWT system, consisting of Tx and Rx antennas which circumscribe $\mathcal{D}$. $\mathcal{D}$ is the imaging domain including the OI. $\mathcal{S}$ is the measurement region. Γ represents the boundary of the problem. In free-space, fields vanish when $\mathbf{r} \to \infty$.

2.1.1 Wave Equation

From (2.1) and (2.2) a vector equation for $\mathbf{E}$ can be derived: $\nabla \times (\nabla \times \mathbf{E}) = \omega^2\mu\epsilon(\mathbf{r})\mathbf{E} - j\omega\mu\mathbf{J}_i(\mathbf{r})$. Considering vector identity $\nabla \times (\nabla \times \mathbf{E}) = \nabla(\nabla \cdot \mathbf{E}) - \nabla^2\mathbf{E}$:

$$\nabla^2\mathbf{E} - \nabla(\nabla \cdot \mathbf{E}) + \omega^2\mu\epsilon(\mathbf{r})\mathbf{E} = j\omega\mu\mathbf{J}_i(\mathbf{r}) \tag{2.7}$$

Since the imaging domain does not contain any source of external current or charge density, $\mathbf{J}_i(\mathbf{r}) = \rho(\mathbf{r}) = 0$. From (2.3) one can write the following relation:

$$\nabla \cdot (\epsilon(\mathbf{r})\mathbf{E}(\mathbf{r})) = \nabla\epsilon(\mathbf{r}) \cdot \mathbf{E}(\mathbf{r}) + \epsilon(\mathbf{r})\nabla \cdot \mathbf{E}(\mathbf{r}) = 0 \tag{2.8}$$

With regard to the assumptions in MWT, $\epsilon(\mathbf{r}) = \epsilon(x, y)$ and $E_x = E_y = 0$, therefore, the first term of equation (2.8), $\nabla\epsilon(\mathbf{r}) \cdot \mathbf{E}(\mathbf{r})$, vanishes and the following relation holds:

$$\nabla \cdot \mathbf{E}(\mathbf{r}) = 0 \tag{2.9}$$

Considering (2.7) and (2.9), the scaler TM_z wave equation is deduced which is in the form of the Helmholtz equation:

$$\nabla^2\mathbf{E}(\mathbf{r}) + k^2(\mathbf{r})\mathbf{E}(\mathbf{r}) = 0 \tag{2.10}$$

where, $\mathbf{E} = E_z\hat{\mathbf{z}}$, and $k^2 = \omega^2\mu\epsilon(\mathbf{r})$, is called the complex wave number. $\epsilon(\mathbf{r})$ is the complex permittivity (2.5).

2.1.2 Contrast Sources

From (2.6) and (2.10), Partial Differential Equations (PDE) of the incident and total fields can be rewritten as

$$\left.\begin{array}{l} \nabla^2\mathbf{E}^{inc}(\mathbf{r}) + k_b^2 \quad \mathbf{E}^{inc}(\mathbf{r}) = 0 \\ \nabla^2\mathbf{E}^{tot}(\mathbf{r}) + k^2(\mathbf{r})\mathbf{E}^{tot}(\mathbf{r}) = S(t) \end{array}\right\} \Rightarrow \nabla^2\mathbf{E}^{sct}(\mathbf{r}) + k^2(\mathbf{r})\mathbf{E}^{tot}(\mathbf{r}) - k_b^2\mathbf{E}^{inc}(\mathbf{r}) = 0$$

where $k_b^2 = \omega^2\mu\epsilon_b$ is the background medium complex wavenumber (permittivity when the OI is absent) and $S(t)$ represent the sources. Defining a normalized contrast

function, χ:

$$\chi(\mathbf{r}) = \frac{k^2(\mathbf{r}) - k_b^2}{k_b^2} = \frac{\epsilon_r(\mathbf{r}) - \epsilon_b}{\epsilon_b} \tag{2.11}$$

and $k^2(\mathbf{r}) = k_b^2(1 + \chi(\mathbf{r}))$, the following PDE holds for the scattered field:

$$\nabla^2 \mathbf{E}^{sct}(\mathbf{r}) + k_b^2 \mathbf{E}^{sct}(\mathbf{r}) = -k_b^2 \, \chi(\mathbf{r}) \mathbf{E}^{tot}(\mathbf{r}) = -k_b^2 \, \mathcal{W}(\mathbf{r}) \tag{2.12}$$

Here $\mathcal{W}(\mathbf{r}) = \chi(\mathbf{r})\mathbf{E}^{tot}(\mathbf{r})$ is defined as the contrast sources (compare with (2.7)). In this thesis (2.12) is the fundamental equation for MWT implementation.

2.1.3 Data and Domain Equations

Equation (2.12) can be solved in integral form using Green's function. Here, the Green's function satisfies the boundary condition at infinity (in free-space, when $\mathbf{r} \to \infty$, then $\mathbf{E}(\mathbf{r}) \to 0$) and the following equation:

$$\nabla^2 G(\mathbf{r}, \mathbf{r}') + k_b^2 G(\mathbf{r}, \mathbf{r}') = -\delta(\mathbf{r} - \mathbf{r}') \tag{2.13}$$

The solution of (2.13) is [36]:

$$G_0(\mathbf{r}, \mathbf{r}') = \frac{j}{4} H_0^{(2)}(k_b \, |\mathbf{r} - \mathbf{r}'|) \tag{2.14}$$

where $H_0^{(2)}$ is the Hankel function of second kind and zero order, and $j^2 = -1$. Using the Green's identity, the solution of (2.12) at arbitrary position $\mathbf{r}$, can be written as

$$\mathbf{E}^{sct}(\mathbf{r}) = k_b^2 \int_{\mathcal{D}} G(\mathbf{r}, \mathbf{r}') \chi(\mathbf{r}') \mathbf{E}^{tot}(\mathbf{r}') d\mathbf{r}' \tag{2.15}$$

where $\mathbf{r}'$ represents the contrast source locations in $\mathcal{D}$. Equation (2.6) and (2.15) provide a solution of fields at any given $\mathbf{r}$, including the measurement domain $\mathcal{S}$, and the imaging domain $\mathcal{D}$. One can write equations for each of the two domains using (2.15), referred to as the *data equation* and the *domain equation*, respectively.

$$\text{Data equation:} \quad \mathbf{E}^{sct}(\mathbf{r}) = k_b^2 \int_{\mathcal{D}} G(\mathbf{r}, \mathbf{r}')\chi(\mathbf{r}')\mathbf{E}^{tot}(\mathbf{r}')d\mathbf{r}', \text{ and } \quad \mathbf{r} \in \mathcal{S} \tag{2.16}$$

$$\text{Domain equation:} \quad \mathbf{E}^{tot}(\mathbf{r}) = \mathbf{E}^{inc}(\mathbf{r}) + k_b^2 \int_{\mathcal{D}} G(\mathbf{r}, \mathbf{r}')\chi(\mathbf{r}')\mathbf{E}^{tot}(\mathbf{r}')d\mathbf{r}', \text{ and } \quad \mathbf{r} \in \mathcal{D} \tag{2.17}$$

Note that in the data equation, the measured data should be substituted in the left side of this equation.

In the equations of (2.16) and (2.17), the contrast χ and the total field $\mathbf{E}^{tot}$ are both unknown and under the integral. These equations are Fredholm integral equations [38] but in general these are non-linear integral equations.

Equations (2.16) and (2.17) form the system of equations for inverse problem formulation. Solution to this set of equations is what the imaging algorithm searches for, which is χ.

From Hadamard definition, a problem is *well-posed* if its solution exists, depends continuously on the given data and is unique. Existence means that there exist at least one solution. Continuity means that a small change in data, does not produce a significant change in the solution and uniqueness means that the solution is the only solution. The set of coupled inverse problem equations, together, are non-linear and *ill-posed* [39].

For simplicity, (2.16) and (2.17) can be represented by a linear operator $\mathcal{G}_i$, where

$i = \mathcal{D}$ or $\mathcal{S}$ for the data and domain equations, respectively:

$$\mathcal{G}_i(\mathbf{X}) = k_b^2 \int_{\mathcal{D}} G(\mathbf{r}, \mathbf{r}')\mathbf{X}(\mathbf{r}')d\mathbf{r}' \tag{2.18}$$

Note that for $i = \mathcal{D}$ or $\mathcal{S}$, the integration is taken over $\mathcal{D}$, however for $\mathcal{G}_\mathcal{D}$, $\mathbf{r} \in \mathcal{D}$ and for $\mathcal{G}_\mathcal{S}$, $\mathbf{r} \in \mathcal{S}$. This integral can be calculated using spatial Fourier transform [22].

Another operator $\mathcal{G}_\mathcal{D}^\varphi$ is also defined as

$$\mathcal{G}_\mathcal{D}^\varphi(\mathbf{X}) = k_b^2 \int_{\mathcal{D}} G(\mathbf{r}, \mathbf{r}')\mathbf{X}(\mathbf{r}')\varphi(\mathbf{r}')d\mathbf{r}' \tag{2.19}$$

where the scalar function φ is defined in $\mathcal{D}$.

The data and domain equations, (2.16) and (2.17), can now be rewritten using operators (2.18) and (2.19):

$$\text{Data equation:} \quad \mathbf{E}^{sct}(\mathbf{r}) = \mathcal{G}_\mathcal{S}(\chi\mathbf{E}^{tot}) = \mathcal{G}_\mathcal{S}^\chi(\mathbf{E}^{tot}) \quad , \mathbf{r} \in \mathcal{S} \tag{2.20}$$

$$\text{Domain equation:} \quad \mathbf{E}^{tot}(\mathbf{r}) = \mathbf{E}^{inc}(\mathbf{r}) + \mathcal{G}_\mathcal{D}(\chi\mathbf{E}^{tot}) \quad , \mathbf{r} \in \mathcal{D} \tag{2.21}$$

From the measurement, $\mathbf{E}_{meas}^{sct}$ is known in $\mathcal{S}$. $\mathbf{E}^{inc}$ is also known everywhere. The total fields inside $\mathcal{D}$ are evaluated from (2.21):

$$\mathbf{E}^{tot} - \mathcal{G}_\mathcal{D}^\chi(\mathbf{E}^{tot}) = \mathbf{E}^{inc} \tag{2.22}$$

(2.22) represents the relation between $\mathbf{E}^{tot}$ and $\mathbf{E}^{inc}$. $\mathbf{E}^{tot}$ is evaluated from a minimization of $\|(\mathbf{E}^{tot} - \mathcal{G}_\mathcal{D}^\chi(\mathbf{E}^{tot})) - \mathbf{E}^{inc}\|_\mathcal{D}^2 / \|\mathbf{E}^{inc}\|_\mathcal{D}^2$, where $\|\mathbf{X}\| = \sqrt{\int \mathbf{X} \cdot \mathbf{X}^* d\mathbf{r}'}$ is the Euclidean norm and "*" is the complex conjugate operator. Herein, any solver of (2.21) or (2.22) assuming χ to be known is referred to as a *forward solver*. The min-

imization can be done using different optimization techniques such as the Conjugate Gradient (CG) method [22]. For simplicity one can represent (2.22) by operator terminology where $\mathbf{E}^{tot} - \mathcal{G}_{\mathcal{D}}^{\chi}(\mathbf{E}^{tot})$ is represented by $[\mathcal{I} - \mathcal{G}_{\mathcal{D}}^{\chi}](\mathbf{E}^{tot})$, where $\mathcal{I}$ represents the identity operator and $\mathcal{I}(\mathbf{X}) = \mathbf{X}$. Using this representation (2.22) is shown as

$$[\mathcal{I} - \mathcal{G}_{\mathcal{D}}^{\chi}](\mathbf{E}^{tot}) = \mathbf{E}^{inc} \Rightarrow \mathbf{E}^{tot} = [\mathcal{I} - \mathcal{G}_{\mathcal{D}}^{\chi}]^{-1}(\mathbf{E}^{inc}) \tag{2.23}$$

Note that the operators are not subtracted or inversed. This representation is used to show a more clear relationship between the fields. The scattered field $\mathbf{E}^{sct}$ can be calculated from (2.20) and (2.23):

$$\mathbf{E}^{sct}(\mathbf{r}) = \mathcal{G}_{\mathcal{S}}\left(\chi[\mathcal{I} - \mathcal{G}_{\mathcal{D}}^{\chi}]^{-1}(\mathbf{E}^{inc})\right) \tag{2.24}$$

2.2 Linear Inversion Methods

Equation (2.20) can be linearly approximated to find the unknown contrast function χ. In the BA [40], the OI is assumed to be a weak scatterer so that the total field $\mathbf{E}^{tot}$ in (2.20) is approximated by $\mathbf{E}^{inc}$ and the Green's operator is approximated by the one corresponding to the background medium, for example free-space. Clearly, there is no need to solve (2.23) because $[\mathcal{I}-\mathcal{G}_{\mathcal{D}}^{\chi}]^{-1}$ is approximated by $\mathcal{I}$. The contrast χ, is the only unknown of (2.20) and it can be evaluated by minimizing a normalized least square cost function $\mathcal{F}^{LS}$:

$$\mathcal{F}^{LS}(\chi) = \frac{\|\mathbf{E}^{sct} - \mathbf{E}^{sct}_{meas}\|^2_{\mathcal{S}}}{\|\mathbf{E}^{sct}_{meas}\|^2_{\mathcal{S}}} \approx \frac{\|\mathcal{G}^{\chi}_{\mathcal{S}0}\left(\mathbf{E}^{inc}\right) - \mathbf{E}^{sct}_{meas}\|^2_{\mathcal{S}}}{\|\mathbf{E}^{sct}_{meas}\|^2_{\mathcal{S}}} \tag{2.25}$$

where $\mathcal{G}^{\chi}_{\mathcal{S}0}$ is the background Green's function operator (2.19). The minimization can also be manipulated to where one has to invert a 2D Fourier transform. A review of these methods is available in [23]

2.3 Non-linear Iterative Methods

In Iterative Methods (IM), the unknown contrast χ is iteratively updated using an optimization technique. Two approaches are usually employed:

- **Conventional approach:** In conventional approach, the minimization is applied to a cost function similar to (2.25). Different algorithms have been utilized in this category. The BIM [19] updates the contrast at each iteration i, using (2.20). Then, $\mathbf{E}^{tot}_i$ is updated from (2.23). The iterative steps continue until the predicted scattered field gets close enough to the measured scattered field $\mathbf{E}^{sct}_{meas}$ on $\mathcal{S}$. The cost function to be minimized, $\mathcal{F}^{IM}$, is derived from (2.24) as

$$\mathcal{F}^{IM}(\chi) = \frac{\|\mathbf{E}^{sct} - \mathbf{E}^{sct}_{meas}\|^2_{\mathcal{S}}}{\|\mathbf{E}^{sct}_{meas}\|^2_{\mathcal{S}}} = \frac{\|\mathcal{G}_{\mathcal{S}}\left(\chi[\mathcal{I} - \mathcal{G}^{\chi}_{\mathcal{D}}]^{-1}(\mathbf{E}^{inc})\right) - \mathbf{E}^{sct}_{meas}\|^2_{\mathcal{S}}}{\|\mathbf{E}^{sct}_{meas}\|^2_{\mathcal{S}}} \tag{2.26}$$

  In the DBIM [20, 21], the Green's function is also updated at each iteration. Newton type algorithms [41] such as GNI, approximate the cost function (2.26) in a quadratic form at each iteration i. Then the contrast is updated as

$$\chi_{i+1} = \chi_i + \alpha_i \Delta\chi_i \tag{2.27}$$

  where $\Delta\chi_i$ is the updating correction, weighted by a number, α_i [42]. Global optimization methods can also be utilized to minimize (2.26) such as genetic algorithm [43] and simulated annealing [39].

- **Contrast source approach:** In this approach, the forward solver is absent. By multiplying both sides of (2.21) by the contrast function, χ, and denoting contrast sources by $\mathcal{W}(\mathbf{r})$ (2.12), the following equation holds:

$$\mathcal{W} = \chi\, \mathbf{E}^{inc} + \chi\, \mathcal{G}_{\mathcal{D}}(\mathcal{W}) \tag{2.28}$$

The data equation (2.20) can be written as:

$$\mathbf{E}^{sct} = \mathcal{G}_{\mathcal{S}}(\mathcal{W}) \tag{2.29}$$

The cost function to be minimized, from (2.28) and (2.29) is [44, 45]:

$$\mathcal{F}^{CSI} = \frac{\|\mathbf{E}^{sct}_{meas} - \mathcal{G}_{\mathcal{S}}(\mathcal{W})\|^2_{\mathcal{S}}}{\|\mathbf{E}^{sct}_{meas}\|^2_{\mathcal{S}}} + \frac{\|\chi\mathbf{E}^{inc} - \mathcal{W} + \chi\mathcal{G}_{\mathcal{D}}(\mathcal{W})\|^2_{\mathcal{D}}}{\|\chi\mathbf{E}^{inc}\|^2_{\mathcal{D}}} \tag{2.30}$$

In this method, both the contrast and the contrast sources corresponding to the total field in the imaging domain, are taken as the optimization variable and therefore, there is no need for a forward simulation. The CSI and Newton type algorithms provide similar inversion results [46].

In this thesis, the non-linear inversion methods, GNI and CSI, are utilized for image reconstruction. These algorithms require some sort of regularization to convert them to *well-posed* problems. This can be done by different kinds of regularization techniques, such as additive methods, in which an identity matrix multiplied by a coefficient is added to the cost function [20], or multiplicative methods [45]. Herein, the MR technique is utilized for both GNI and CSI algorithms. The algorithms and regularization techniques are not the focus of this thesis, complete details are available in [22, 23].

Chapter 3

Direct Microwave Tomography System

As mentioned in Chapter 1, in order to collect data for MWT, one advantageous approach is the use of co-resident antennas located outside the OI. This region, which is referred to as the measurement domain, encircles the OI. With this approach each antenna is successively activated as a transmitter to illuminate the OI from different angles. For each active transmitter, the field scattered by the OI is measured with the remaining antennas which act as receivers. The voltage measured by the receivers is used to infer the electromagnetic field impinging directly on the antenna. Herein, this type of field collection approach is referred to as a "direct" measurement approach.

In the framework of the direct approach, an MWT system was developed that includes twenty-four co-resident antennas, mounted on a Plexiglas chamber. In this chapter this system is described. Herein, the antennas designed for the system, the performance of the co-resident antennas inside the chamber, a frequency selection method, and imaging results are presented.

3.1 Antennas

In previously reported direct MWT systems, various types of measurement systems have been utilized and different parameters change within these systems including the type of Tx and Rx antennas, the number of antennas, frequency of operation, stationary or moving measurement system, and far-field or near-field measurements.

For example, the systems reported in [31] and [47] use open-ended waveguide antennas and monopole antennas as the Tx and Rx, respectively, where the frequency range of measurement is 300-1000 MHz. In [6, 11], only monopole antennas are utilized for both Tx and Rx cases. The use of dielectric filled open-ended waveguide antennas are reported in several systems, where the operating frequency is 2330 MHz [48], 2450 MHz [32] and 900 MHz [49]. A far-field system utilizing double ridged horn antennas in a frequency range of 2 GHz to 18 GHz is reported in [33], and the use of parabolic reflector as Tx and double ridged horn as Rx in the frequency range of 3 GHz to 8 GHz is reported in [34].

In the UM imaging group, the approach was to develop a system for TM_z based imaging. Due to specific polarization requirement of the system, the cross polarization level (X-pol) of the antennas was a selection criterion for the antenna design. Also development of an array of co-resident antennas for fast data acquisition was desired. Due to the uncertainty in the best operating frequency, developing a wideband system was a suitable solution. Since the use of exponential tapering provides a very wideband frequency response, I focused on its use for Tapered Slot Antennas (TSA).

The TSA is one of several broadband antennas proposed in the '70s [50, 51]. It is in the category of surface traveling wave antennas or slow wave structures, which in general, radiate in the end-fire direction [52]. This antenna consists of a slot line guided region that might be tapered in different ways such as linear, exponential (Vivaldi), and constant [53]. There are many applications for TSAs such as millimeterwave [54], wireless communication [55], and ultra wideband communication [56]. In particular, Vivaldi antennas have also been utilized for MI applications, including the radar-based methods [57–59].

The design of three different TSAs is reported: Double Layered Vivaldi Antennas

(DLVA), Single Layered Y-Y fed Vivaldi Antenna (SLYVA) and a new TSA which is called the Eagle Feed Vivaldi Antenna (EFVA). Among the three candidates, the one with the lowest X-pol level, the DLVA, was chosen for UM air-based MWT system.

3.1.1 Double Layered Vivaldi Antenna (DLVA)

In this section, a DLVA is investigated which is suitable to be used in a multi-static tomography system with fast acquisition time. The antennas are designed such that mutual coupling in close proximity with other DLVAs is minimized. The reason for choosing the DLVA is that they are intrinsically broadband, and can provide a pure polarization. Their directive pattern, with an average gain of 7 dBi, can increase the sensitivity of the system, by concentrating the power in one direction. Another advantage to the directive pattern is presenting a wide beam in one plane and narrow beam in the orthogonal plane that is very useful for illuminating a 2D cross sectional slice of the object in a tomography system. A Single layer Vivaldi antenna as the element of a circular array was suggested for MI measurements in [60]. The level of X-pol of this antenna can be improved by adding another layer. This leads to better polarization purity [61]. The double layer design to be presented here, has improved the X-pol by at least 10 dB [62].

The fabrication sensitivity of the DLVA has also been studied and found that even a small misalignment in the fabrication deteriorates the X-pol, especially in the E-plane. Compared to the EFVA (Section 3.1.5) and SLYVA (Section 3.1.6), and considering the fabrication sensitivity and X-pol level improvement, the DLVA was selected for UM MWT system.

3.1.2 DLVA Configuration, Design Steps

The DLVA consists of two major parts, a feed-line and three radiation flares. The shape of the flares follow an elliptical configuration. Since the antenna is fabricated using two substrates, the feed-line excitation can be provided by a stripline transmission line, which is tapered gradually to the radiation flares. Because of the gradual tapering from the unbalanced stripline feed to the balanced radiation flares, there is no need to use a balun for this structure. All simulations of the design are done by the Finite Element Method (FEM) using Ansoft HFSS simulation software [63].

Design Steps

The antenna geometry is shown in Figure 3.1. The design procedure is as follows:

1. Substrate: Arlon-Diclad 527 substrate was chosen with relative permittivity of $\epsilon_r \approx 2.5$ and loss tangent of $\tan\delta = 0.0022$. Depending on the availability and the size of the stripline connector, choices of substrate thickness are limited. Here the thickness is $h = 0.0625$ inch.

2. Antenna main dimensions: Theoretically, the upper frequency limit of a Vivaldi antenna is infinity. The lower frequency limit depends mainly on W_s which should be half of the effective wavelength (λ_{eff}) at the lowest frequency. The effective wavelength is calculated as [64]

$$\lambda_{eff} \approx \frac{\lambda_0}{\sqrt{\epsilon_r}} = \frac{c}{f\sqrt{\epsilon_r}} \quad , \quad W_s \approx \frac{\lambda_{eff}}{2} \tag{3.1}$$

where λ_0 and c are the free-space wavelength and light speed, respectively.

The feed line width, W_f, is calculated from [64]

$$x = \frac{30\pi}{\sqrt{\epsilon_r} Z_0} - 0.441, \quad \frac{W_f}{h} = \begin{cases} x & \sqrt{\epsilon_r} Z_0 < 120 \\ 0.85 - \sqrt{0.6 - x} & \sqrt{\epsilon_r} Z_0 > 120 \end{cases} \tag{3.2}$$

As shown in Figure 3.1, the antenna length consists of the feed section L_f, and the radiation section $(L_s - L_f)$. The radiation section consists of three ellipses: one on the left side, and the other two on the right side, see Figure 3.1 (a) and (b). Smoother tapering of the radiation section provides a less variation in gain, but increases the size. Decreasing the feed portion deteriorates the gain flatness within the operating bandwidth. Using a parametric study, the antenna dimensions were computed so as to achieve a maximum bandwidth, a minimum size of the antenna, and a flat gain versus frequency. This parametric study was performed by sweeping the dimensions of the radiation flare curves in terms of the ratios of ellipses radii. Optimum values are obtained as

$$\begin{array}{lcllcl} L_s & = & W_s = 70 \text{ mm} & , & L_f & = & 18 \text{ mm} \\ Rs_v & = & W_s/2 & , & Rs_h/Rl_h & = & 0.48 \\ Rl_h & = & (W_s - W_f)/2 & , & Rl_v/Rs_v & = & 1.67 \end{array} \tag{3.3}$$

3. Sandwiching: The two layers should be sandwiched. Nylon screws were used for this purpose, since their dielectric properties are very close to that of the substrate. The fabricated antenna is shown in Figure 3.1 (c).

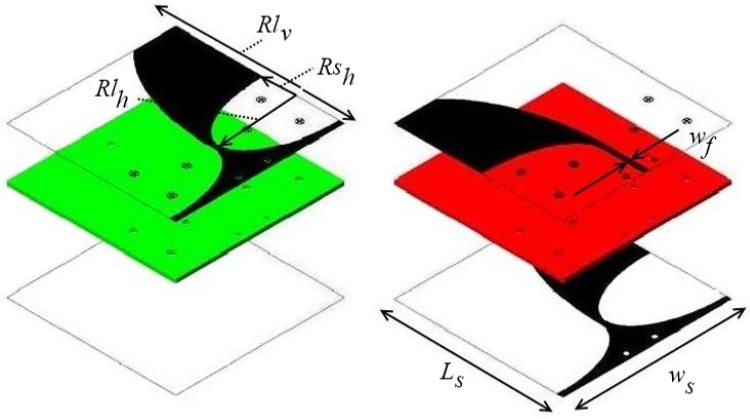

(a)

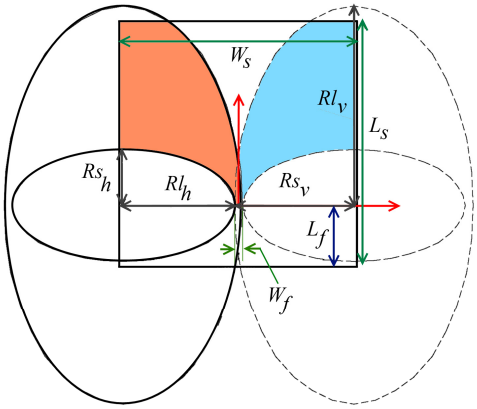

(b)

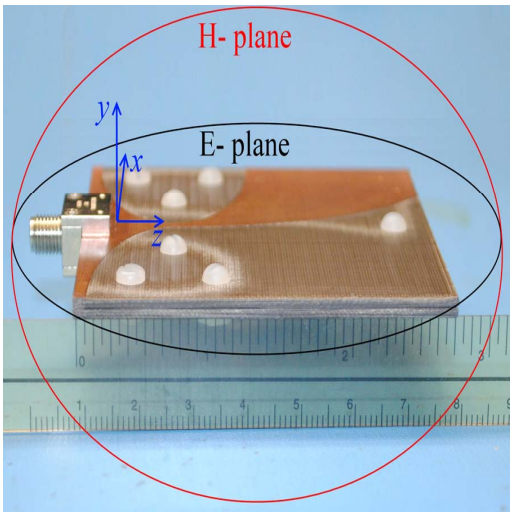

(c)

Figure 3.1: DLVA: (a) layers, (b) dimensions, and (c) fabricated antenna including E- and H-planes.

3.1.3 DLVA Impedance Bandwidth and Radiation Behavior

The reflection coefficient of the DLVA is shown in Figure 3.2. The impedance bandwidth covers the frequency range of 3.3 GHz to 10 GHz. There is a slight frequency difference between the measurement and simulation. In addition to computational error, it may be mainly due to fabrication error for mounting the connector.

Radiation pattern: The E- $(x-z)$ and H- $(y-z)$ planes of the DLVA are illustrated in Figure 3.1 (c). The DLVA pattern measurement setup is shown in Figure 3.3. The anechoic chamber was calibrated by a reference horn antenna. The minimum sensitivity of the compact range measurement in the UM chamber is -35 dB, therefore, the X-pol results under -35 dB are not valid. The angular resolution of measurement is 1°. The measured and simulated fields are compared in Figure 3.4 at 3.7 GHz, 6.7 GHz and 9.7 GHz. In these figures M, S, Co, and X stand for the measured, simulated, Co-pol level, and X-pol level, respectively. As expected, the pattern is wider in the H-plane. In the H-plane, the simulation results agree well with the measurements at all frequencies. In the E-plane, simulated Co-pol patterns agree well with the measurements; but simulated X-pol patterns do not follow the measurements. As shown in Figure 3.4 (b), (d), and (f), there is up to 15 dB difference between the results. To achieve further certainty of proper measurement results, another kind of measurement was performed where the DLVA was kept stationary in the chamber while the chamber transmitter antenna was rotated. To perform this measurement, the DLVA was mounted once in the E-plane and then in the H-plane, as shown in Figure 3.3. The result of these measurements for the center frequency of 6.7 GHz is shown in Figure 3.5. It can be seen that the maximum of the X-pol level is -36 dB (at $\theta = 0$) and it is symmetrically changing. This is consistent with the results of Figure 3.4 (c,d) from the standard measurement. Similar results were

observed at other frequencies. After validation of X-pol measurement by these two methods, fabrication sensitivity was studied to investigate the source of error in the E-plane pattern.

Also the co- and x-pol patten at four orthogonal planes of $\phi = 0°$, $\phi = 45°$, $\phi = 90°$, and $\phi = 135°$ are presented at frequencies of 3.7 GHz, 6.7 GHz, and 9.7 Ghz in Figure 3.6, Figure 3.7, and Figure 3.8. In the E-plane, $\phi = 0°$, the X-pol is minimum due to the cancellation of cross-polarized field between the two substrates of the antenna.

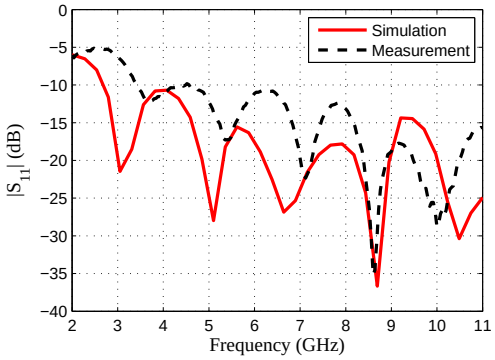

Figure 3.2: DLVA reflection coefficient, simulation and measurement.

3.1.4 DLVA Fabrication Sensitivity

To study the sensitivity of the antenna performance to fabrication tolerances, three cases are simulated that are described in Table 3.1. In these cases, misalignments in horizontal and vertical axes are considered as it could happen in fabrication process. The horizontal misalignment may happen due to a small movement of substrates being sandwiched. The vertical misalignment (rotation) may happen due to the presence of 6 nylon screws on one side of the substrates and only 1 nylon screw at the front location. Simulations show that the misalignment significantly deteriorates

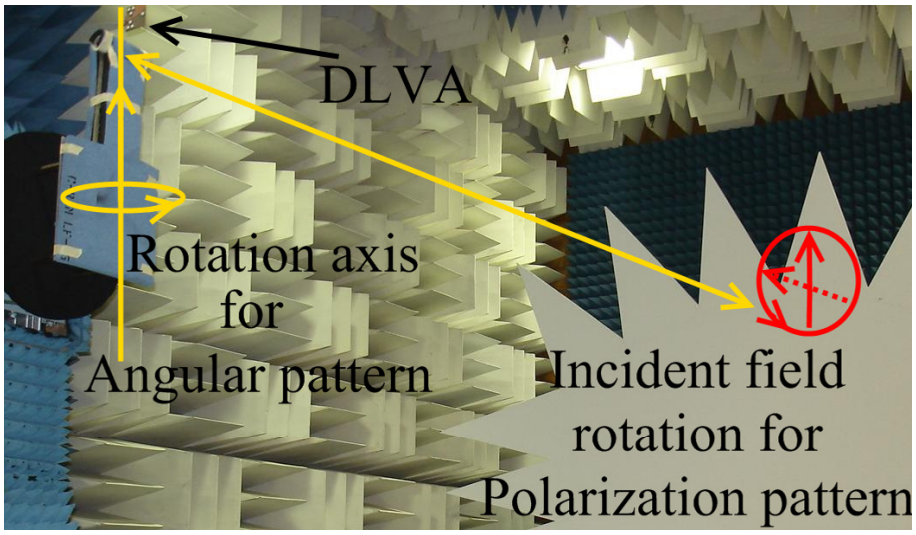

Figure 3.3: DLVA antenna pattern measurement in anechoic chamber.

Table 3.1: Fabrication tolerance due to misalignment

Case	Description
1	Ideal alignment of upper and lower layers.
2	Misalignment of one layer in horizontal direction ($x-z$ plane) by 0.5 mm.
3	Misalignment of one layer in vertical direction ($y-z$ plane) by 1°.

the E-plane X-pol level, but it hardly changes the X-pol level in the H-plane. These results are shown in Figure 3.9 at three frequencies within the bandwidth. As shown in these figures, the E-plane X-pol level increases by an average of 15 dB, because of the fabrication error. The H-plane results do not change, so they are not shown.

3.1.5 Eagle Feed Vivaldi Antenna (EFVA)

In this section, a novel combination method is presented which is utilized to design an antenna called EFVA. The antenna structure is discretized into an arbitrary number of sections whose characteristic impedances and their corresponding dimensions are evaluated using Transmission Line (TL) theory and the FEM, respectively.

As mentioned in Section 3.1.1, the Vivaldi antenna is a planar antenna and can be

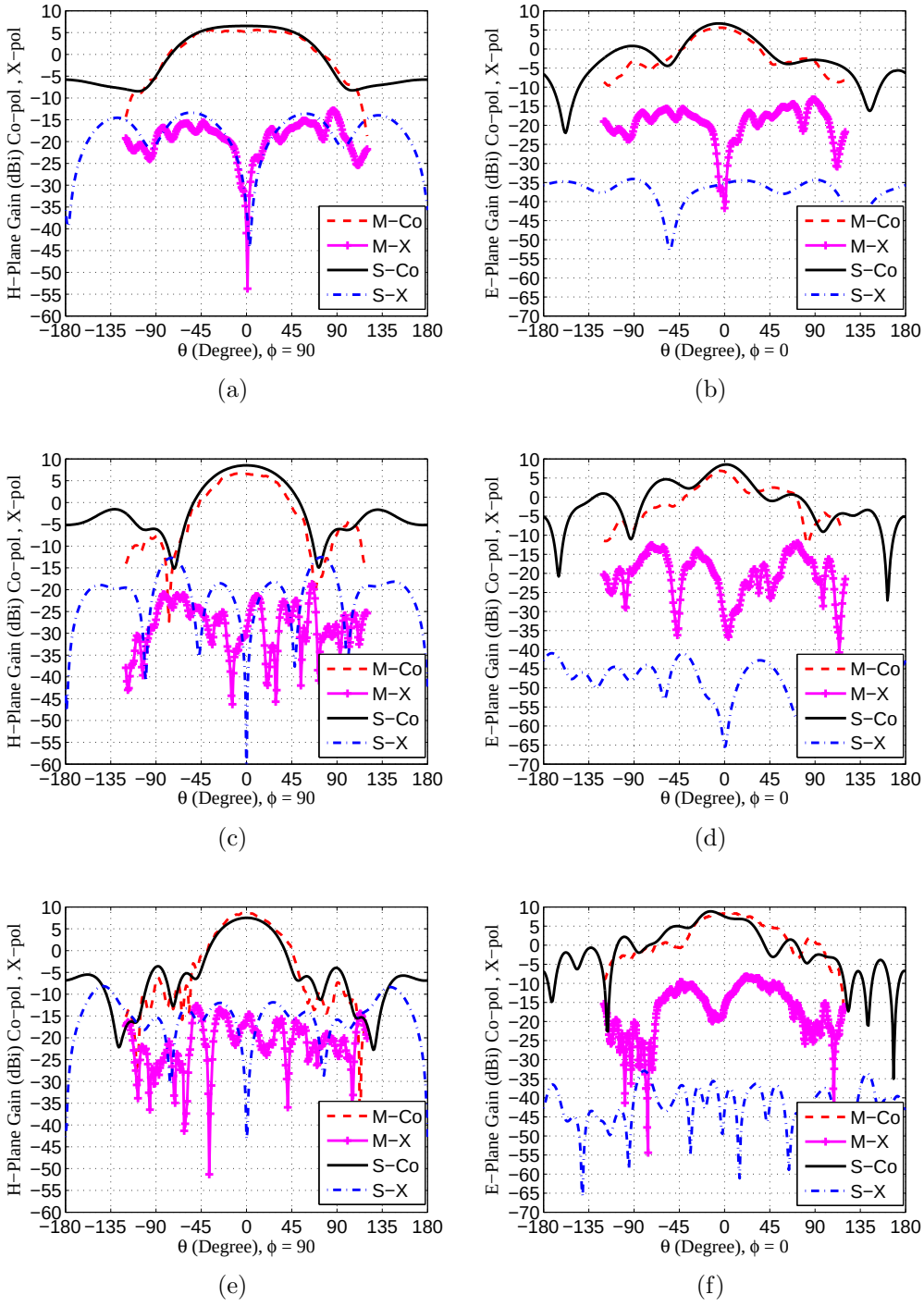

Figure 3.4: Comparison of the simulated (S) and measured (M) Co- and X-pol gain patterns of the DLVA. (a,c,e) H-plane at 3.7 GHz, 6.7 GHz, and 9.7 GHz, respectively. (b,d,f) E-plane at 3.7 GHz, 6.7 GHz, and 9.7 GHz, respectively.

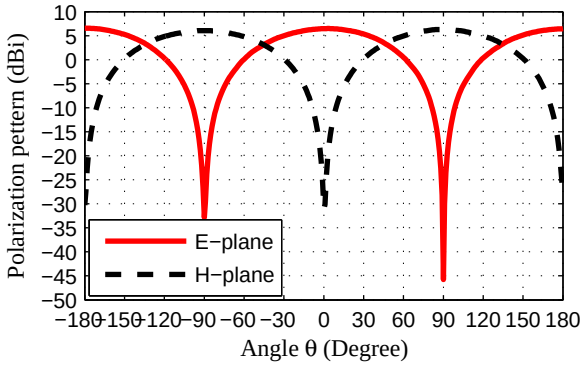

Figure 3.5: Polarization patterns of the antenna at 6.7GHz (see Figure 3.3).

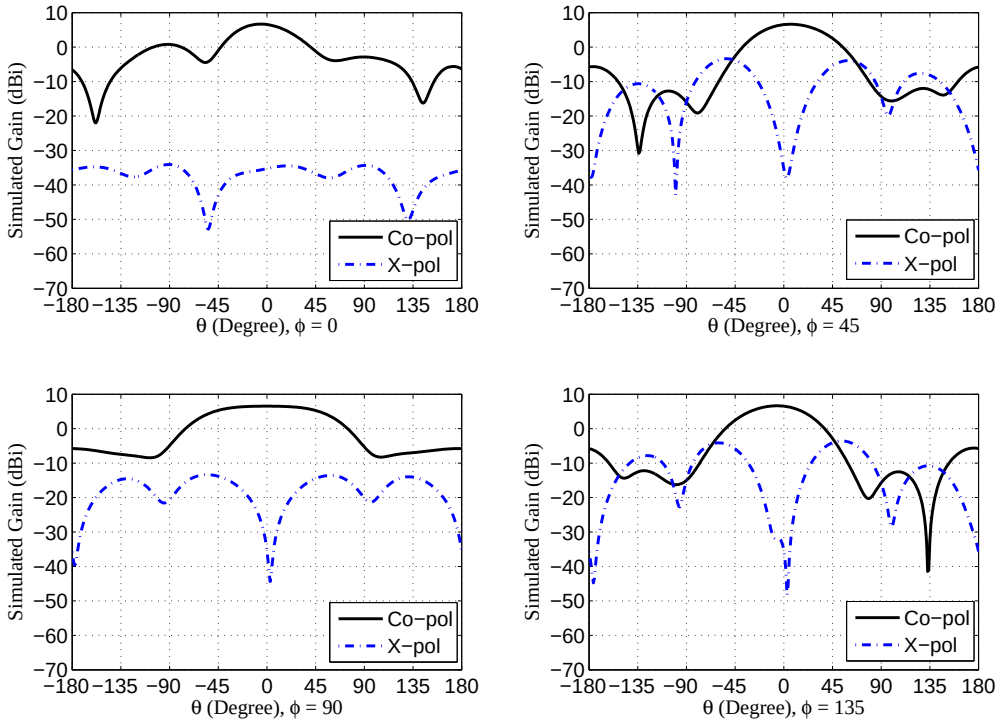

Figure 3.6: DLVA simulated Co- and X-pol gain patterns at 3.7 GHz at planes $\phi = 0°$, $\phi = 45°$, $\phi = 90°$, and $\phi = 135°$.

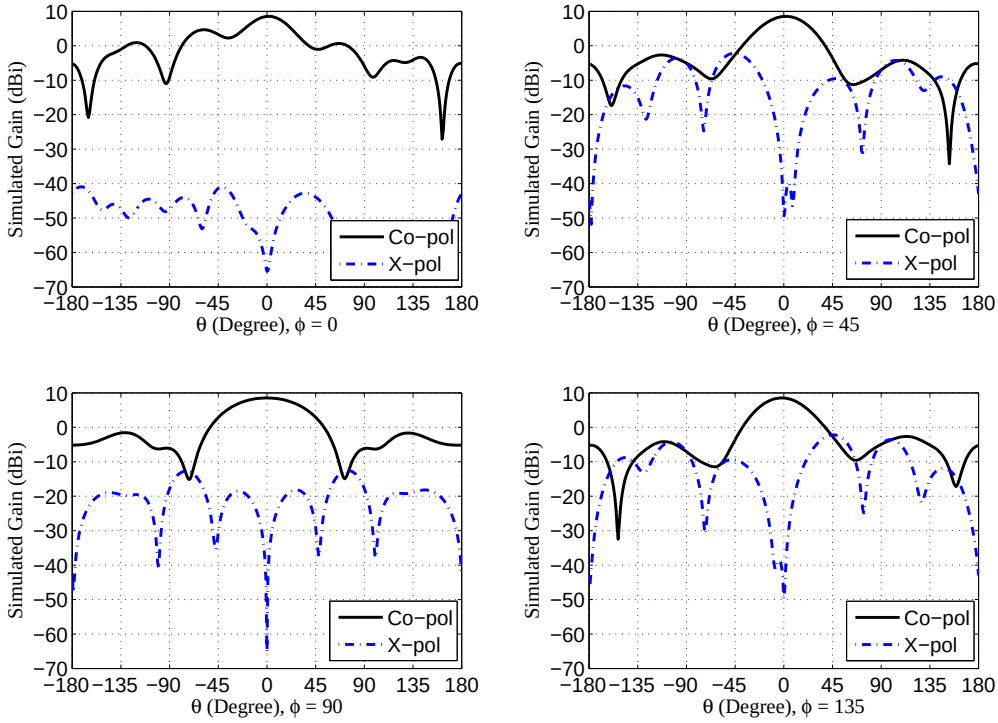

Figure 3.7: DLVA simulated Co- and X-pol gain patterns at 6.7 GHz at planes $\phi = 0°$, $\phi = 45°$, $\phi = 90°$, and $\phi = 135°$.

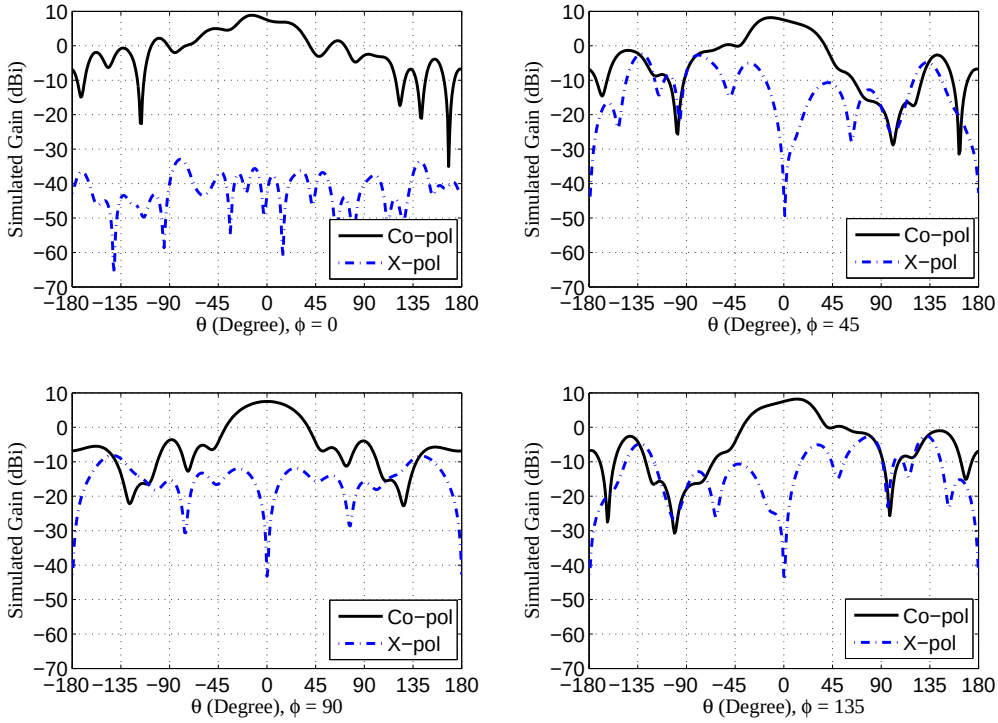

Figure 3.8: DLVA simulated Co- and X-pol gain patterns at 9.7 GHz at planes $\phi = 0°$, $\phi = 45°$, $\phi = 90°$, and $\phi = 135°$.

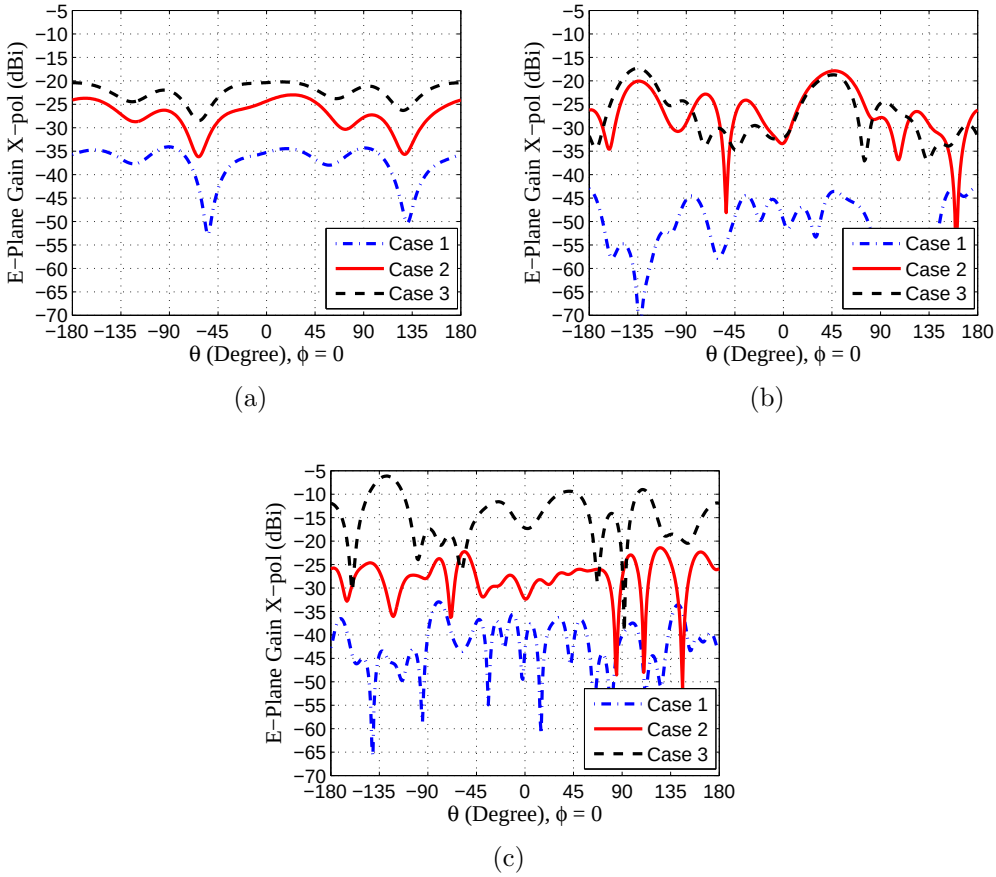

Figure 3.9: Effect of fabrication error on simulated E-plane X-pol level. (a) 3.7GHz, (b) 6.7GHz, and (c) 9.7GHz

divided into two regions: the radiating and the feeding regions. The radiating region generates end-fire radiation while the feeding region is connected to an unbalanced 50 Ω feed line. The latter consists of two terminals which are connected to the radiating region and a 50 Ω feed line, respectively. The two terminals do not necessarily have the same impedance nor the same structure. The feeding region should be designed in such a way that so as to match the two terminals to the line impedance and the input impedance of the radiating region. The design steps are listed as follows:

1. Designing the radiating region: There are different choices for tapering. The exponential tapering was chosen as depicted in Figure 3.10. Design details for this region are similar to the ones explained in Section 3.1.2 [65]. The radiating region is very similar to that of the DLVA antenna; however in this design, the two radiation flares are on the same plane on a single side of the substrate. The reason behind this choice is due to the high fabrication sensitivity of the DLVA that significantly increases cross polarization components (in the order of 15 dB average, see Section 3.1.4). Basically, the radiating region consists of four-quarter ellipses: C_{out}, C_{in} in Figure 3.10, and their mirrors with respect to the $z-$ axis. In this design, the radiation region length (L_r), the aperture width (L_a), the flare width on the $x-$ axis (W_f), and the gap between the left and right flares (G) are 40 mm, 50 mm, 1.5 mm, and 0.2 mm, respectively. Each of the outer and inner ellipses (C_{out}, C_{in}) consists of the horizontal (R_h, along $x-$ axis) and vertical (R_v, along $z-$ axis) radii, whose lengths are listed here (similar to Figure 3.1 (b)):

$$C_{out} : R_v = 50\text{mm},\ R_h = 60\text{mm} \qquad C_{in} : R_v = 40\text{mm},\ R_h = 200\text{mm}$$

2. Calculating the radiating region impedance: As shown in Figure 3.10, the far end of the radiating region is free space whose wave impedance is 120 Ω. The radiation region input impedance, Z_{0out}, is symmetric and is not necessarily 50 Ω. Using the FEM (Ansoft HFSS [63]), the characteristic impedance of Z_{0out} is evaluated as

$$Z_{0out} = \frac{P}{I^2}, \quad P = \int_S \mathbf{E} \times \mathbf{H}^* \cdot d\mathbf{s}, \quad I = \int_C \mathbf{H} \cdot d\mathbf{l} \tag{3.4}$$

where **E** and **H** are the electric and magnetic fields at the antenna aperture. P is the power passing through the Z_{0out} FEM port with aperture S, and I is the port current, computed by applying Ampere's law integration on the port boundary C. In this design the average evaluated impedance within the frequency range of interest is 104.4 Ω.

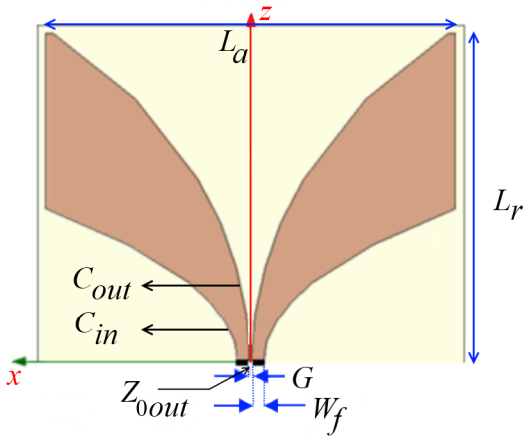

Figure 3.10: TSA radiating region.

3. Designing the structure of the feeding region: The feeding region should be designed such that it matches $Z_{0in} = 50$ Ω to Z_{0out} (here 104.4 Ω) over a wide frequency range. In the DLVA design of Section 3.1.2 , because the radiating

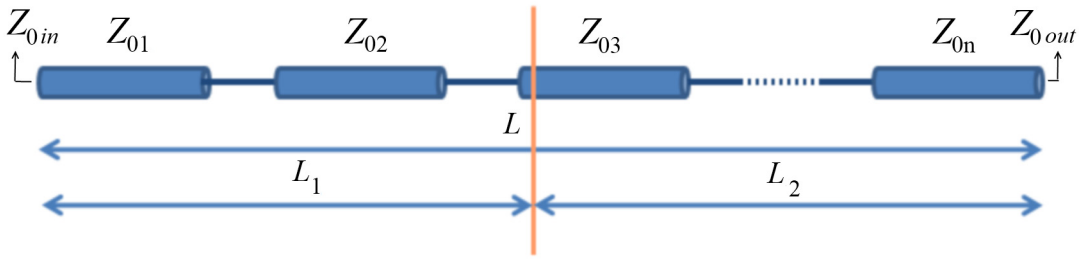

Figure 3.11: Implementing a series of cascaded transmission line sections for the unbalanced (L_1) and balanced (L_2) sections of feeding region.

region was implemented on different sides of the substrate, an exponential tapering from the 50 Ω stripline to Z_{0out} was used; however in this design, the entire radiating region is implemented on one side of the substrate. A series of TL sections are cascaded between the two ports of Z_{0in} and Z_{0out}; half of them contain 3 conductors (similar in structure to the 50 Ω feed) and the remaining should contain 2 conductors (similar in structure to the radiating region). These TL sections are referred to as unbalanced and balanced sections, respectively. A diagram of the TL sections is shown in Figure 3.11. The lengths L_1 and L_2 in this figure correspond to the unbalanced and balanced sections, respectively.

4. Designing the transmission line sections: In this step, regardless of the unbalanced or balanced geometry of the line, the number, the length, and the characteristic impedances of the transmission lines should be calculated such that the optimum matching between the Z_{0in} and Z_{0out} ports is achieved. As the first iteration, a distribution of 6 equal length sections ,$Z_{01} - Z_{06}$, was used each of which is 6 mm in length, between $Z_{0in} = 50\Omega$ and $Z_{0out} = 104.4\Omega$. The Frequency range of interest is chosen to be 5 GHz to 10 GHz. Using Ansoft Designer circuit solver [63], the equal length and the characteristic impedances of $Z_{01} - Z_{06}$ were optimized to achieve a wide frequency match between Z_{0in}

and Z_{0out}. A constraint for the maximum length of sections to be less than 7 mm was applied, in order to minimize the length of the antenna. A reflection coefficient less than -10 dB was achieved, using 6 TL sections. The optimized values for Z_{0in} to Z_{0out} are 50.0, 58.0, 62.8, 80.5, 90.2, and 104.4 Ω and the length of each section is 6 mm.

5. Choosing a transmission line geometry: There are many TL structures that can be selected for the TL sections. In this design, half of Z_{0i}s in the feeding region are unbalanced sections (L_1), and the remaining are balanced (L_2). A Coplanar Waveguide (CPW) transmission line was selected for Z_{0in}, a so-called Three-Ground Coplanar Waveguide (3G-CPW) transmission line for Z_{01} to Z_{03}, Asymmetric Parallel Plate (APP) transmission lines for Z_{04} to Z_{06}, and a symmetric parallel plate transmission line for Z_{0out}. All of these TLs are illustrated in Figure 3.13 (a). 3G-CPW and APP should have the same characteristic impedance at the intersection point: here Z_{03}, and Z_{04}.

6. Evaluating the transmission line dimensions: From step 4, the Z_{0i}s, and from step 5, the type of transmission lines are known. If the transmission line is a standard type, calculating the dimensions of each section is analytically possible. However, 3G-CPW and parallel plate configurations are not standard transmission lines. Therefore transmission line theory was incorporated to evaluate their dimensions. The characteristic impedance of a transmission line is calculated from (3.5) [66]

$$Z_{0i} = \sqrt{\frac{R_i + j\omega L_i}{G_i + j\omega C_i}} \tag{3.5}$$

where L_i, C_i, R_i, and G_i are the inductance, capacitance, resistance, and con-

ductance, respectively, per unit length of the i^{th} section, and ω is the angular frequency. Using a low loss substrate such as DiClad 527 in this design (loss tangent of 0.0022) with the Copper laminate (conductivity of 5.88E07 S/m), R_i, and G_i are negligible. Thus equation (3.5) simplifies to

$$Z_{0i} \approx \sqrt{\frac{L_i}{C_i}} \tag{3.6}$$

The substrate is non magnetic and its permeability is constant. Therefore L_i does not change by replacing the substrate with air. When the substrate is air the medium is homogeneous and the velocity of propagation can be found as that of the air, therefore $L_i\ C_{0i} = \mu_0\ \epsilon_0$. Finally Z_{0i} is found as

$$Z_{0i} = \sqrt{\frac{\mu_0\ \epsilon_0}{C_{0i}\ C_i}} \tag{3.7}$$

where μ_0 and ϵ_0 are the free space permeability and permittivity, respectively. C_{0i} is the per unit length capacitance of the i^{th} section when the substrate is air. From (3.7), one can see that it is only needed to calculate the per unit length capacitance of each section, once with the dielectric substrate and once with air. In order to evaluate these per unit length capacitances, Comsol Multiphysics software [67] was utilized which is an accurate numerical technique for inhomogeneous media based on the FEM. The cross-sections of the 3G-CPW and the parallel plate TLs were modeled using a 2D electrostatic environment. The domain size for the FEM solver was chosen to be $40h$, where h is the substrate thickness and is equal to 62.5 mil. A typical meshing of the geometry for the 3G-CPW is illustrated in Figure 3.12. By applying a reference voltage to the main conductors, the electrostatic total electric energy in the enclosure

was calculated, once with the dielectric substrate (C_i) and once with the air substrate (C_{0i}). The per unit length capacitance is twice the energy divided by the reference voltage squared.

To convert the Z_{0i}s to physical dimensions, a look-up table for the characteristic impedances of the 3G-CPW and parallel plate TL as a function of different dimensions was created. There are several structures that can provide each Z_{0i}, hence there is no unique solution. In order to create the look-up table, the geometry of the 3G-CPW and parallel plate TL structures were defined in Matlab. The Matlab program sweeps various dimensions of these transmission lines and calls the FEM solver for each dimension to evaluate C_i and C_{0i}. Then, it calculates the characteristic impedance using (3.7). This program was utilized to provide a look-up table for corresponding characteristic impedances of the 3G-CPW or parallel plate geometries. Using these look-up tables, 6 different structures to arrive at the final result were examined. These structures are depicted in Figure 3.14. The geometry with a symmetric structure was chosen, which resembles two eagles facing each other. This antenna was called EFVA and is shown in Figure 3.13. Table 3.2 lists the final dimensions and characteristic impedances. In this table, W_l and W_r stand for the widths of the left and right conductor strips in the APP section, depicted in Figure 3.13, respectively. Wg_l, Wc_l, Wc_r, and Wg_r, stand for left ground, left center conductor, right center conductor and right ground widths, respectively. Wc and Ws stand for center conductor width and the separation distance for the initial feed line, respectively. This section belongs to CPW transmission line.

The fabricated antenna and reflection coefficient are shown in Figure 3.13 (b) and Figure 3.15, respectively. The antenna shows a reflection coefficient of less than -

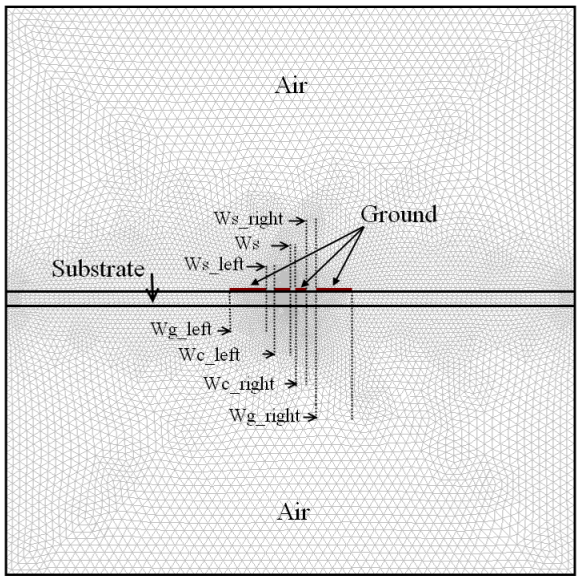

Figure 3.12: FEM mesh to calculate the per unit length parameters for 3G-CPW.

10 dB in the 2 GHz to 16 GHz frequency range (except for a -9 dB level at 6.4 GHz). The typical radiation patterns of EFVA in both E-plane and H-plane at 6.7 GHz are depicted in Figure 3.16. This particular frequency was chosen arbitrarily and the results are similar for other frequencies. The E-plane is the antenna plane $(x - z)$ and H-plane is the $(y - z)$ plane. The measurements were conducted in the compact antenna range of the University of Manitoba, with a cross polarization level of about -35 dB. Cross polarization components are less than -15 dB in the end-fire direction (z- axis) within the 2 GHz to 10 GHz frequency band.

3.1.6 Single Layered Y-Y fed Vivaldi Antenna (SLYVA)

The DLVA and EFVA utilize a direct connection of the feed line to the radiation region. Another approach to implementing the Vivaldi antenna, is to build an indirect transition or balun, between the feed and the radiation regions. One configuration for this approach is a microstrip to slot-line transition, or simply "Y-Y".

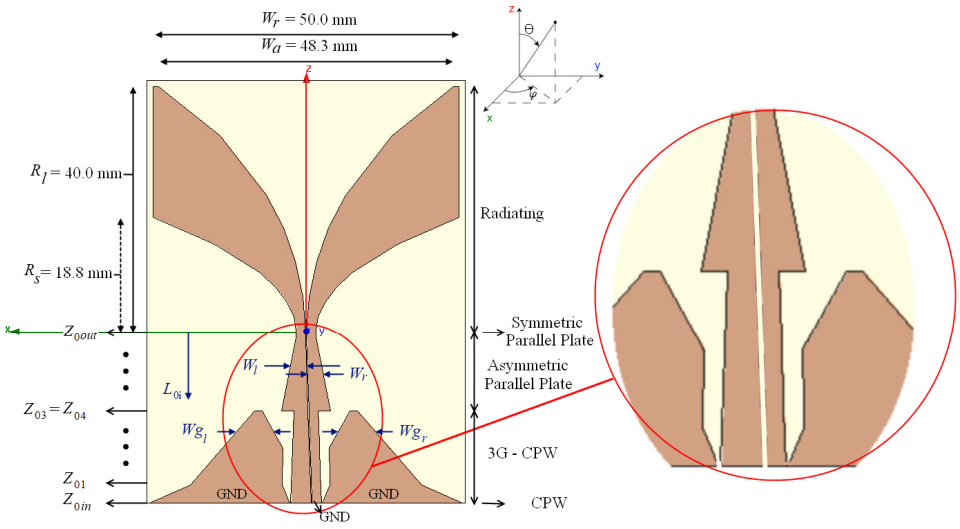

(a)

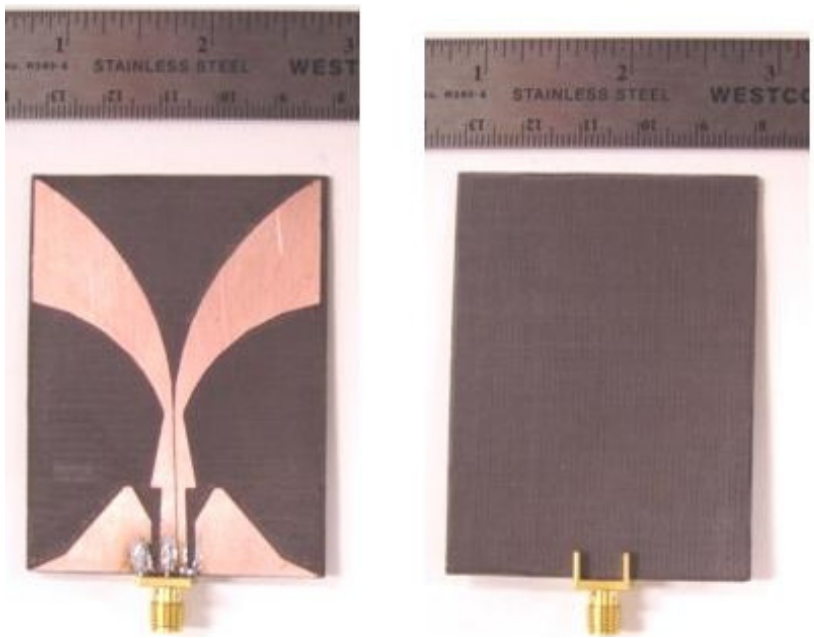

(b)

Figure 3.13: EFVA: (a) dimensions, and (b) fabricated antenna.

Table 3.2: Dimensions and characteristic impedances of EFVA, see Figure 3.13

		$Z_{0i}(\Omega)$	L_{0i} (mm)	W_l, Ws, W_r (mm)	Wg_l, Ws_l, Wc_l, Ws, Wc_r, Ws_r, Wg_r (mm)	Wc, Ws (mm)
CPW	Z_{0in}	50.0	28.0			3.2, 0.2
3G-CPW	Z_{01}	58.0	25.0		15.0, 1.5, 3.1, 0.2, 1.5, 1.5, 15.0	
	Z_{01}	62.8	19.0		9.9, 1.6, 2.7, 0.2, 1.5, 1.6, 9.9	
	Z_{03}	80.5	13.0		1.2, 5.2, 2.3, 0.2, 1.5, 5.2, 1.25	
Asymmetric Parallel Plate	Z_{04}	80.5	13.0	4.3, 0.2, 3.5		
	Z_{05}	90.2	7.0	2.9, 0.2, 2.5		
	Z_{06}	104.4	1.0	1.5, 0.2, 1.5		
Radiation	Z_{0out}	104.4	0	1.5, 0.2, 1.5		

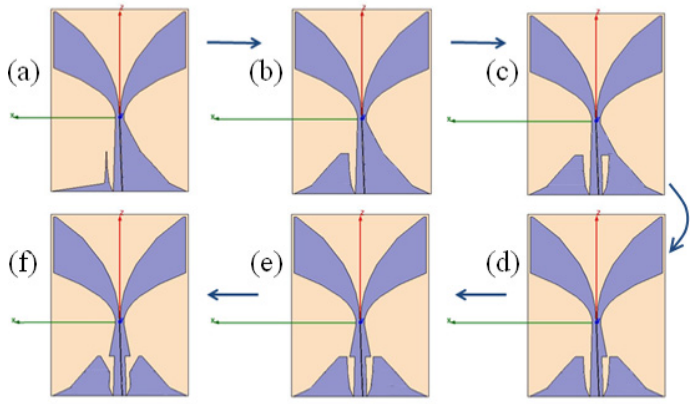

Figure 3.14: EFVA design solutions due to different possible dimensions for a specific characteristic impedance.

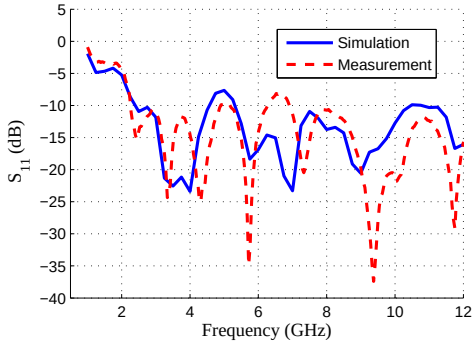

Figure 3.15: EFVA reflection coefficient: simulation and measurement.

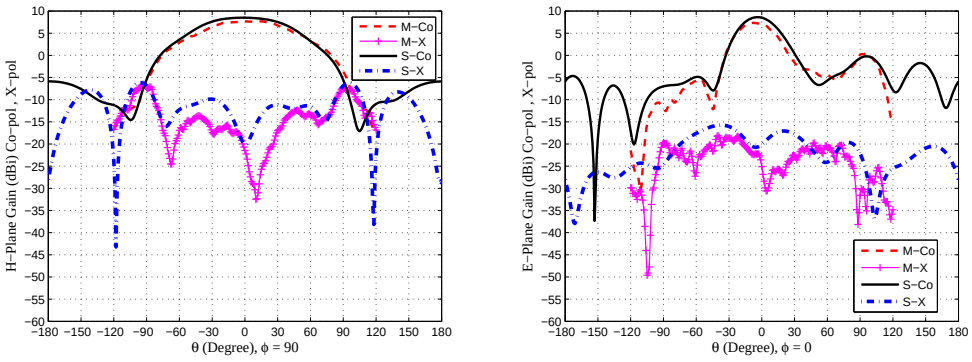

(a) (b)

Figure 3.16: EFVA typical Co-pol (Co) and X-pol (X) radiation patterns at 6.7 GHz, M: Measurement, S: Simulation. (a) H-plane, (b) E-plane.

Using this configuration, a Single Layered Y-Y fed Vivaldi Antenna (SLYVA) was fabricated. The SLYVA employs a combination of a perpendicular short circuit microstrip line and an open circuit slot line in order to couple the feeding region to the radiating region. One way of improving this method is to extend the junction of microstrip-slot line to a double junction, which results in a 6-port microstrip-slot line transformer and balun [68]. This method of feeding is called Y-Y feed, where the unbalanced microstrip input line is divided into two parallel branches: one short circuit and one open circuit. On the other side of the substrate, the slot line is also divided into two parallel branches: one open circuit and one short circuit. Using the method described by [68], and [69], a SLYVA to operate in 3 GHz to 7 GHz was designed. The geometry and fabricated antenna are shown in Figure 3.17. The antenna external dimensions are 60 mm by 61 mm.

The antenna reflection coefficient is depicted in Figure 3.18. Measurement results show that the antenna covers the 3 GHz to 7 GHz frequency range as expected. Also E-plane ($x-z$) and H-plane ($y-z$) radiation patterns were measured and compared with simulation results. A typical pattern at 6.7 GHz is shown in Figure 3.19. The

cross polarization component in the end-fire direction is less than -15 dB in the entire operation frequency band.

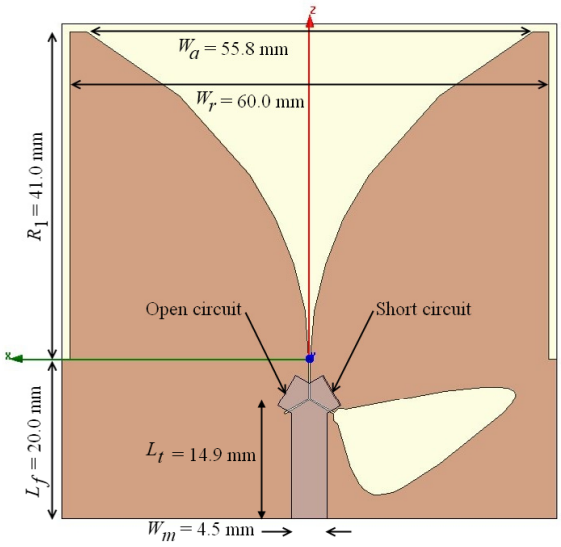

(a)

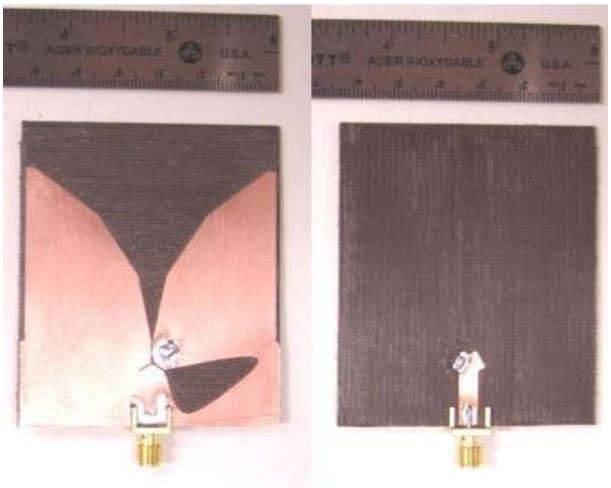

(b)

Figure 3.17: SLYVA: (a) geometry and, (b) fabricated antenna.

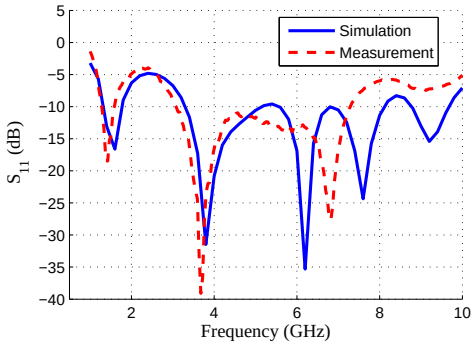

Figure 3.18: SLYVA reflection coefficient, simulation and measurement.

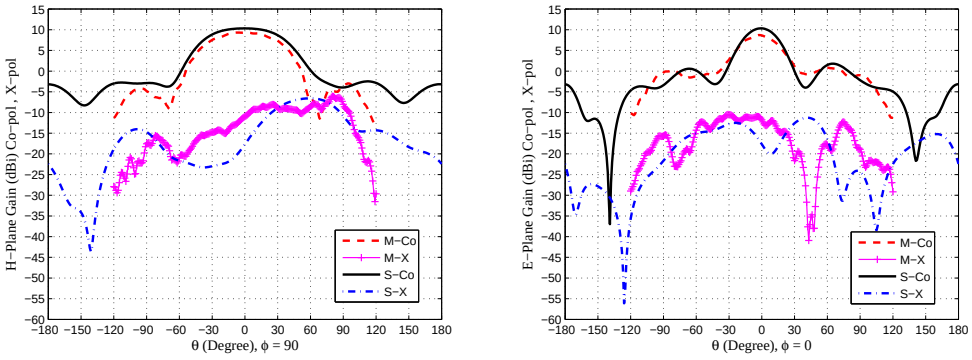

(a) (b)

Figure 3.19: SLYVA typical Co-pol (Co) and X-pol (X) radiation pattern at 6.7 GHz. M: Measurement, S: Simulation. (a) H-plane, (b) E-plane.

3.1.7 Comparison of Vivaldi Antennas and Conclusion

The design, fabrication and measurement-simulation results of three Vivaldi antennas have been presented. The DLVA, Section 3.1.1, with a smooth tapering of the stripline feed to the radiating region, features an overall size of 70 mm by 70 mm. Its impedance bandwidth covers the 3.3 GHz to 11 GHz with less than -10 dB reflection coefficient. The simulation results show that the DLVA cross polarization level is exceptionally low (less than -60 dB). However, measurement results show that the E-plane cross polarization is about -25 dB which still shows 10 dB better performance than the results obtained from the EFVA, Section 3.1.5 and the SLYVA, Section 3.1.6.

The measured reflection coefficients of the EFVA, SLYVA and DLVA are shown in Figure 3.20 in the frequency range of 2 GHz to 18 GHz. Among these antennas, the SLYVA shows the smallest impedance bandwidth, compared to the EFVA and the DLVA. The end-fire gains of the three antennas are depicted in Figure 3.21. The Co-pol gain of the three antennas are close to each other, especially at frequencies higher than 5.5 GHz. Their gain changes from 5 dBi at 5 GHz to 10 dBi at 12 GHz in the end-fire direction. The 3 dB Half Power Beam-Width (HPBW) of these antennas are compared in Table 3.3. For an MWT system, a maximum HPBW in the H-plane and minimum HPBW in the E-plane is required to illuminate a cross-sectional slice of the OI. The EFVA shows maximum HPBW in the H-plane at 6.7 GHz.

In conclusion, the EFVA shows the widest impedance bandwidth and HPBW, however, the cross polarization level of the DLVA is minimum among the three antennas. The drawback of the DLVA is its sensitivity to fabrication errors discussed in Section 3.1.4 but still shows the best measured X-pol level. As far as implementing a TM_z MWT system is concerned, the DLVA is the best Vivaldi candidate among the three Vivaldis being proposed. Using 24 co-resident DLVAs, a free-space MWT

system is implemented as described in the next section.

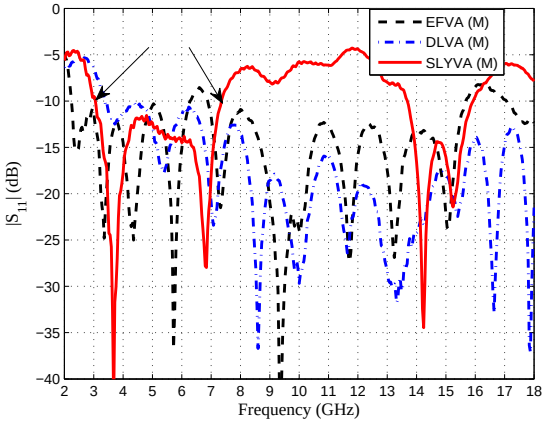

Figure 3.20: Comparing the measured reflection coefficient of EFVA, SLYVA, and DLVA.

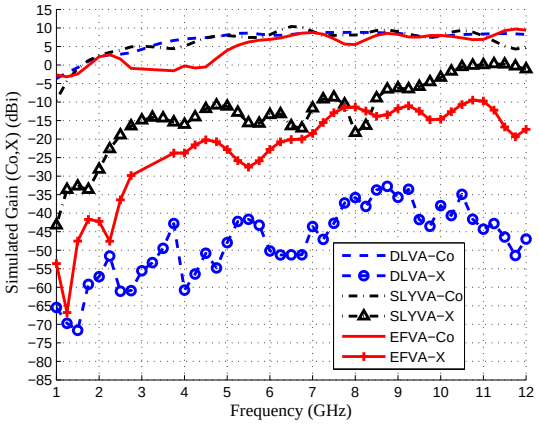

Figure 3.21: Comparing simulated end-fire gain Co-pol (Co) and X-pol (X) of DLVA, SLYVA, and EFVA versus frequency.

3.2 Microwave Tomography Apparatus

Twenty-four DLVAs were utilized encircling an OI to implement a *direct* MWT system. Using a Vector Network Analyzer (VNA) and a RF switch, the transmission

Table 3.3: Vivaldi antennas' HPBW in the E- and H- planes at 6.7 GHz.

	H-plane simulation	H-plane measurement	E-plane simulation	E-plane measurement
DLVA	69.1°	65.8°	39.0°	33.5°
EFVA	95.4°	95.71°	37.9°	39.4°
SLYVA	75.9°	71.2°	34.0°	38.3°

coefficients S_{ji}, between arbitrary transmitter Tx_i, and receiver Rx_j were collected. A data acquisition program controls the VNA and RF switch network through a General Purpose Interface Bus (GPIB) connection and records the measurements. In this section, the details of this system is reviewed.

3.2.1 Array of Antennas

The directive pattern and low X-pol level of the DLVA makes it a good candidate for a TM_z tomography system. Note that the tomography system is modeled using a 2D algorithm which only requires E_z component of electric fields. The cross polarization components of the antenna, can produce E_z fields after impinging the OI. Thus, improving the polarization characteristic of the antenna is a factor for choosing the antenna. Twenty-four DLVAs were fabricated and mounted on a Plexiglas cylinder of 45 cm diameter with equal angular spacing of 15°. The antennas are connected to a 2×24 mechanical RF switch network (Agilent 87050A-K24) using coaxial cables of equal lengths. The network analyzer (Agilent E-8363B) is directly connected to the switch network. This setup is shown in Figure 3.22 (a). To illuminate an entire cross-section of the object the DLVAs should be mounted vertically. In this situation the wider beam of the antenna pattern is in the cross-sectional plane of the object, while the narrower beam focuses the energy in this plane. The antennas are labeled

from 1 to 24, as shown in Figure 3.22 (b).

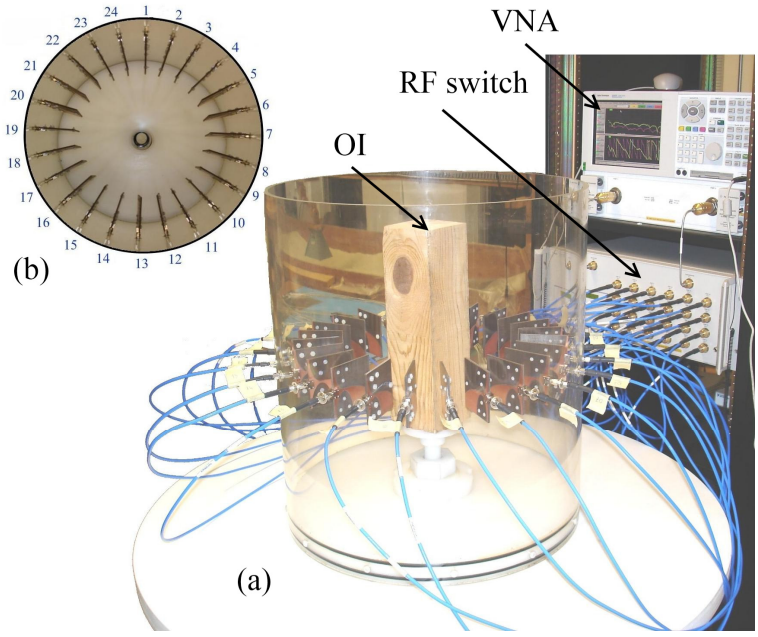

Figure 3.22: Measurement setup including 24 DLVA, (a) RF switch, VNA, and a wood cuboid as the OI, (b) top view.

To study the mutual coupling of the antennas, their performance alone and in the presence of the other antennas were compared, while mounted in a Plexiglas chamber. For this experiment a full 2-port calibration was performed, with port 1 as a reference and ports 2-23 as forward. The HP 85033D 3.5 mm kit was used for calibration. The kit is valid up to 6 GHz. Therefore, there might be some calibration error at higher frequencies (more than 6 GHz). Figure 3.23 (a),(b) show the amplitude and phase of the reflection coefficients of each DLVA, when the antenna is either in the presence of the other antennas or alone. As indicated in these figures, the reflection coefficient of the DLVA in presence of co-resident antennas is not the same as the one obtained when it is alone. The difference is higher at some frequencies between 3 GHz to 4.5 GHz. The difference in the reflection coefficient indicates the loading effects due to the presence of the co-resident antennas. It can also give an indication as to which

working frequencies should be selected for the microwave tomography operation. The image reconstruction error is lower at frequencies where the reflection coefficient is invariant [70]. One expects to improve this behavior by filling the enclosure with a lossy solution. However, lossy medium also causes attenuation in measuring scattered field.

Figure 3.24 shows the transmission between antenna #1 and other antennas and highlights the level of mutual coupling. As shown in this figure, the mutual coupling is less than -17 dB at frequencies higher than 4 GHz. Because of the directional pattern of the DLVA, fidelity parameter was studied as explained in [71], to measure how many receivers are uniformly illuminated by a transmitter. After a full 2-port calibration, the $S_{n\,1}$ for n = 2-24 are collected at 3059 sampling points within the frequency range of 3.3 GHz to 10 GHz. By assuming a perfect calibration at all frequencies, the time domain equivalent pulse of this spectrum is reconstructed in Matlab. Cross-correlation of the time derivative of this pulse and the measured pulse at each receiver indicates the similarity of the pulse shape between different antennas. Cross correlation of the i^{th} antenna is calculated from

$$Correlation^i = max_\tau \int_{-\infty}^{\infty} r(t-\tau) f^i(t) dt \tag{3.8}$$

where $f^i(t)$ is the received signal at i^{th} antenna and $r(t)$ is the time derivative of an ideal transmitted pulse. This cross-correlation is then normalized to the energy of both the transmitted and received signals and is called *fidelity* of each antenna. The energy is calculated by cross-correlation of each signal by itself. The calculation shows that when antenna #1 is the transmitter, the changes in fidelity of antennas #9 to #17 is less than 10%. Therefore by sending a pulse that covers the operating frequency range of 3.3 GHz to 10 GHz, the nine antennas in front of the transmitter

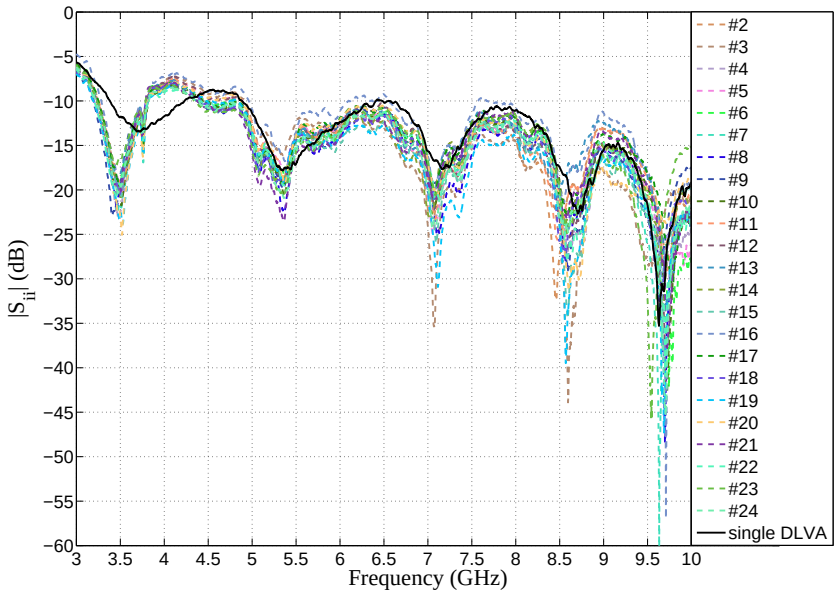

(a)

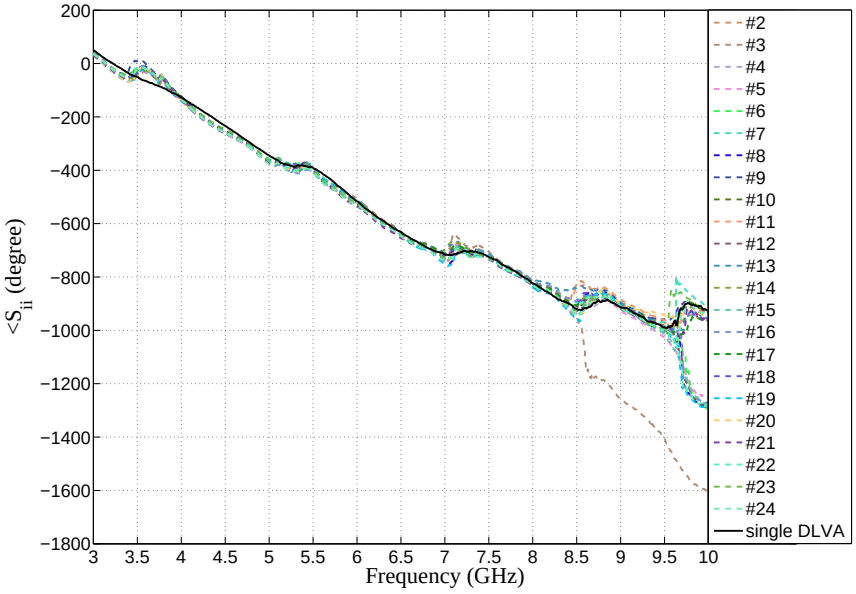

(b)

Figure 3.23: Reflection coefficient, S_{ii}, of each antenna in presence of co-resident DLVAs or alone. (a): amplitude (dB), (b) phase (degree).

will receive the expected pulse with less than 10% error. This shows a uniform illumination by the Tx antenna.

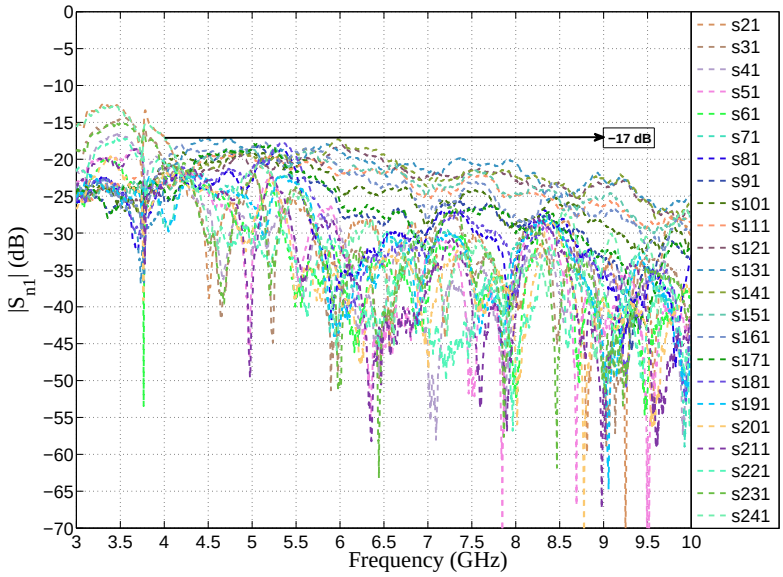

Figure 3.24: Amplitude (dB) of transmission coefficients, S_{n1}.

3.2.2 On the Frequencies of Inversion

Figure 3.23 compares the performance of a single DLVA alone and in the presence of the other antennas. As discussed in Section 3.2.1, these figures can determine at which frequencies the DLVAs are weakly or strongly coupled. As an example, there is a strong coupling at 3.5 GHz and 4.0 GHz, while the coupling is weak at 3.0 GHz and 4.5 GHz. It is speculated that the weak coupling with the co-resident antennas provides more reliable data for image reconstruction. At frequencies with strong mutual coupling, usually the inversion algorithm (CSI and GNI) fails to reconstruct the image. As shown in [70], the analytical scattered fields by a PEC cylinder does not well match to the measured scattered fields at frequencies with strong mutual

coupling. Thus, the measured data needs to be strongly "manipulated" within the calibration procedure at these frequencies. As a result, imaging algorithms do not usually converge at these frequencies. On the other hand, the frequencies with weak mutual coupling present closer results to the analytical counterpart of the calibration object and the chance of successful inversion is higher at these frequencies.

As an inversion example, using this experimental system and the enhanced DBIM and CSI algorithms, the relative complex permittivity of a wood cuboid and a nylon rod is reconstructed at 3 GHz, where the mutual coupling is weak. This object is shown in Figure 3.25. The nylon diameter is 1.5 inch (38 mm). The wood dimensions are 87 $\times$ 88 mm. The complex permittivity of nylon is $\epsilon_r^{nylon} = 3.0 - j0.03$ at 3 GHz [36]. The complex permittivity of wood was measured using the Agilent 85070E dielectric probe kit, at all of its four side-faces. The average permittivity at 3 GHz is $\epsilon_r^{wood} = 2.0 - j0.20$. The object was positioned at the center of the measurement chamber. The reconstructed images of the two algorithms are illustrated in Figure 3.26. The inversion of another object as well as other weekly coupled frequencies such as 4.5 GHz and 6 GHz, are also reported in [70].

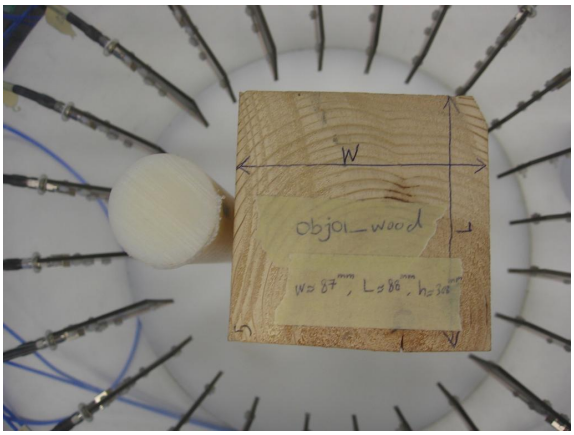

Figure 3.25: The picture of a wood-nylon object for image reconstruction.

3.3 Conclusion

In this chapter different antenna design techniques were presented to be utilized in a broadband MWT system with TM_z polarization. The DLVA, EFVA, and SLYVA antennas were discussed and the DLVA, due to the lowest X-pol level was selected for the MWT system.

Next, the UM MWT system was described, utilizing 24 co-resident DLVAs. The performance of the antenna alone, and in presence of other DLVAs was studied and a frequency selection procedure based on the strong/weak mutual coupling was introduced. Inversion results of this system at *well-behaved* frequencies were presented. The enhanced DBIM and CSI algorithms were utilized for the image reconstruction.

In an experimental tomography system, different field polarizations exist. Even by illuminating the OI by a single polarized incident field, the scattered field may have all field polarizations, depending on the OI. Since in this implementation only 2D algorithms are utilized with the E_z component, the cross-polarization component of the Tx antennas may generate an unwanted E_z component after impinging on the OI. Furthermore, the co-polarization component of the Tx antennas may generate a cross-polarization component at the receiver antennas. All these components contribute in the received voltage by the Rx antenna and generate a measurement error which is referred to as the polarization error. In order to reduce polarization error and increase the measurement accuracy, 1) an antenna with zero or negligible cross polarization must be used as the Tx antenna (here a DLVA has been utilized), and/or 2) a technique to accurately measure a single polarization at the receiver stations should be developed (a novel system addressing the receiver polarization is introduced in Chapter 6). There are other sources of error *e.g.* resulting from 2D modeling of a 3D wave propagation phenomenon. Calibration techniques can be developed specifically

to minimize some of these specific errors. Some of these techniques are discussed in greater detail in chapter 4.

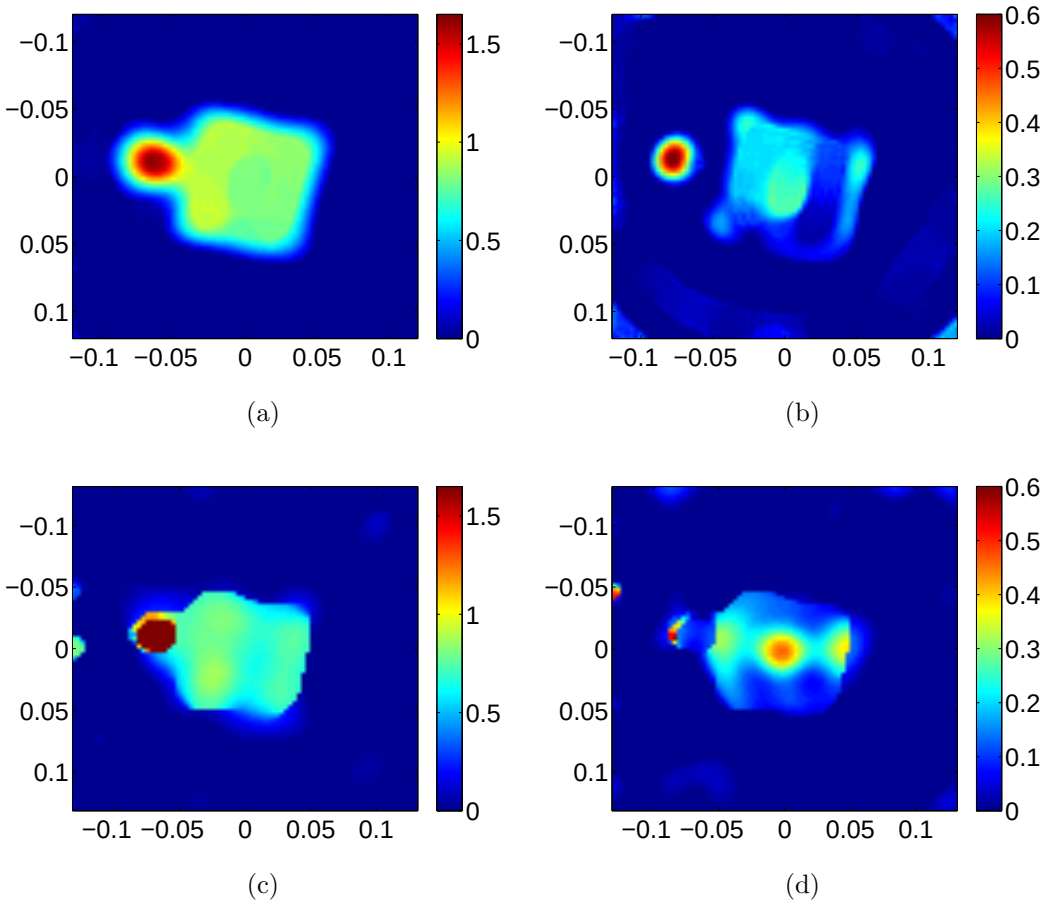

Figure 3.26: Reconstructed image of wood-nylon object at 3.0 GHz. Real (a), and imaginary (b) parts of contrast χ from DBIM method. Real (c), and imaginary (d) parts of contrast χ from CSI method.

Chapter 4

Analysis of Incident Field Modeling and Calibration Techniques

In MWT an inverse scattering algorithm is utilized to reconstruct the image from the measurement data, as discussed in Chapter 2 and Section 3.2. Inversion algorithms typically assume an idealized electromagnetic model of the physical system which simplifies, or ignores, the antennas (field-probes), the finite extent of the imaging chamber, as well as cables leading from the Tx/Rx instrumentation to the antennas. In addition, though only circuit quantities can be directly measured, most inversion algorithms require field values at appropriate spatial locations/regions within their assumed electromagnetic model. For example, the cost function of both the GNI [22], and the CSI [23] techniques require scattered field quantities at several measurement points surrounding the OI as well as an accurate characterization of the incident field inside the imaging domain. In both GNI and CSI the modeled incident field appears directly in the cost functions which are minimized: equations (2.26) and (2.30), respectively. This leads to constraints on the design of MWT systems, *e.g.*, the use of antennas that can be modeled simply and the use of a lossy matching fluid so that the mutual coupling between co-resident antennas as well as the effect of the chamber boundaries and feed cables can be minimized. Even when such design considerations are taken into account, calibration factors must still be used to translate the measured circuit quantities into the required scattered field quantities at the

model-defined measurement points, and the incident field used in the algorithms will still only approximate the true incident field. The resulting error, due to these two factors, contribute to what is called modeling error. Calibration of an MWT system includes dealing with both of these factors.

In this chapter, this calibration task is studied as it relates to typical co-resident antenna MWT systems in existence. As mentioned in Section 3.1 different antennas have been utilized in co-resident MWT systems *e.g.* monopoles [11] and open-ended loaded waveguides [72] seem to be two of the most popular ones, probably because they can be replaced by relatively accurate simple models in the inversion algorithm. None the less, somewhat more complicated antennas have been used successfully as in the UM air-based MWT system which utilizes 24 co-resident DLVAs. Due to the heavy computational cost, these antennas are not fully modeled in MWT imaging algorithms [72, 73], even for more sophisticated 3D inversions [11, 17, 41]. Thus, calibration means determining an acceptably accurate incident field to be used in the imaging algorithm and determining calibration factors which convert the measured quantities to field values at particular positions.

In the past, the incident field characterization has mostly been handled by modeling the transmitting antenna as a line-source at an appropriate location. More complicated models have employed an array of line sources [74]. Experimentally sampling the incident field directly inside the imaging domain has also been reported, wherein the field is then modeled as an exponentially damped plane wave [75].

A method of determining calibration factors is to place a canonical reference object inside the imaging domain and then form the ratio of analytically or numerically derived scattered field values at the observation points for this object positioned inside the electromagnetic model's chamber to the values measured by the corresponding

antennas in the actual system. This methodology is called scattered field calibration [34] and the ratios are called the scattered field calibration coefficients. If the incident field is used to determine these factors, the technique is called incident field calibration [76]. The canonical reference object is usually an object with high permittivity compared to the background medium, such as a Polyvinyl Chloride (PVC) cylinder in water [75], or a PEC object [34, 70].

In order to study the effect of different incident field approximations and methods of finding calibration factors, the air-based MWT system is fully simulated to obtain an accurate incident field. The fields obtained from the 3D-model and a line-source approximation are compared inside imaging domain $\mathcal{D}$ as well as on measurement domain $\mathcal{S}$. The two domains are illustrated in Figure 4.1 (a). Then the images of two dielectric phantom tests are reconstructed by the GNI algorithm, where the incident field from the 3D-model or the line-source approximation is incorporated into both inversion algorithm and as well as the calculation of the corresponding calibration coefficients.

The all four combinations of the incident field models and the calibration techniques used herein, are listed in Table 4.1. Using these different incident fields and calibration techniques, the resultant images of experimental data are analyzed from the air-based system, to determine the affects each parameter has on the imaging results. The mean and standard deviation of the imaging results, as well as the fields are compared in different regions. Due to the use of different antennas in current MWT systems, with/without a lossy background medium, the associated incident field is different for each system as well as the mutual coupling of the co-resident antennas. Thus, a unique calibration method cannot be applied for all tomography systems. However, this study provides information on the benefits and/or disadvan-

tages of different techniques for an MWT system, where there is no background loss to reduce the mutual coupling.

Table 4.1: Incident field modelings and calibration techniques.

		Calibration technique	
		Incident	Scattered
Incident field	Line-source	$\mathcal{C}_{\mathcal{F}_{ls}}^{inc}$, E_{ls}^{inc}	$\mathcal{C}_{\mathcal{F}_{ls}}^{sct}$, E_{ls}^{inc}
	3D-model	$\mathcal{C}_{\mathcal{F}_{3D}}^{inc}$, E_{3D}^{inc}	$\mathcal{C}_{\mathcal{F}_{3D}}^{sct}$, E_{3D}^{inc}

4.1 Field Comparison

The inversion algorithm requires the incident field inside imaging domain,$\mathcal{D}$, as well as the fields at $\mathcal{S}$. In order to calibrate the data, the fields scattered by a known object, here a PEC cylinder-3.5 inch diameter, are required at $\mathcal{S}$, however the fields inside $\mathcal{D}$ cannot be measured. In the first part of this section, the incident field inside $\mathcal{D}$ obtained from the line-source approximation and the 3D-model are compared. In the second part, the incident and the field scattered by the calibration object on $\mathcal{S}$ are compared, including the measured data.

4.1.1 Fields Inside the Imaging Domain

Twenty-four co-resident DLVAs were fully simulated with FEM using Ansoft-HFSS [63]. The 3D-model schematic is shown in Figure 4.1 (b). The incident field is then extracted at the $x-y$ plane ($z=0$) cross-section and is denoted by E_{3D}^{inc}. On the other hand, a line-source approximation model uses line-sources parallel to the $z-$ axis at the DLVA locations. The DLVA source antenna is 7 cm in length, thus the placement of the equivalent line-source is ambiguous and the best location must be

found by modeling. Here weve placed them 1 cm from the front-end of the antenna. The incident field of a line-source is denoted by E_{ls}^{inc} and is calculated as

$$E_{ls}^{inc} = \frac{1}{4j} H_0^{(2)}(k_0 \left|\mathbf{r} - \mathbf{r}_0\right|) \tag{4.1}$$

where $H_0^{(2)}$ was introduced in (2.14). $\mathbf{r}$ and $\mathbf{r}_0$ represent the observation point and the source point position vectors, respectively.

The amplitude and phase of the E_{3D}^{inc} and E_{ls}^{inc} inside $\mathcal{D}$ are shown in Figure 4.2 where the antenna #1 or #4 are the transmitters (see Figure 4.1 (a)). Note that the co-resident array produces fields substantially different from those of a line-source.

4.1.2 Fields on the Measurement Domain

The incident fields from the 3D-model and the line-source model are computed at $\mathcal{S}$, when the antenna #1 is the transmitter. The incident field is also measured using the DLVAs' S-parameter measurement as discussed in section 3.2. The amplitude and phase for these three cases are shown in the first row of Fig. 4.3. Note that the measurements do not deal with the calibration technique, at this time.

Next, the field scattered by the PEC calibration object is computed. First, the scattered field is calculated when the transmitter is approximated by a line-source. Then a 2D forward solver (the Method of Moments [22]) was utilized to compute the scattered fields using the incident field obtained from the 3D-model (E_{3D}^{inc}). Finally the scattered field by the PEC cylinder was measured at 5 GHz, using the DLVAs' S-parameter measurement. The amplitude and phase of the scattered field on $\mathcal{S}$ for these three cases are shown in the second row of Figure 4.3. Again, note the difference between the line-source incident field and the actual field. Also note that the scattered

fields are a better match between all three cases than the incident field.

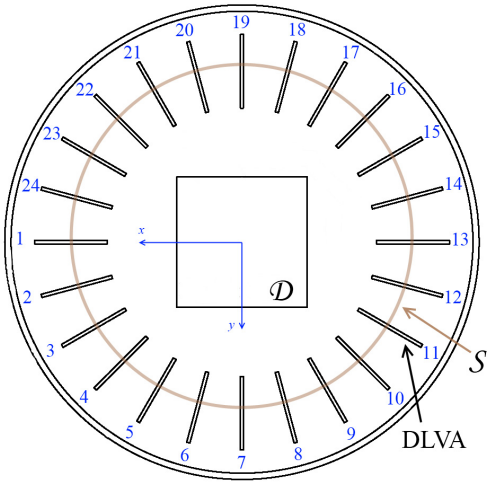

(a)

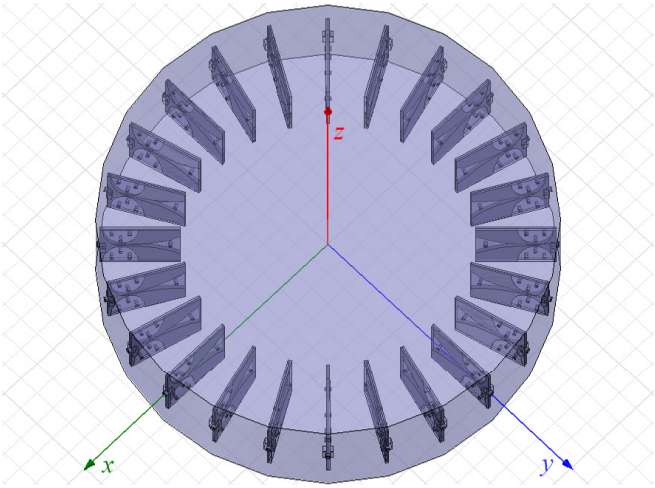

(b)

Figure 4.1: MWT system of twenty-four co-resident DLVAs. (a) Imaging domain $\mathcal{D}$ and measurement domain $\mathcal{S}$, (b) simulation geometry of the full 3D-model.

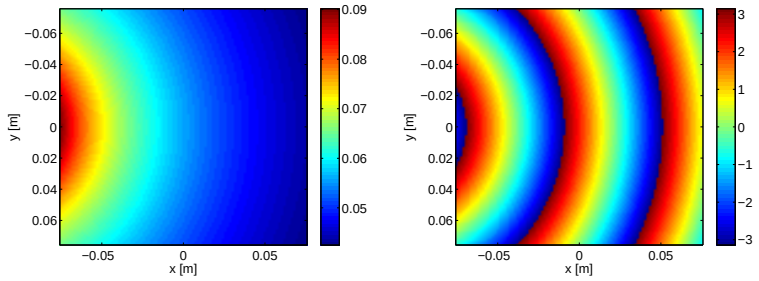

(a) Line-source $\left|E_{ls}^{inc}\right|$ (V/m) (b) Line-source $\angle E_{ls}^{inc}$ (Rad)

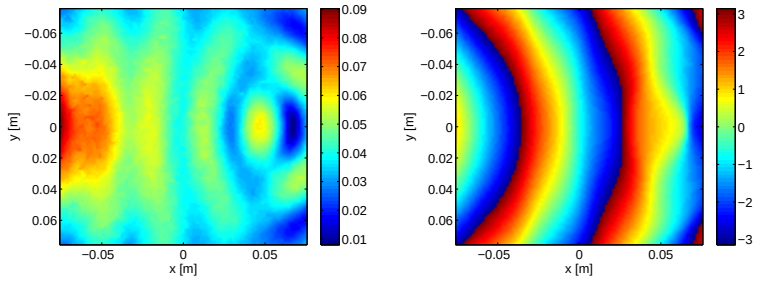

(c) 3D-model $\left|E_{3D}^{inc}\right|$ (V/m) (d) 3D-model $\angle E_{3D}^{inc}$ (Rad)

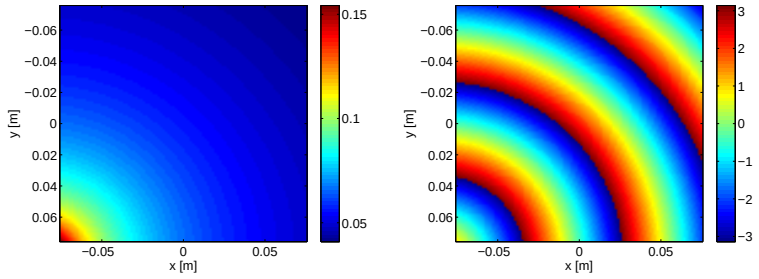

(e) Line-source $\left|E_{ls}^{inc}\right|$ (V/m) (f) Line-source $\angle E_{ls}^{inc}$ (Rad)

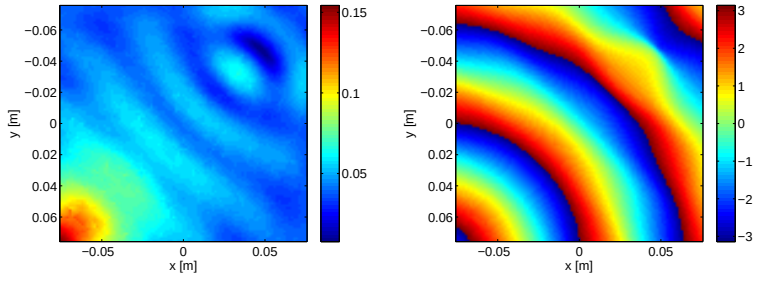

(g) 3D-model $\left|E_{3D}^{inc}\right|$ (V/m) (h) 3D-model $\angle E_{3D}^{inc}$ (Rad)

Figure 4.2: Incident field amplitude/phase in $\mathcal{D}$ at 5 GHz. (a)-(d) Antenna #1 and (e)-(h) antenna #4 is the Tx.

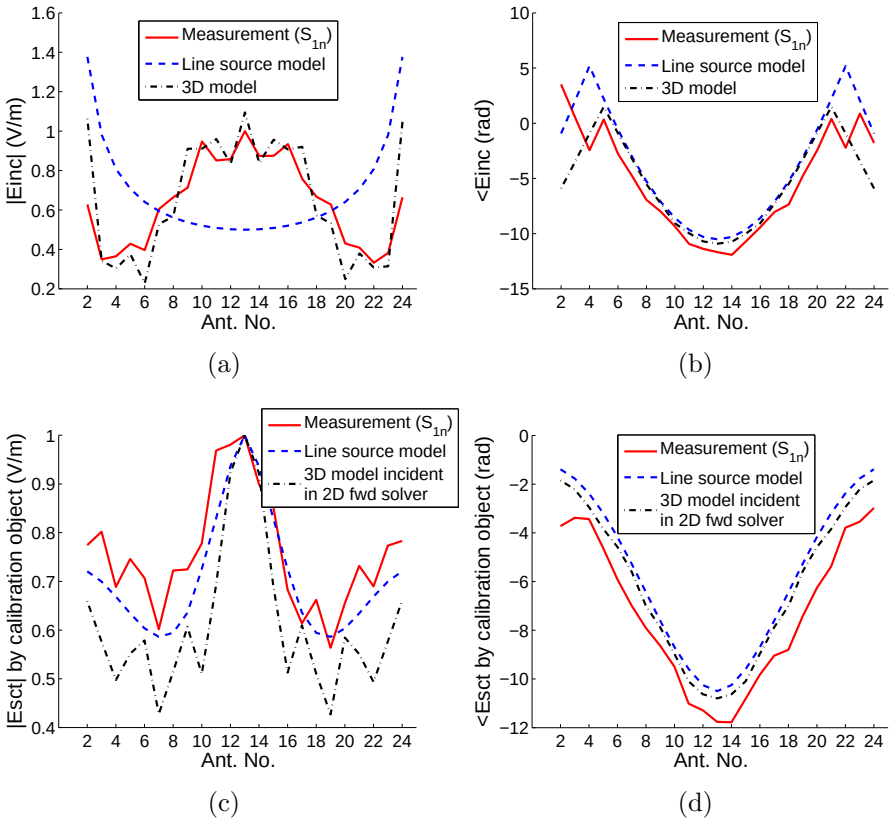

Figure 4.3: Comparison of the incident and the scattered fields (by PEC cylinder) on $\mathcal{S}$ at 5 GHz.

4.1.3 Calibration Coefficients

Let's denote the incident field calibration coefficients by ${\mathcal{C}_\mathcal{F}}^{inc}$. For each active transmitter, the ${\mathcal{C}_\mathcal{F}}^{inc}$ is calculated at the receiver points on $\mathcal{S}$ as

$$ {\mathcal{C}_\mathcal{F}}^{inc} = E^{inc}_{expected} / S^{inc}_{meas} \tag{4.2} $$

where S^{inc}_{meas} is the measured S-parameter, corresponding to the incident field, using a VNA, and $E^{inc}_{expected}$ is either from the 3D-model or from the line-source approximation. The corresponding calibration coefficient is denoted by $\mathcal{C}_{\mathcal{F}^{inc}_{3D}}$ or $\mathcal{C}_{\mathcal{F}^{inc}_{ls}}$, respectively.

In the scattered field calibration, for each active transmitter the calibration coefficient ${\mathcal{C}_\mathcal{F}}^{sct}$ is calculated at the receiver points on $\mathcal{S}$ as

$$ {\mathcal{C}_\mathcal{F}}^{sct} = E^{sct}_{expected} / S^{sct-PEC}_{meas} \tag{4.3} $$

where $S^{sct-PEC}_{meas}$ is the measured S-parameter, corresponding to the scattered field by the calibration object, and $E^{sct}_{expected}$ is either from the 3D-model or from the line-source approximation (as discussed in Section 4.1). The corresponding calibration coefficient is denoted by $\mathcal{C}_{\mathcal{F}^{sct}_{3D}}$ or $\mathcal{C}_{\mathcal{F}^{sct}_{ls}}$, respectively.

Note that we do not use a single calibration coefficient. For each transmitter-receiver pair, the calibration coefficients are calculated individually and are stored in a matrix $\underline{\mathcal{C}_\mathcal{F}}$. The measured scattered fields by an OI, $\underline{S^{sct}_{meas}}$, is then calibrated to $\underline{E^{sct}_{cal}} = \underline{\mathcal{C}_\mathcal{F}} \odot \underline{S^{sct}_{meas}}$, where $\odot$ denotes the Hadamard matrix product of the two matrices $\underline{\mathcal{C}_\mathcal{F}}$ and $\underline{S^{sct}_{meas}}$.

4.2 Inversion Results

Two dielectric phantom tests were utilized to test the different calibration techniques and the use of different incident fields on image reconstruction.

1. A complexity test: This test uses an object which is referred to as the e-phantom, shown in Figure 4.4 (a). The e-phantom is made of UltraHigh Molecular Weight polyethylene (UHMW) with relative complex permittivity of $\epsilon_r = 2.3 + j0.0$ [77]. The dimensions are shown in Figure 4.4 (b).

2. A resolution test: This test uses two nylon rods and a plastic pipe as shown in Figure 4.4 (c). The nylon rod complex permittivity is $\epsilon_r \approx 3.0 - j0.03$ [70]. We could not find a reliable information for the permittivity of the plastic pipe, however it was used so as to make the target more complicated.

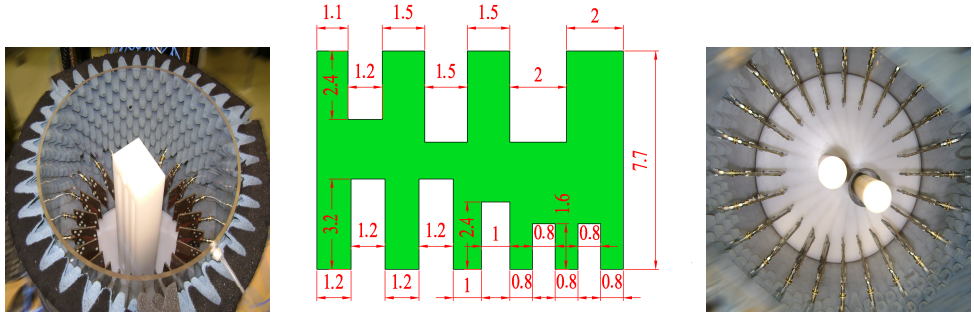

(a) (b) (c)

Figure 4.4: Phantoms utilized for image reconstruction. (a) The complexity test: e-phantom, (b) e-phantom dimensions (cm), and (c) the resolution test: plastic pipe (with diameters of $D_{inner} = 5.20$ cm , $D_{outer} = 5.80$ cm) and two nylon rods (with diameter of $D = 3.81$ cm).

The MR-GNI algorithm was utilized for image reconstruction with the data from the two antennas on either side of the transmitter antenna as well as the backscatterer removed. That is, the dataset consists of $24 \times 21 = 504$ measured points at 5 GHz.

For each OI, both the ${\mathcal{C}_\mathcal{F}}^{inc}$ (4.2) and ${\mathcal{C}_\mathcal{F}}^{sct}$ (4.3) were used to calibrate the dataset. The calibration coefficients are computed from both the line-source model and the 3D-model. Thus, four calibrated datasets are generated for each OI: $\mathcal{C}_{\mathcal{F}_{ls}}^{inc}$, $\mathcal{C}_{\mathcal{F}_{3D}}^{inc}$, $\mathcal{C}_{\mathcal{F}_{ls}}^{sct}$, and $\mathcal{C}_{\mathcal{F}_{3D}}^{sct}$. The corresponding incident field of each calibration coefficient is E_{ls}^{inc}, E_{3D}^{inc}, E_{ls}^{inc}, and E_{3D}^{inc}, respectively, which are the incident fields used in the domain of the inversion algorithm (see Table 4.1). Imaging results of the complexity test are depicted in Figure 4.5. Imaging results of the resolution test are depicted in Figure 4.6.

4.2.1 Quantitative Analysis of the e-phantom Inversion Results

For the complexity test, the mean and the standard deviation of permittivities of each image were calculated inside the e-phantom boundaries and inside the background medium. The e-phantom and the background boundaries are depicted in Figure 4.7. These calculations are illustrated in Figure 4.8 and provide us a criterion to quantitatively compare the four images. The real and the imaginary parts are calculated separately.

4.2.2 Discussion

In the MWT system, the fields are collected using a VNA that measures the scattering parameters S_{21} between its two ports. Thus, a trivial assumption is that the so called "antenna factors" for all the DLVAs, are the same. The antenna factor is defined as the ratio of the fields in front of a DLVA to a corresponding voltage at its terminal. In summary, in addition to this assumption, there exist different kinds of errors in this MWT system:

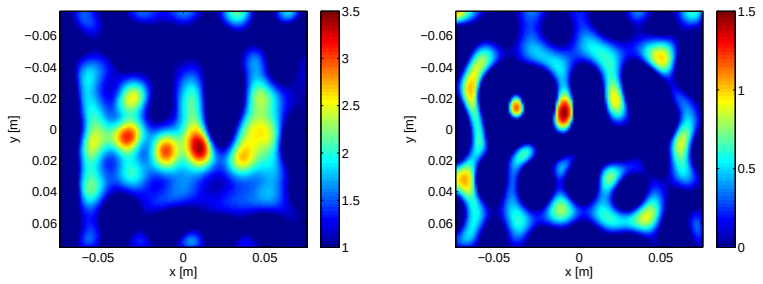

(a) Re(ϵ_r): $\mathcal{C}_{\mathcal{F}_{ls}}^{inc}, E_{ls}^{inc}$ (b) Im(ϵ_r): $\mathcal{C}_{\mathcal{F}_{ls}}^{inc}, E_{ls}^{inc}$

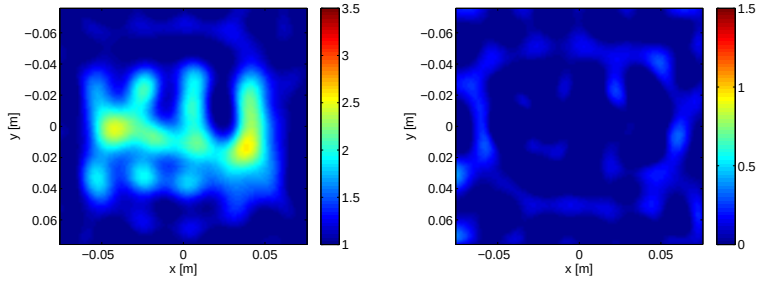

(c) Re(ϵ_r): $\mathcal{C}_{\mathcal{F}3D}^{inc}, E_{3D}^{inc}$ (d) Im(ϵ_r): $\mathcal{C}_{\mathcal{F}3D}^{inc}, E_{3D}^{inc}$

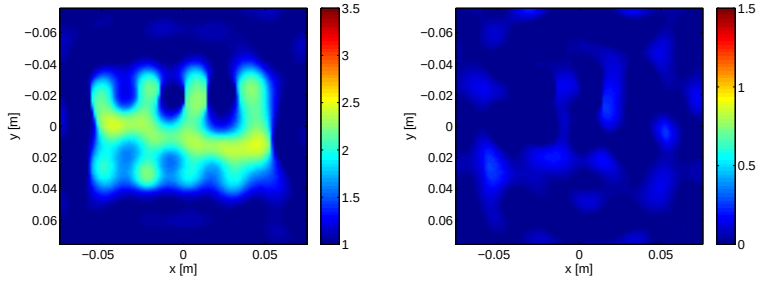

(e) Re(ϵ_r): $\mathcal{C}_{\mathcal{F}_{ls}}^{sct}, E_{ls}^{inc}$ (f) Im(ϵ_r): $\mathcal{C}_{\mathcal{F}_{ls}}^{sct}, E_{ls}^{inc}$

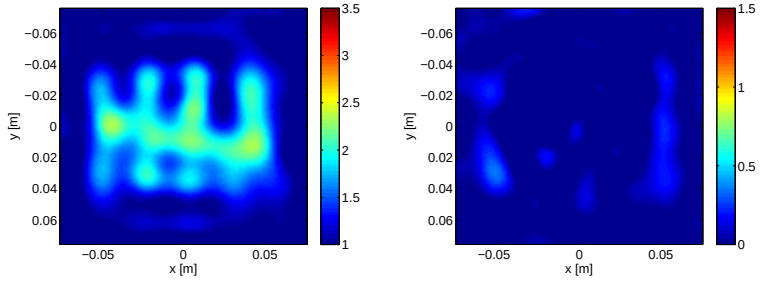

(g) Re(ϵ_r): $\mathcal{C}_{\mathcal{F}3D}^{sct}, E_{3D}^{inc}$ (h) Im(ϵ_r): $\mathcal{C}_{\mathcal{F}3D}^{sct}, E_{3D}^{inc}$

Figure 4.5: Complex permittivity reconstruction of the complexity test at 5 GHz using incident field calibration method $\mathcal{C}_{\mathcal{F}}{}^{inc}$, (a)-(d), and the scattered field calibration $\mathcal{C}_{\mathcal{F}}{}^{sct}$, (e)-(h).

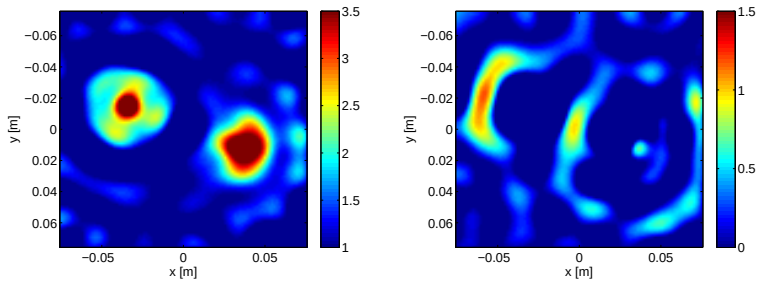

(a) Re(ϵ_r): $\mathcal{C}_{\mathcal{F}_{ls}}^{inc}, E_{ls}^{inc}$ (b) Im(ϵ_r): $\mathcal{C}_{\mathcal{F}_{ls}}^{inc}, E_{ls}^{inc}$

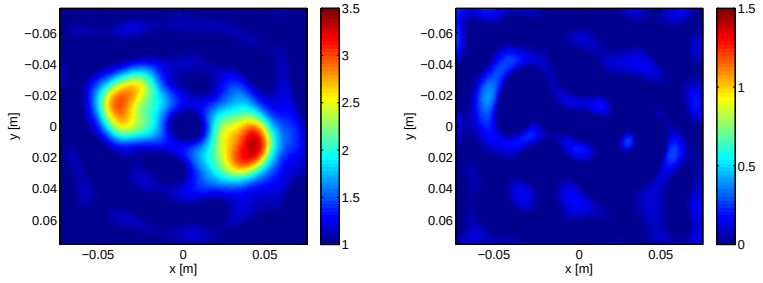

(c) Re(ϵ_r): $\mathcal{C}_{\mathcal{F}3D}^{inc}, E_{3D}^{inc}$ (d) Im(ϵ_r): $\mathcal{C}_{\mathcal{F}3D}^{inc}, E_{3D}^{inc}$

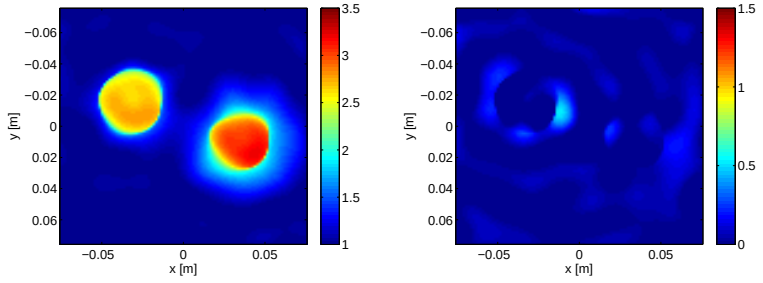

(e) Re(ϵ_r): $\mathcal{C}_{\mathcal{F}_{ls}}^{sct}, E_{ls}^{inc}$ (f) Im(ϵ_r): $\mathcal{C}_{\mathcal{F}_{ls}}^{sct}, E_{ls}^{inc}$

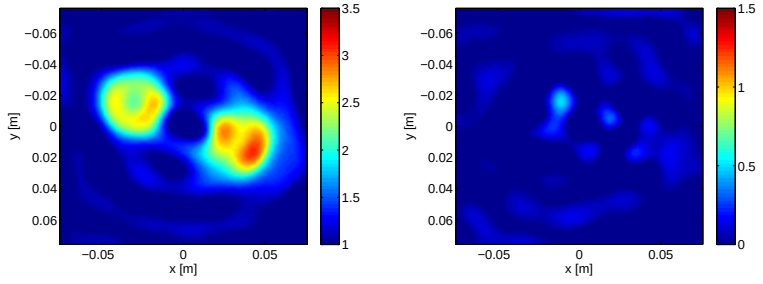

(g) Re(ϵ_r): $\mathcal{C}_{\mathcal{F}3D}^{sct}, E_{3D}^{inc}$ (h) Im(ϵ_r): $\mathcal{C}_{\mathcal{F}3D}^{sct}, E_{3D}^{inc}$

Figure 4.6: Complex permittivity reconstruction of the resolution test at 5 GHz using incident field calibration method: $\mathcal{C}_{\mathcal{F}}{}^{inc}$, (a)-(d), and the scattered field calibration $\mathcal{C}_{\mathcal{F}}{}^{sct}$, (e)-(h).

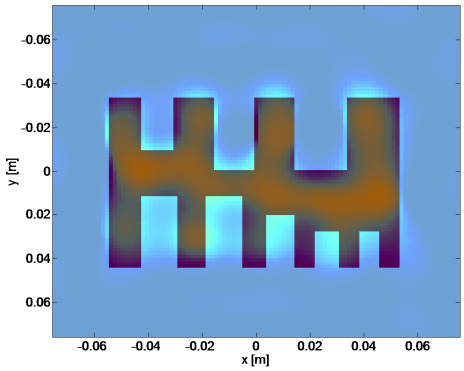

Figure 4.7: The e-phantom overlaid with a reconstructed image.

- The 2D MR-GNI algorithm which was used models neither the antennas nor the entire measurement system.
- Different polarizations contribute to the received voltage at each DLVA port and the antennas cannot measure a pure polarization, although the best antenna among the candidates was chosen.
- The 24 cables of the system experience different mechanical and bending stress. This stress introduces phase error within the cables which is variable and different for each antenna.
- The RF switch network consists of several mechanical switches. These switches can connect any input port i to any output port j. Each pair of i-j ports experiences a different RF route. Different routings of the ports, introduces a phase error in S_{ji} measurements.

Due to the use of the scattered field in the algorithm by subtracting the total and incident fields, the third and fourth sources of error vanish. A method to reduce the second source of error is introduced in the next chapter. For the first source of error is to be removed using the calibration coefficients.

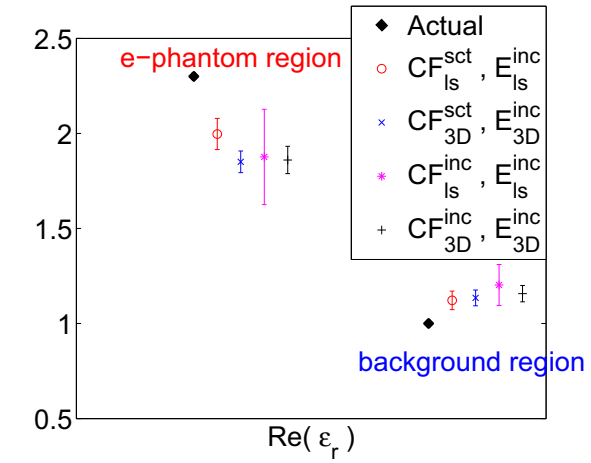

(a) Re(ϵ_r)

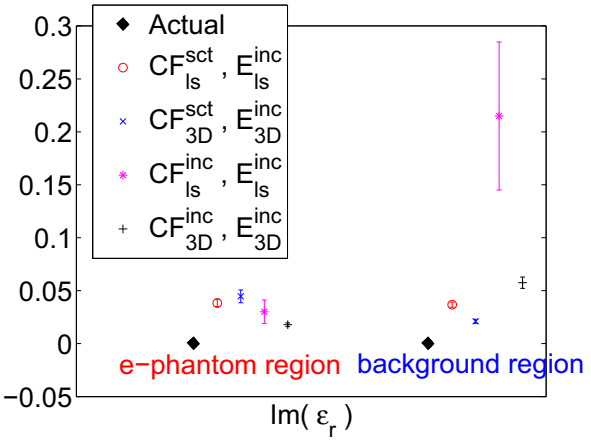

(b) -Im(ϵ_r)

Figure 4.8: The mean and standard deviation of reconstructed images.

In addition to these sources of error, the incident field modeling is also very important as it appears directly in the cost function of MWT algorithms (2.26) or (2.30).

Quantitatively studying the results in Figures 4.5 and 4.6, one can find that using $(\mathcal{C}_{\mathcal{F}_{ls}}^{inc}, E_{ls}^{inc})$ generates considerable artifacts especially in the imaginary part of the image while its real part is not quantitatively accurate. This is due to the significant error between the line-source model and the real system, see Figure 4.3 (a),(b).

$(\mathcal{C}_{\mathcal{F}_{3D}}^{inc}, E_{3D}^{inc})$ and $(\mathcal{C}_{\mathcal{F}_{3D}}^{sct}, E_{3D}^{inc})$ generate relatively accurate quantitative images. For these results, E_{3D}^{inc} is extracted from the 3D-model, here however it is combined with a 2D imaging algorithm. It is speculated this is the main reason for not seeing a considerable improved image.

Finally $(\mathcal{C}_{\mathcal{F}_{ls}}^{sct}, E_{ls}^{inc})$ generates, relatively, the best qualitative results. The line-source incident field does not match with the real system however there is a good match between the scattered fields by the PEC object, see Figure 4.3 (c),(d).

The quantitative results of Figure 4.8 also agree with above observations. $(\mathcal{C}_{\mathcal{F}_{ls}}^{inc}, E_{ls}^{inc})$ generate a lot of artifacts especially in the imaginary part of the image while the real part is not quantitatively accurate. The maximum variance is observed for this case. However by the use of a more accurate incident field such as the one obtained from the 3D-model, the variance and the mean improves significantly, compare the mean and the variance of $(\mathcal{C}_{\mathcal{F}_{3D}}^{inc}, E_{3D}^{inc})$ with $(\mathcal{C}_{\mathcal{F}_{ls}}^{inc}, E_{ls}^{inc})$. $(\mathcal{C}_{\mathcal{F}_{3D}}^{inc}, E_{3D}^{inc})$ and $(\mathcal{C}_{\mathcal{F}_{3D}}^{sct}, E_{3D}^{inc})$ both use E_{3D}^{inc} and generate relatively similar and accurate quantitative images, with similar variance and mean. $(\mathcal{C}_{\mathcal{F}_{ls}}^{sct}, E_{ls}^{inc})$ generates, relatively, the best result with the closest mean value to the actual value, in the real part of the image.

4.3 Conclusion

The MWT system without any OI was fully simulated, to obtain an accurate incident field inside the imaging domain. Then either the line source approximation or the incident field from the full 3D-model were employed to calculate calibration coefficients to calibrate the measured data, listed in Table 4.1. This task was performed for both the incident field and the scattered field calibration techniques. The image reconstruction of the two calibration procedures was presented for a complexity test object and for a resolution test object.

In the UM loss-less air-based imaging system, accurate incident field modeling can improve the images especially when using ${\mathcal{C}_{\mathcal{F}}}^{inc}$. It is speculated that the ${\mathcal{C}_{\mathcal{F}}}^{sct}$ generates more accurate quantitative images due to the contribution of the forward solver in ${\mathcal{C}_{\mathcal{F}}}^{sct}$ calculation. It is also speculated that the 3D-model would improve the imaging result if used with a 3D algorithm.

Chapter 5

Near-Field Measurement and Indirect Microwave Imaging Systems

MWT algorithms assume a numerical model for the data collected experimentally. In the experimental system only circuit quantities can be directly measured, however most inversion algorithms require field values at appropriate spatial locations/regions with a particular polarization (see Chapter 1). Thus, a measurement error occurs in the collected dataset of these *direct* MWT systems including the system discussed in Chapter 3. On the other hand, near-field measurement techniques are capable of collecting a particular field polarization. Unfortunately these techniques were mostly developed for antenna radiation pattern measurements and are not suitable for MWT applications, however there are some near-field measurement techniques such as the Modulated Scatterer Technique (MST) which can be modified and implemented for MWT.

In this chapter a brief review of the near-field measurement techniques including the ones for antenna radiation measurements is given. The theory of MST is then discussed, including the theory of a proposed MWT system based on the MST. The implementation and performance of the proposed system is discussed in the next chapter in greater detail.

5.1 Field Regions of a DLVA

In antenna theory, the term "near-field" generally refers to a region whose energy is imaginary or *stored* ([52] page 156). In this region, all field polarizations exist and $kr << 1$ where $k^2 = \omega^2\mu\epsilon$ is the complex wave number and r is the distance from the antenna. The "far-field" region refers to a region which contains only real energy, here $kr >> 1$. In the far-field region, the field polarization parallel to the radial direction from the antenna vanishes and the wave is polarized transverse to this direction. The region between the near-field and the far-field is referred to as the intermediate region.

A more detailed description of the near-field and the far-field regions is provided in [78]. The regions surrounding an antenna can be partitioned into *reactive near-field*, *radiating near-field*, *Fresnel*, and *Fraunhofer* regions. These regions are depicted in Figure 5.1 for a DLVA. In this figure D refers to the maximum dimension of the antenna, here 7.0 cm. Measurements indicate that the reactive near-field region starts from the surface of the antenna up to a distance of one wavelength, λ, from the surface. Inside this region the phase difference between the magnetic and electric field vectors is 90° and the power is imaginary. The quadrature phase difference of the field vectors does not necessarily happen beyond λ, thus this region is called the radiating near-field region. In the radiating near-field region the fields tend to be in-phase but they do not exhibit a e^{-jkr}/r relation. The term Fresnel region is a subregion of the radiating near-field region in which a phase variation of (e^{-jkr}) can be used. This region extends from $(\frac{D}{2\lambda})^{(\frac{1}{3})}\frac{D}{2} + \lambda$ to the far field. Finally the term Fraunhofer is synonymous to far-field and is taken from optic theory and refers to a region where a focal point of an antenna (phase center) can be calculated. The added λ in Figure 5.1 is to cover the cases of antennas with D smaller than λ [78].

Different field regions of the DLVA are calculated for frequencies of 3 GHz to 6 GHz with steps of 1 GHz. The calculations are shown in Table 5.1. Note that these calculations are for the case of a single antenna in free-space without the presence of the other DLVAs or the OI. With regard to Figure 4.1 (a) of the UM direct MWT system, if one assumes that the imaging domain $\mathcal{D}$ is a centered square of 12.5 cm, the minimum distances of the DLVAs from $\mathcal{D}$ is in the range of 3.7 cm to 6.7 cm and the minimum separation of co-resident DLVAs is 3.1 cm. Thus, it is clear that in the air-based direct system, the antennas and the imaging domain are in the near-field region.

Other reported co-resident MWT systems, utilize a lossy background medium which results in a far-field system, so that the co-resident antennas remain *invisible* to each other, *e.g.* see [6], [48] and [72]. Due to the positioning of the DLVAs in the near-field region, the UM systems are referred to as near-field tomography systems.

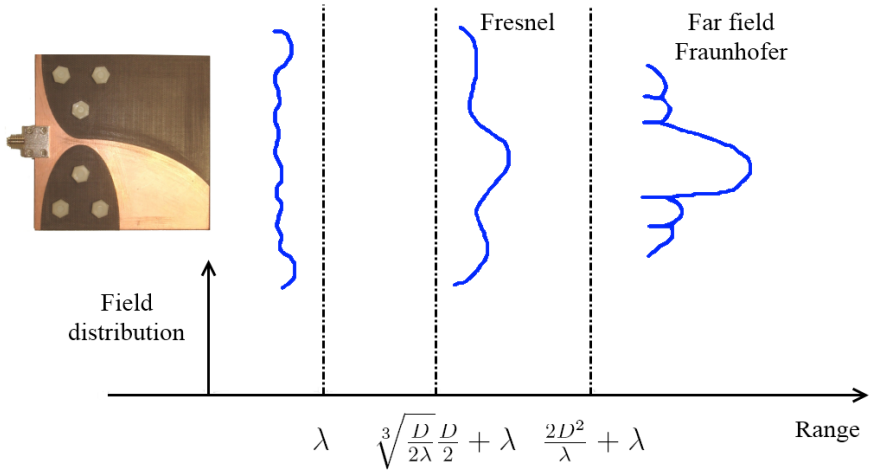

Figure 5.1: Radiation field regions of an antenna, see [78].

Table 5.1: Radiating regions of a single DLVA in free-space. Distances are in cm.

Frequency (GHz)	Radiating near-field	Fresnel	Fraunhofer
3.0	10.0	12.5	19.8
4.0	7.5	10.2	20.6
5.0	6.0	8.9	22.3
6.0	5.0	8.1	24.6

5.2 Near-Field Measurement Techniques

Near-field measurements can be used to calculate an antenna radiation pattern. There are a number of reasons for the interests in antenna pattern measurement using near-field techniques [78]:

- Radiation properties of special antennas: Some antennas are not easily measured using a traditional low-cost far-field region technique. In some cases the antenna's far-field distance is larger than the size of a typical anechoic chamber. In other cases the antenna is very heavy and it's not possible to mount it on the chamber's tower. It is also possible that the electrical dimension of the antenna is very large. Sometimes the far-field pattern is very complicated and due to the limitations of the far-field chamber, standard measurement procedures cannot measure their radiation characteristics, and finally some antennas are not reciprocal and it is not possible to measure their radiation pattern using conventional far-field techniques.

- Radiation properties of antennas under operating conditions: In many applications antenna performance is measured in an idealized condition of an anechoic chamber. When the antenna is mounted on a system, the surrounding medium affects its performance, *e.g.* the weather conditions, the presence of ground or neighboring buildings, and the electronic instruments attached to the antenna.

For these applications the antenna measurement should be performed using near-field methods.

5.2.1 Conventional Technique with Cables

Conventional near-field probes are connected to a measurement instrument using a high quality cable. These probes are usually employed in near-field antenna measurements. They scan the near field of the antenna under test in a rectangular, cylindrical or spherical pattern with different polarizations. The measured field is then transformed into the far-field using closed-form expressions. A historical review of using the conventional near-field technique is available in [78] that covers the period between the '50s to the '80s.

5.2.2 Perturbation Technique for Measuring Field

The conventional method of near-field measurement has a number of disadvantages:

- The probe needs an RF cable to transfer the signal into a measurement instrument such as a network analyzer. The presence of the cable in the measurement region disturbs the field which results in measurement error.
- To measure the field at different locations one needs to move the probe as well as its cable. The probe movement introduces a stress on the cable that results in phase error.
- Conventional near-field methods require accurate and complicated mechanical systems. In addition to the higher costs of such a system, the measurement time is slow especially in cases that many sampling points are needed.

An alternative to the conventional method is called the perturbation method, initially introduced in 1955 [79]. The perturbation method is based on measuring the scattered field of a known scatterer. To measure the field at a specific location, a probe with known scattering behavior is placed at that location. Due to the presence of the probe, a current is induced on the probe which in turn generates a scattered field that perturbs the original field. To measure the field by this method an antenna is required to record the unperturbed and the perturbed fields. This antenna is called the *collector*.

In the mono-static perturbation method proposed by Justice and Rumsey [79], the collector antenna is initially matched while the probe is absent. Once the probe is introduced an associated voltage, which depends on the amount of perturbation, is generated at the antenna terminals. The voltage is proportional to the square of the original unperturbed field value at the probe location. The block diagram of this measurement is shown in Figure 5.2. A hybrid module is used to distinguish the transmitted and the reflected signals. When the probe is absent, the hybrid is tuned such that the detected voltage remains close to zero. The presence of probe is detected by the amount of voltage at the collector port.

5.2.3 Modulated Scatterer Technique

In principle, the perturbation method can be used to measure the electromagnetic field with the probe located at any distance from the collector, however in practice as the distance from the probe to the collector increases the sensitivity of the measurement decreases. This is due to the small amount of scattered field from the probe. In such cases, it is not feasible to detect the perturbed field [80]. A solution to increase the sensitivity is to modulate the probe based on the MST. The modulation scheme

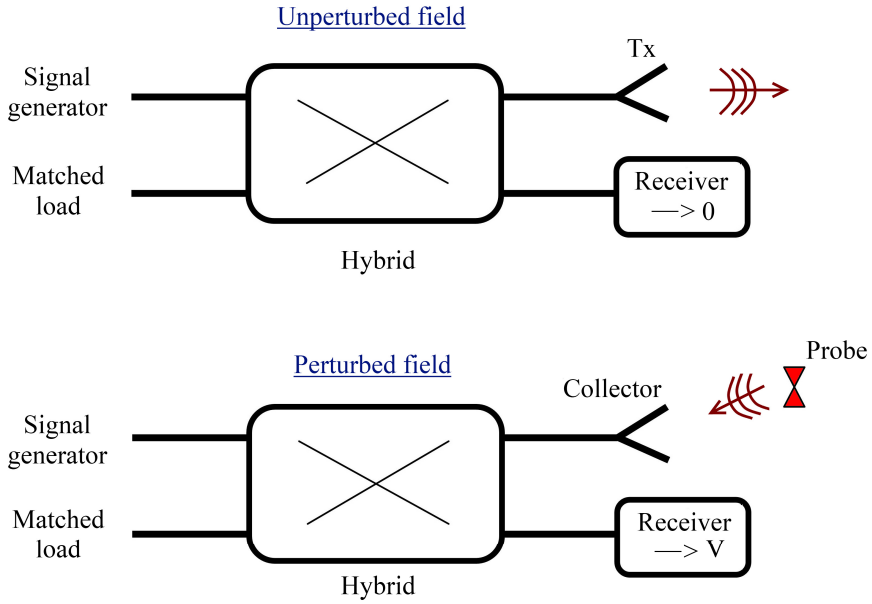

Figure 5.2: General block diagram of near-field perturbation technique for monostatic measurement [79].

can be implemented electronically [81], optically [82], or mechanically [80]. Since the probe is modulated by a known signal, noise and interference can be rejected at the receiver/collector. Electrical modulation was the first modulation to be used, introduced in 1955 [83]. In the same year a technique for mechanical modulation was successfully implemented [80].

A schematic showing the different modulations is shown in Figure 5.3. In this figure, "ordinary probe" represents the perturbation method which is usually implemented using a piece of thin metallic wire without any modulation, where the probe is present/absent at the measurement location to perturb/unperturb the fields, respectively. "Mechanical modulation" is implemented by mounting a metallic thin wire probe on a supporting rod. Then the probe is spun at a known angular frequency so that the measurement is modulated at that frequency. In "optical modulation" the probe is loaded with an optically sensitive element. The element is then acti-

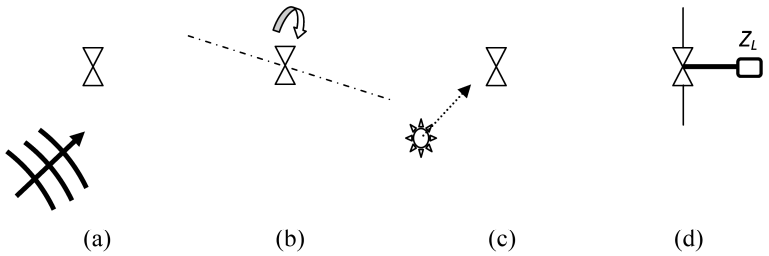

Figure 5.3: Illustration of different modulations for probe: (a) ordinary probe, (b) mechanical modulation, (c) optical modulation, (d) electrical modulation.

vated/deactivated by a light source. By changing the frequency of light illumination the probe is modulated accordingly. One can use an optical fiber to transmit light power to the probe [82]. The "electrical modulation" scheme is implemented by connecting a load to the probe where the electrical characteristics of the load are changed at a known frequency to modulate the probe.

Of particular interest, the electrical modulation is usually the economical choice of modulation as it neither requires the complicated mechanical spinning systems of mechanical modulation nor the relatively expensive optical modules required for optical modulation.

Applicable to the electrical modulation case, Harrington [81] has developed equations for the backscattering of a dipole loaded at the center by different loads, Z_l. Figure 5.4 shows his results of the normalized back scattering of a piece of wire (dipole), at different frequencies. σ in this figure is the echo area of the scatterer. There are four graphs in this figure corresponding to (a): $Z_l = 0$ or the short-circuit load, (b): $Z_l = -j\mathrm{Im}(Z^{(f)}_{dipole})$ or the resonance load which is continuously changing as a function of frequency, (c): $Z_l = -j\mathrm{Im}(Z_{dipole})$ when the dipole dimensions and the load remain unchanged, and (d): $Z_l = \infty$ or the open-circuit load. Note that case (b) is not a practical case, however it shows the maximum amount of back-scattering

at the different frequencies. As shown in this figure, case (d) is an open-circuit probe that does not perturb the field significantly and its amplitude is very low in a wide frequency range. The echo of the "open-circuit" and "short-circuit" loaded dipoles are significantly different, especially at the resonance frequencies where the effective length of the wire is close to the half wave-length.

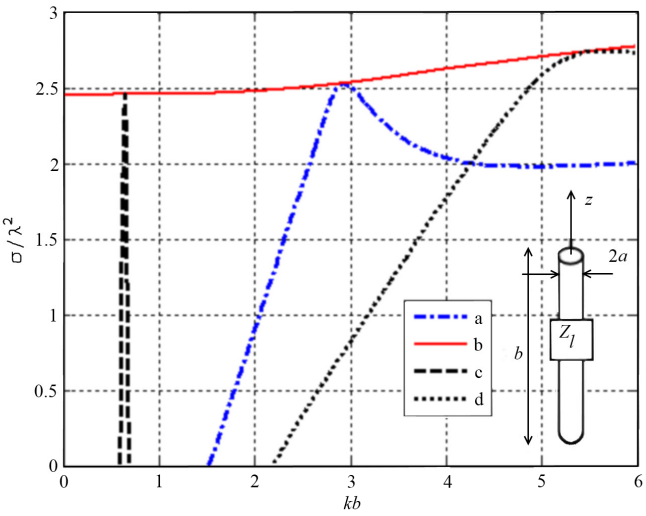

Figure 5.4: Normalized echo area from (a) Short circuit dipole, (b) Resonant dipole, (c) Dipole resonated by fixed L, and (d) Open-circuited dipole, b/a = 150 [81].

The results of Figure 5.4 show that one can change/modulate a probe's load, Z_l, in order to change the scattered field by the probe. Since this scattered field is proportional to the induced current on the probe as well as the field at the probe's location, it is possible to find the field at the probe's location by changing/modulating the impedance Z_l. The MST can be utilized for a variety of applications such as field probing applications, *e.g.* field distribution of a microstrip TL at different locations [82], non-destructive testing of industrial applications [4], and microwave imaging. Using this technique, one of the earliest MI systems was implemented in the '70s [26].

In current MST systems in existence, the probe is modulated using a low-frequency signal and a coherent detector is utilized to extract the field at the probe's location. If the collector and the Tx antenna are the same, the system is called mono-static MST and if the collector and the Tx are separated, the system is called bi-static MST. The general configuration of mono-static and bi-static MST using a coherent detector is shown in Figure 5.5 (a) and (b), respectively. It can be shown that the modulated signal is proportional to the field squared value and to the field value in the mono-static case and the bi-static case, respectively, at the probe's location [84,85].

5.3 Theory of Scatterer Probe Technique to be Utilized for MWT

In Chapter 1, the two major approaches to MWT measurement systems: the *direct* and the *indirect* approaches were briefly introduced. These two are depicted in Figure 5.6 (a) and (b), respectively. The direct systems were discussed in Chapter 3, including the UM air-based system.

The indirect MWT systems utilize the MST technique. A general configuration of these systems is depicted in Figure 5.6 (b). A Tx antenna illuminates the OI in the presence of a number of *probes*. The probes are positioned at some distance from a Rx antenna, the *collector*. The collector's task is to infer the field present at each probe's location. In these systems the process of field measurement is implemented by the use of the MST as described in Section 5.2.3.

In the proposed near-field system which will be discussed in the next chapter, no coherent detector is utilized. Instead, a VNA and an RF switch network were used for measurement which are connected to the DLVAs. In this section, the theoretical

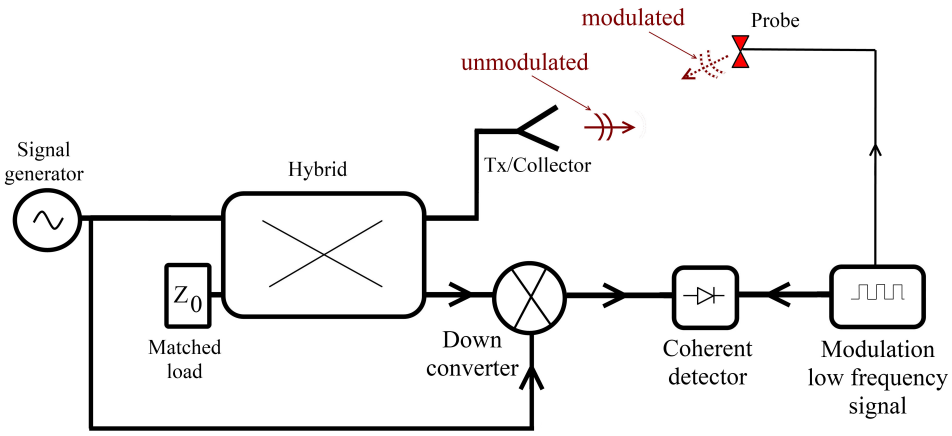

(a)

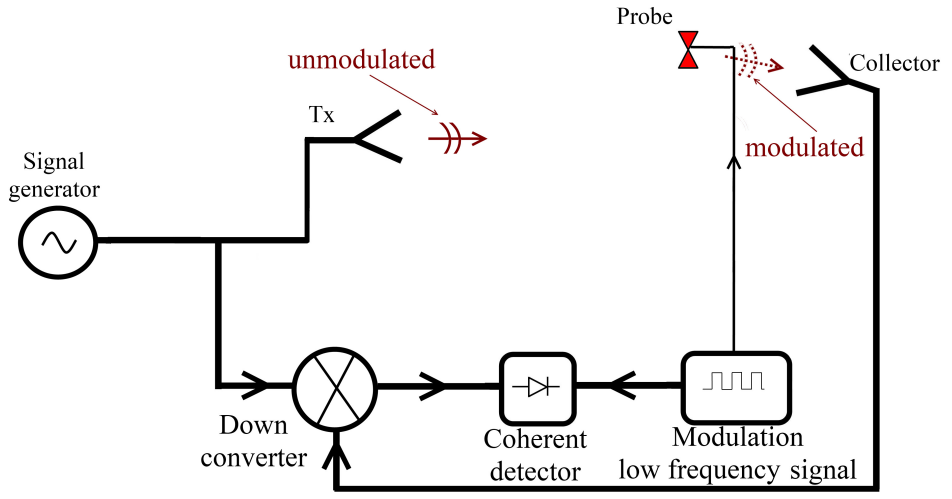

(b)

Figure 5.5: MST general block diagram using coherent detector: (a) mono-static, (b) bi-static.

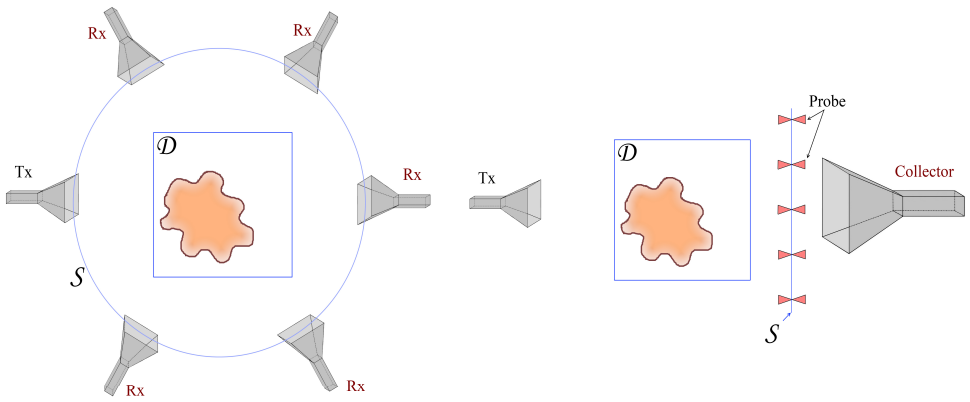

(a) Direct MWT system (b) Indirect MWT system

Figure 5.6: General configuration of conventional MWT systems.

background of this system is discussed. As in the coherent systems, it can be implemented either as mono-static or bi-static systems. A schematic of a mono-static measurement set-up using a single DLVA is depicted in Figure 5.7.

5.3.1 Near-Field of a Dipole

In this section the relationship between the fields around and the induced current on a dipole is considered.

When a thin wire is exposed to an electromagnetic field, a current is induced on the wire such that the generated field by the induced current cancels the tangential electric field along the wire. This is because the total electric field, the summation of the incident and the scattered fields, should vanish on the wire. The geometry of the wire is shown in Figure 5.8 (a). Let's assume that the field around the wire does not change rapidly and that the induced current can be approximated as

$$I = \begin{cases} I_m \sin k(L-z) & , \quad z > 0 \\ I_m \sin k(L+z) & , \quad z < 0 \end{cases} \tag{5.1}$$

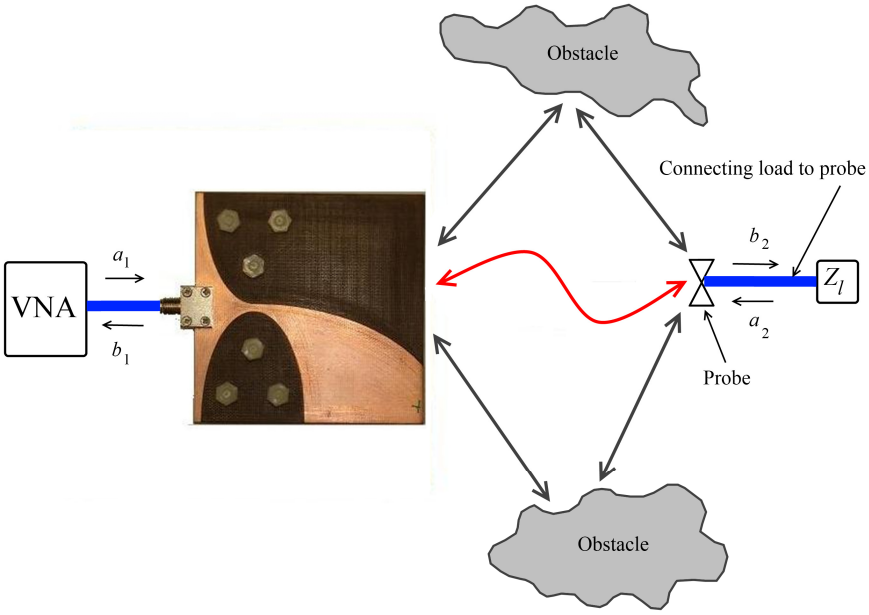

Figure 5.7: Probe present in front of a DLVA with obstacles in the local environment.

where I_m is the maximum current and L is the half-length of the wire.

With the position variables, referring to Figure 5.8, defined as

$$r = \sqrt{(z-l)^2 + y^2} \quad r_1 = \sqrt{(z-L)^2 + y^2} \quad r_2 = \sqrt{(z+L)^2 + y^2} \quad r_0 = \sqrt{z^2 + y^2} \tag{5.2}$$

where the geometry is depicted in $yz-$ plane (it is symmetrical with respect to the $z-$ axis), an expression for the vector potential at an arbitrary point P is given as [86]

$$A_z = \frac{\mu}{4\pi} \int \frac{I_z e^{-jkr}}{r} dl = \frac{\mu I_m}{4\pi} \left[\int_0^L \frac{\sin k(L-l) e^{-jkr}}{r} dl \right] \tag{5.3}$$

As shown in [86], the electric and magnetic fields in the $yz-$ plane can be obtained

from (5.3) as

$$E_z = -j30I_m\left(\frac{e^{-jkr_1}}{r_1}+\frac{e^{-jkr_2}}{r_2}-2\cos kL\frac{e^{-jkr_0}}{r_0}\right) \tag{5.4}$$

$$E_y = j30I_m\left(\frac{z-L}{y}\,\frac{e^{-jkr_1}}{r_1}+\frac{z+L}{y}\,\frac{e^{-jkr_2}}{r_2}-\frac{2z\cos kL}{y}\,\frac{e^{-jkr_0}}{r_0}\right) \tag{5.5}$$

$$H_\phi = \frac{j30I_m}{\eta y}\left(e^{-jkr_1}+e^{-jkr_2}-2\cos kLe^{-jkr_0}\right) \tag{5.6}$$

Since the total field must vanishe on the wire, a current is induced on the wire to cancel the incident field. Thus, the scattered field on the surface of the wire, $y = a$, follows the relation of

$$E_z^s(x=0,y=a,z) = -E_z^i = -j30I_m\left(\frac{e^{-jkr_1}}{r_1}+\frac{e^{-jkr_2}}{r_2}-2\cos kL\frac{e^{-jkr_0}}{r_0}\right) \tag{5.7}$$

and one can see that the magnitude of the induced current, I_m, has a linear relationship to the field. Now suppose that there are two wires parallel to the z- axis, separated by a small gap, as shown in Figure 5.8 (b). By assuming that the resulting total field at the two wires' location is symmetric then the induced current on both wires should be the same. Each wire interacts with the field and they generate a "perturbed" or scattered transverse field, E_y, in the gap. The transverse field can be calculated from (5.5) by shifting the coordinate system to $z = +L$ for wire $_1$ and to $z = -L$ for the wire $_2$. One can see that the transverse fields cancel each other in the gap, thus the dipole wires do not perturb the transverse polarized field in the gap and they only interact with the E_z. This is one of the advantages of scatterer probe technique where only a single polarization of the field is perturbed.

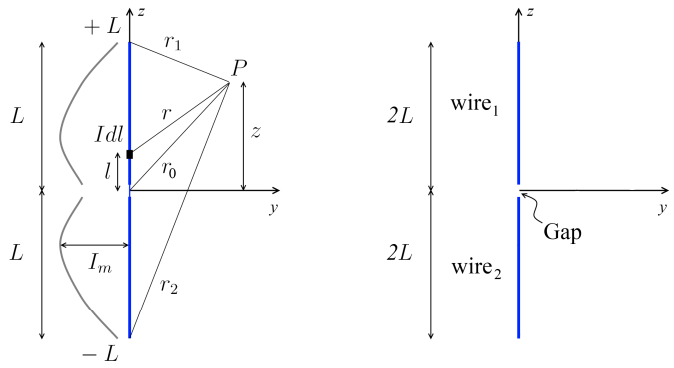

Figure 5.8: Wire (dipole) in a field, (a) geometry of single wire, (b) two wires with a gap at the center.

5.3.2 Antenna-Probe Reciprocity

Let's assume that a DLVA antenna and a wire-probe are located in free-space, see Figure 5.9. Using the reciprocity theorem, one is able to derive a relation between the received scalar power of the DLVA and the longitudinal field component at the probe's location.

The reciprocity theorem states that: "response of a system to a source is unchanged when source and measurer are interchanged" ([36] page 116). In circuit theory this is stated as "the voltage at b due to a current source at a is equal to the voltage at a due to the same current source at b" for a network consisting of port a and port b ([36] page 119). In Figure 5.9 one may consider the DLVA and the probe as the two ports of a network similar to the analysis performed for horn antennas in [87].

Let's assume two cases: (1) the DLVA is excited at its coaxial entry port while the probe is just a receiver, and (2) the probe is excited at its port and the DLVA is

just a receiver. Maxwell's curl equations for each case are written as

$$\begin{cases} \nabla \times \mathbf{E}^{(1)} &= -j\omega\mu\mathbf{H}^{(1)} \\ \nabla \times \mathbf{H}^{(1)} &= j\omega\epsilon\mathbf{E}^{(1)} + \mathbf{J}^{(1)} \end{cases}, \quad \begin{cases} \nabla \times \mathbf{E}^{(2)} &= -j\omega\mu\mathbf{H}^{(2)} \\ \nabla \times \mathbf{H}^{(2)} &= j\omega\epsilon\mathbf{E}^{(2)} + \mathbf{J}^{(2)} \end{cases} \tag{5.8}$$

where $\mathbf{J}^{(1)}$ is the current imposed at the DLVA port in "case (1)" and $\mathbf{J}^{(2)}$ is the current imposed on the probe port in "case (2)". Applying the vector identity $\nabla \cdot (\mathbf{A} \times \mathbf{B}) \equiv (\nabla \times \mathbf{A}) \cdot \mathbf{B} - (\nabla \times \mathbf{B}) \cdot \mathbf{A}$, one can write

$$\begin{aligned} &\nabla \cdot (\mathbf{E}^{(1)} \times \mathbf{H}^{(2)} - \mathbf{E}^{(2)} \times \mathbf{H}^{(1)}) \equiv \\ &\left[(\nabla \times \mathbf{E}^{(1)}) \cdot \mathbf{H}^{(2)} - (\nabla \times \mathbf{H}^{(2)}) \cdot \mathbf{E}^{(1)}\right] - \left[(\nabla \times \mathbf{E}^{(2)}) \cdot \mathbf{H}^{(1)} - (\nabla \times \mathbf{H}^{(1)}) \cdot \mathbf{E}^{(2)}\right] = \\ &\left[(-j\omega\mu\mathbf{H}^{(1)}) \cdot \mathbf{H}^{(2)} - (j\omega\epsilon\mathbf{E}^{(2)} + \mathbf{J}^{(2)}) \cdot \mathbf{E}^{(1)}\right] - \\ &\left[(-j\omega\mu\mathbf{H}^{(2)}) \cdot \mathbf{H}^{(1)} - (j\omega\epsilon\mathbf{E}^{(1)} + \mathbf{J}^{(1)}) \cdot \mathbf{E}^{(2)}\right] \end{aligned}$$

which, because it is assumed that the material variables in problems (1) and (2) are the same, can be simplified to

$$\nabla \cdot (\mathbf{E}^{(1)} \times \mathbf{H}^{(2)} - \mathbf{E}^{(2)} \times \mathbf{H}^{(1)}) = -\mathbf{J}^{(2)} \cdot \mathbf{E}^{(1)} + \mathbf{J}^{(1)} \cdot \mathbf{E}^{(2)} \tag{5.9}$$

Equation (5.9) is another representation of reciprocity theorem. Note that an alternative for using imposed currents, $\mathbf{J}^{(1)}$ and $\mathbf{J}^{(2)}$, is the use of excitation fields at the ports' apertures [87]. Thus, it is assumed that there isn't any imposed current distribution and $\mathbf{J}^{(1)} = \mathbf{J}^{(2)} = 0$.

Applying the Divergence theorem

$$\int_S (\mathbf{E}^{(1)} \times \mathbf{H}^{(2)} - \mathbf{E}^{(2)} \times \mathbf{H}^{(1)}) \cdot \hat{\mathbf{n}} ds = 0 \tag{5.10}$$

Referring to Figure 5.9, the integration of (5.10) over surface "S" can be divided into four surfaces: the antenna surface (S_A), the probe surface (S_p), the infinite enclosure (S_∞), and the feed port reference planes (S_f). The surface S_∞ is in the far-field and therefore the fields for both cases are orthogonal to the outward normal vector, $\hat{\mathbf{n}}$

$$\mathbf{E}^{(1)} \cdot \hat{\mathbf{n}} = \mathbf{H}^{(1)} \cdot \hat{\mathbf{n}} = \mathbf{E}^{(2)} \cdot \hat{\mathbf{n}} = \mathbf{H}^{(2)} \cdot \hat{\mathbf{n}} = 0 \tag{5.11}$$

Because $\mathbf{B} \times \mathbf{C} \cdot \mathbf{A} \equiv \mathbf{A} \times \mathbf{B} \cdot \mathbf{C}$, the contribution of the surface integral in (5.10) can be written as

$$\int_{S_\infty} (\mathbf{E}^{(1)} \times \mathbf{H}^{(2)} - \mathbf{E}^{(2)} \times \mathbf{H}^{(1)}) \cdot \hat{\mathbf{n}} ds = \int_{S_\infty} (\hat{\mathbf{n}} \times \mathbf{E}^{(1)} \cdot \mathbf{H}^{(2)} - \hat{\mathbf{n}} \times \mathbf{E}^{(2)} \cdot \mathbf{H}^{(1)}) ds \tag{5.12}$$

but $\mathbf{H}^{(1)} = \hat{\mathbf{n}} \times \mathbf{E}^{(1)}/\eta$ and $\mathbf{H}^{(2)} = \hat{\mathbf{n}} \times \mathbf{E}^{(2)}/\eta$, where η is the medium wave impedance, and therefore this integral is zero, that is

$$\int_{S_\infty} (\mathbf{E}^{(1)} \times \mathbf{H}^{(2)} - \mathbf{E}^{(2)} \times \mathbf{H}^{(1)}) \cdot \hat{\mathbf{n}} ds = 0 \tag{5.13}$$

The surfaces S_A and S_p are PEC therefore $\mathbf{E}^{(1)} \times \hat{\mathbf{n}} = 0$ and

$$\int_{S_A+S_p} (\mathbf{E}^{(1)} \times \mathbf{H}^{(2)} - \mathbf{E}^{(2)} \times \mathbf{H}^{(1)}) \cdot \hat{\mathbf{n}} ds = \int_{S_A+S_p} (\mathbf{H}^{(2)} \cdot (\mathbf{E}^{(1)} \times \hat{\mathbf{n}}) - \mathbf{H}^{(1)} \cdot (\mathbf{E}^{(2)} \times \hat{\mathbf{n}})) ds = 0 \tag{5.14}$$

Thus, the only contribution in (5.10) from the surface integral is from the feed reference planes S_f. Since it is assumed that the imposed currents are zero and the feed ports are excited by the fields, equation (5.10) is summarized as

$$\int_{S_{f,DLVA} \cup S_{f,probe}} \mathbf{E}^{(1)} \times \mathbf{H}^{(2)} \cdot \hat{\mathbf{n}} ds = \int_{S_{f,DLVA} \cup S_{f,probe}} \mathbf{E}^{(2)} \times \mathbf{H}^{(1)} \cdot \hat{\mathbf{n}} ds \tag{5.15}$$

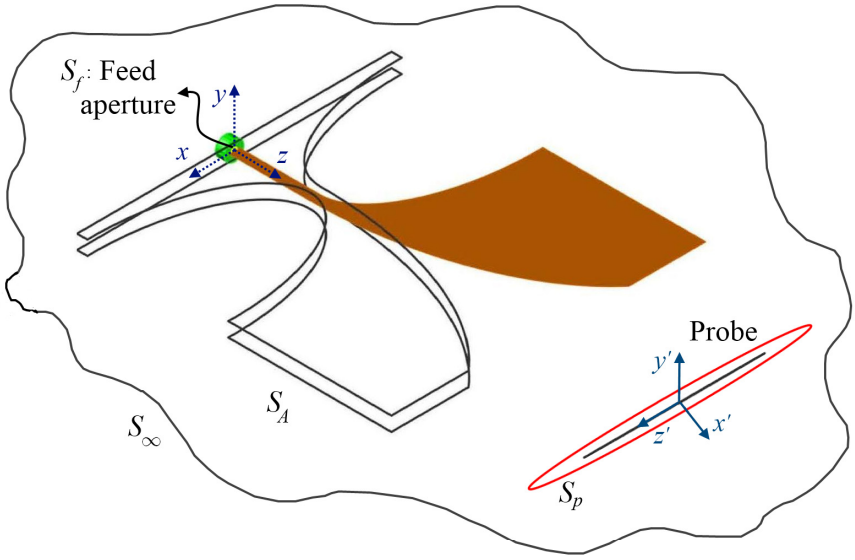

Figure 5.9: A DLVA in close proximity of a thin wire probe.

5.3.3 The Relationship between Scattering Parameters and Fields

In this section the use of scatterer probes in a system consisting of a multitude of antennas and probes are studied. Suppose that a number of near-field probes are added into the system described in Chapter 3. Note that the antennas are connected to a 24-port RF switch network, followed by a 2 port VNA. In this configuration only one antenna is activated as a transmitter while the remaining antennas are kept loaded with a matched load in the switch network. The general configuration of this problem is shown in Figure 5.10. As shown in this figure, for each measurement a Tx antenna is activated and a collector antenna collects the field. Each element of this measurement system contains an arbitrarily-defined reference feed plane, also called a port. Each port i, is associated with an incident wave a_i, and a reflected wave b_i. The voltage V_i and current I_i at each port are related to the a_i and b_i parameters

as [64]

$$V_i = (a_i + b_i)\, Z_{ci} \qquad I_i = (a_i - b_i)\, /Z_{ci} \tag{5.16}$$

where Z_{ci} is the characteristic impedance of the port i.

In Figure 5.10, there are m remaining inactive antennas which are matched-loaded by the RF switch network, thus $a_i = 0$ for $i = 1...m$. If the collector and the Tx antennas are the same, this is a mono-static setup and if they are separated, it is referred to as bi-static setup.

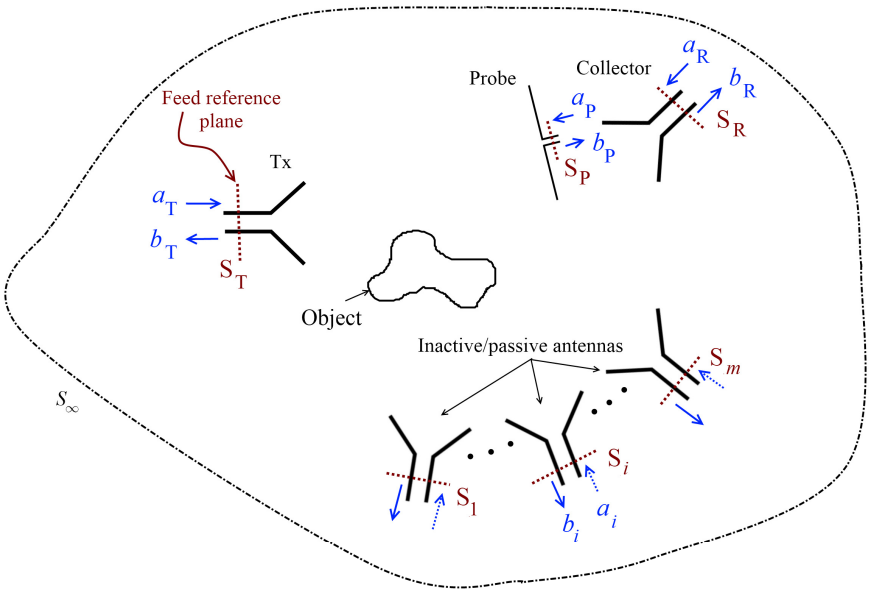

Figure 5.10: A multi-antenna system with scatterering probe.

Let's denote a Tx antenna's port by T and a probe's port by P. Since the VNA measures scattering parameters $[S]$, the relation between $[S]$ and field at the probe's location should be determined. Referring to Figure 5.10, this problem can be divided into two cases

- Case (1): The Tx is activated at S_T with incident wave $a_T^{(1)}$ while the probe is loaded by an arbitrary impedance Z_L. A current $I_P^{(1)}$ appears at the port

terminal P.

- Case (2): The probe is activated by an arbitrary source V_{th}^{P}. The VNA detects an incoming wave $b_T^{(2)}$ at port S_T. The current at the probe's port is now denoted by $I_P^{(2)}$.

These two cases and the probe's equivalent circuit model are depicted in Figure 5.11.

In these two cases, different field distributions are obtained. These fields are denoted as $(\mathbf{E}^{(1)}, \mathbf{H}^{(1)})$ and $(\mathbf{E}^{(2)}, \mathbf{H}^{(2)})$ for the cases (1) and (2), respectively. Applying the reciprocity theorem (5.15) on the reference ports

$$\int_{S_T \cup S_P \cup S_i} \mathbf{E}^{(1)} \times \mathbf{H}^{(2)} \cdot d\bar{s} = \int_{S_T \cup S_P \cup S_i} \mathbf{E}^{(2)} \times \mathbf{H}^{(1)} \cdot d\bar{s} \tag{5.17}$$

Let's denote the associated voltages and currents of the ports T, P, and is with (V_T, I_T), (V_P, I_P), and (V_i, I_i)s, respectively. At each port reference plane, the electric field, $\mathbf{E}$, and the magnetic field, $\mathbf{H}$, can be replaced by their corresponding voltage, V, and current, I, respectively [64], thus

$$V_T^{(1)} I_T^{(2)} + V_P^{(1)} I_P^{(2)} + \sum_{i=1}^{m} V_i^{(1)} I_i^{(2)} = V_T^{(2)} I_T^{(1)} + V_P^{(2)} I_P^{(1)} + \sum_{i=1}^{m} V_i^{(2)} I_i^{(1)}$$

After rearranging the equation and moving the probe's terminal to the right side

$$V_T^{(1)} I_T^{(2)} - V_T^{(2)} I_T^{(1)} + \sum_{i=1}^{m} \left(V_i^{(1)} I_i^{(2)} - V_i^{(2)} I_i^{(1)} \right) = V_P^{(2)} I_P^{(1)} - V_P^{(1)} I_P^{(2)} \tag{5.18}$$

On the antenna side, one can measure the scattering parameters using a VNA, thus the port voltages and currents (V_T, I_T) and (V_i, I_i) can be converted to their equivalent (a_T, b_T) and (a_i, b_i) using (5.16). Note that the inactive DLVAs are connected to a

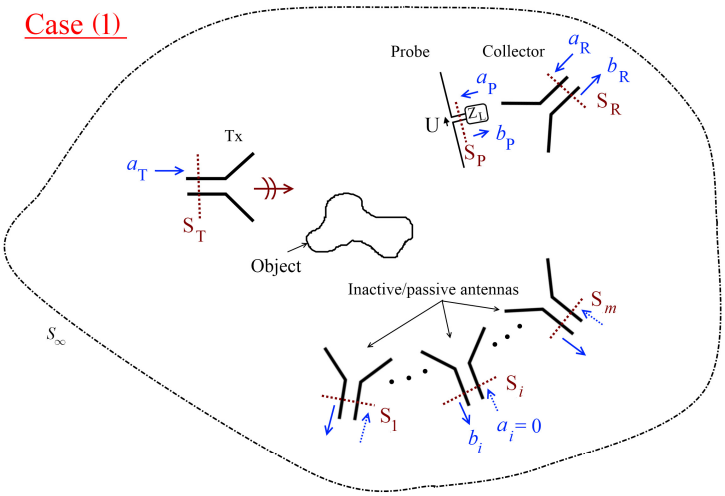

(a)

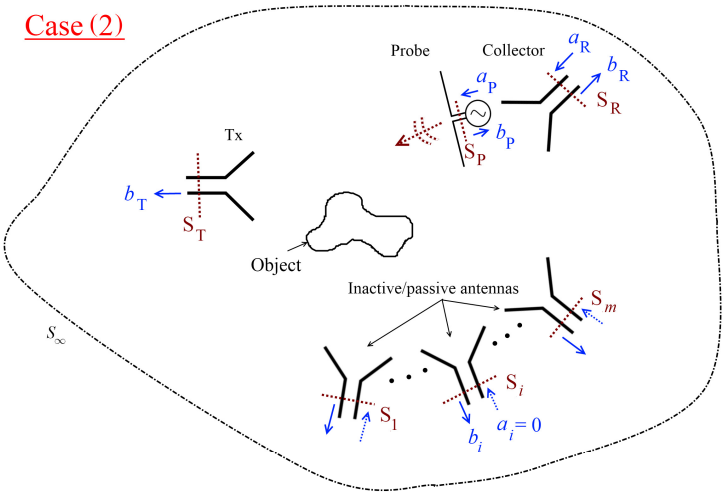

(b)

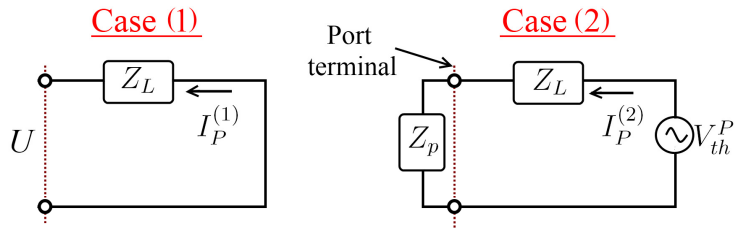

(c)

Figure 5.11: Probe-antenna reciprocity cases and the probe equivalent circuit model.

matched load (RF switch network), thus $a_i^{(1)} = a_i^{(2)} = 0$ for $i = 1...m$. For each inactive antenna i, its port voltage and current can be calculated from (5.16) which results in

$$V_i^{(1)} I_i^{(2)} - V_i^{(2)} I_i^{(1)} = (a_i^{(1)} + b_i^{(1)})(a_i^{(2)} - b_i^{(2)}) - (a_i^{(2)} + b_i^{(2)})(a_i^{(1)} - b_i^{(1)})$$

Since $a_i^{(1)} = a_i^{(2)} = 0$

$$(a_i^{(1)} + b_i^{(1)})(a_i^{(2)} - b_i^{(2)}) - (a_i^{(2)} + b_i^{(2)})(a_i^{(1)} - b_i^{(1)}) = 0$$

The same calculations for the remaining inactive antennas results in

$$\sum_{i=1}^{m} \left(V_i^{(1)} I_i^{(2)} - V_i^{(2)} I_i^{(1)} \right) = 0$$

Moreover, in "Case 2" the probe is transmitting and the Tx is connected to VNA, thus $a_T^{(2)} = 0$ and

$$V_T^{(1)} I_T^{(2)} - V_T^{(2)} I_T^{(1)} = (a_T^{(1)} + b_T^{(1)})(a_T^{(2)} - b_T^{(2)}) - (a_T^{(2)} + b_T^{(2)})(a_T^{(1)} - b_T^{(1)}) = -2a_T^{(1)} b_T^{(2)}$$

Since V_P^{th} is an arbitrary source and it can be adjusted so that $I_P^{(1)} = I_P^{(2)} = I_P$. Thus, equation (5.18) is simplified to

$$-2a_T^{(1)} b_T^{(2)} = (V_P^{(2)} - V_P^{(1)}) I_P \tag{5.19}$$

$b_T^{(2)}$ is just due to the voltage source V_{th}^P in "Case (2)". The probe equivalent circuit model is shown in Figure 5.11 (c). In "Case (1)", due to the presence of the field at the probe's port, a voltage $U = \int \mathbf{E} \cdot d\mathbf{l} \approx E_p \; l$ is generated in this port where E_p

is the field polarization component parallel to the probe and l is the probe effective length. Note that it was shown in Section 5.3.1 that the probe only interacts with the component of field parallel to its axis.

From the circuit model shown in Figure 5.11 (c)

$$I_P = U/Z_L \quad , \quad V_p^{(1)} = U \quad , \quad V_p^{(2)} = Z_p I_P = (Z_P/Z_L)U$$

Thus equation (5.19) simplifies as

$$2a_T^{(1)} b_T^{(2)} = -U^2 \left[\frac{Z_P + Z_L}{Z_L^2} \right] \tag{5.20}$$

The reflection coefficient $S_{11}^{Probe_i}$ due to the $Probe_i$ is calculated as

$$S_{11}^{Probe_i} = \frac{b_T^{(2)}}{a_T^{(1)}} = -U^2 \left[\frac{Z_P + Z_L^i}{2(Z_L^i)^2 (a_T^{(1)})^2} \right] \tag{5.21}$$

where $(a_T^{(1)})^2$ is the incident power and Z_L^i is the impedance load for the probe. It is clear that the $S_{11}^{Probe_i}$ is proportional to U^2 or the field squared value at the probe's location and it is also related to Z_L^i.

Note that the measured S_{11} by the VNA also contains the reflected wave $b_T^{(1)}$ which is due to the "Case (1)". The antennas and other probes in the system contribute in $b_T^{(1)}$

$$S_{11} = \frac{b_T^{(1)} + b_T^{(2)}}{a_T^{(1)}} = S_{11}^{Probe_i} + S_{11}^{others} \tag{5.22}$$

In a system with multiple probes all of the probes contribute to the S_{11}. Their contribution is denoted as S_{11}^{others} in equation (5.22). In order to measure the field at the i^{th} probe's location, one can change (modulate) the Z_L^i of this probe. Since only this probe's impedance has changed, S_{11}^{others} does not change and the measured S_{11}

due to two Z_L^is are

$$S_{11}^{Z_{L1}^i} = S_{11}^{Probe_i, Z_{L1}^i} + S_{11}^{others}$$
$$S_{11}^{Z_{L2}^i} = S_{11}^{Probe_i, Z_{L2}^i} + S_{11}^{others}$$

Subtracting the two measurements

$$\delta S_{11} = S_{11}^{Z_{L1}^i} - S_{11}^{Z_{L2}^i} \propto (E_p^i)^2 \tag{5.23}$$

where E_p^i is the field component at the i^{th} probe's location. In mono-static case, the presence of squared field value in (5.23) introduces a 180° phase ambiguity for the field calculation. In order to accurately measure the field, one can use the bi-static approach. In the bi-static measurement S_{21} parameter is recorded between the Tx antenna and a separate collector antenna, see Figure 5.10. By repeating the same steps that were presented for mono-static measurement, it can be shown that δS_{21} is proportional to the field at the probe's location and there is not any phase ambiguity in measurement.

5.4 Conclusion

In this chapter, the near-field measurement techniques were reviewed and an overview of MST systems for MI was given.

The standard method of implementing an MST system is to modulate a probe and then use a coherent detector for field extraction. Additionally, a theoretical background of a new approach using a VNA was presented where the number of antennas and probes were arbitrary. In the proposed approach, instead of a coherent

detector, the scattering parameters were collected using the VNA.

In order to determine a field at a specific location, the impedance of the corresponding probe was changed while the remaining components of the system remained unchanged. The change of impedance introduces a differential δS_{11} in the mono-static approach or δS_{21} in the bi-static approach. These two measurements are proportional to the second power of the electric field, or to the field at the probe's location, respectively.

In the next chapter, a novel system implemented based on this approach is presented and its performance is investigated.

Chapter 6

Near-Field Microwave Imaging System based on the Scatterer Probe Technique

The direct MWT system was introduced in Chapter 3. Then the basic principle for an indirect MWT system was reviewed in Chapter 5. In this chapter, a novel MWT system is introduced which is based on the use of specially designed scatterer probes and it takes advantage of both direct and indirect measurement techniques.

Due to the inherent non-linear and ill-posed behavior of the inverse scattering problem, a substantial amount of electromagnetic scattering data must be collected in order to ensure a robust and quantitatively accurate image. For purposes of collecting sufficient data, the direct approach suffers from some drawbacks. Unfortunately, the need for a high density of measurement points conflicts with another important design consideration: the need for a sufficiently large spatial separation of the antennas in order to minimize the mutual coupling. As discussed in Chapter 4, strong mutual coupling may prevent the convergence of algorithms. Moreover, when all polarizations of the impinging fields contribute to the received voltage it is difficult to relate the measured voltage to a single polarization and a unique potential advantage of MWT over other modalities, the polarization, is lost.

As was mentioned earlier, there are two common approaches for data acquisition in current MWT systems, both of which ultimately measure the voltage at the port of one or more receiving antennas in the system. In the first approach, the direct

approach, the measured voltage is used to infer the electromagnetic field impinging *directly* on the receiving antenna. Its configuration is shown in Figure 5.6 (a). This requires that some sort of antenna factor be, implicitly or explicitly, part of the calibration procedure. It also requires that the receiving antenna be located at the points where the electromagnetic field needs to be measured. This has been accomplished by either repositioning the receiving antenna, or using an array of co-resident receiving antennas. Various types of antennas have been used in conjunction with this approach, *e.g.*, monopoles [6], open-ended waveguides [49], and the DLVAs that was used in the UM direct system.

The second approach, the indirect approach, uses the measured voltage at the receiving antenna to infer the electromagnetic field impinging on a probe positioned at some distance from the receiving antenna. Its configuration is shown in Figure 5.6 (b). In an early use of this approach [26], an array of dipole probes was positioned in front of a single receiving antenna, in this case a horn antenna. In the state-of-the-art use of this indirect method for microwave tomography, two horn antennas having a 30 cm square aperture are located on either side of a water tank and used as the sole Tx and the sole Rx [75]. The distance between the two horn apertures is 20 cm and a 32×32 array of dipole probes is positioned in front of the Rx antenna. Each probe is loaded using a PIN diode and is sequentially modulated at a low frequency, producing a scattered field at the Rx antenna, thus it is an MST technique. As discussed in Chapter 5, this probe-scattered field is proportional to the original field at the probe location.

This indirect approach of measurement offers several advantages over the direct approach. Firstly, increasing the number of observation points can be easily accommodated by simply adding more probes, whereas in the direct approach this

requires either adding more antennas to the co-resident antenna array or accurately re-positioning the Rx antenna or array to more physical locations. Physically re-positioning is difficult and time consuming to perform accurately. Increasing the size of the co-resident array is not only expensive because of the need for RF switches, but adding array elements increases the mutual coupling which must then be taken into account in the imaging algorithm and calibration procedure. Adding more probes is usually a simple matter and the probe modulation is achieved using inexpensive low frequency switching circuitry. In addition, the mutual coupling between probes is much less than that between Rx antennas, especially, because only one probe is "activated" at a time (the remaining probes are kept "open" and therefore have minimal interaction with the RF field). On the other hand, because the probe-scattered field, upon which the indirect approach relies, is relatively small, custom coherent detectors are typically used for such systems. This requires measurement averaging over a large number of modulation cycles to improve the signal-to-noise (SNR) ratio. In [75] the data is averaged over 500 measurements. Due to the small probe-scattered field, the probes must be placed close to the Rx antenna limiting the number of locations surround the OI at which the probes can be placed.

To the best of author's knowledge, only bistatic MST has been reported for imaging applications (*e.g.* see [26, 75] and [88]). In the bistatic implementation, there is only one Rx and one Tx antenna, incorporated with an array of probes in front of the Rx.

In the proposed system introduced here, which is referred to as the enhanced indirect system, a combination of the direct and indirect methods is utilized for the MWT application. Its configuration is shown in Figure 6.1. The purpose is to quantitatively investigate the performance of the proposed technique where instead

of using a single Tx, and an array of probes in front of a single Rx antenna, each DLVA of the air-based system is equipped with a scatterer probe in its vicinity (for a total of 24 probes). These probes surround the OI with equal angular spacing of 15°. Each probe is simply a printed dipole whose impedance is changed electronically by biasing the 5 equally separated PIN diodes located along its length. The routing of the biasing wires is chosen, via accurate field simulations of the DLVA/probe setup, so as to minimize any field perturbations. It is shown that increasing the number of PIN diodes decreases the interaction of the probe-receiver antenna, but interaction between each DLVA and its probe still exist. In the last section of this chapter, the number of antennas is reduced so that the number of probes are greater than the number of collectors and the probe-collector interaction changes significantly.

Measurements to collect field data within the MWT chamber are performed by successively activating and deactivating each scatterer-probe. While the impedance of the active probe is changed, the remaining probes are kept "open". The "closing" and "opening" of the active probe generates a differential signal at each of the DLVAs. This differential signal is strongest at the DLVA nearest to the "collector". A data acquisition program connects the nearest collector to the VNA and records the differential signal, which is proportional to field at the active probe's location.

Different OIs including a complicated target (the e-phantom), two nylon rods, a combination of PVC with a nylon rod and a dielectric phantom which is referred to as the bear-face phantom are used to test the proposed system. Images of the OIs are successfully reconstructed using the MR-GNI algorithm.

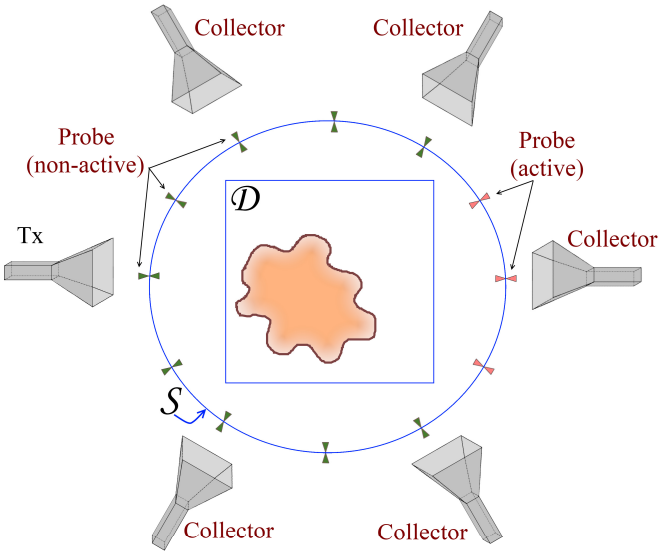

Figure 6.1: Enhanced indirect MWT system.

6.1 System Description

The dimensions of the measurement chamber and a block diagram of the system are provided in Figure 6.2 (a) and (b), respectively [89]. A photo of the system during the measurement of the e-phantom object is shown in Figure 6.3.

The measurement system consists of four subsystems:

1. **Measurement Chamber and Antennas**

   Twenty four DLVAs are mounted on a Plexiglas cylinder, 50.8 cm tall, with equal angular spacing of 15°. As discussed in Section 3.1.1, the DLVA is designed for the ultra wideband frequency range of 3.1 GHz to 10.6 GHz. Compared to a single layer Vivaldi antenna, the double layer version presents at least a 10 dB improvement in the cross polarization performance [62]. The low cross-polarization of these antennas is an advantage for the imaging algorithm which assumes a 2D transverse magnetic field distribution, or simply just assumes that

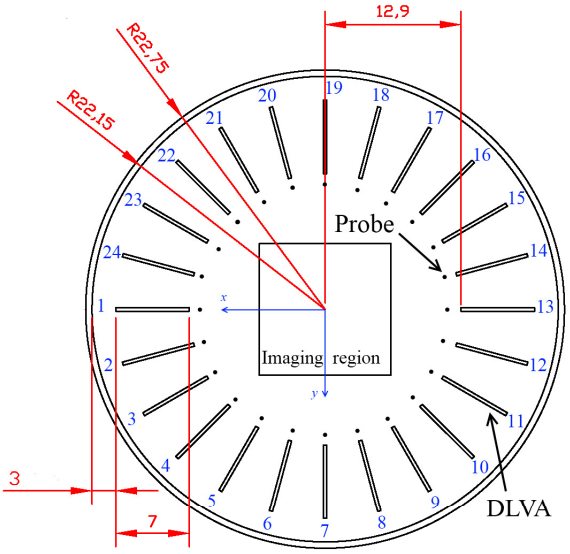

(a)

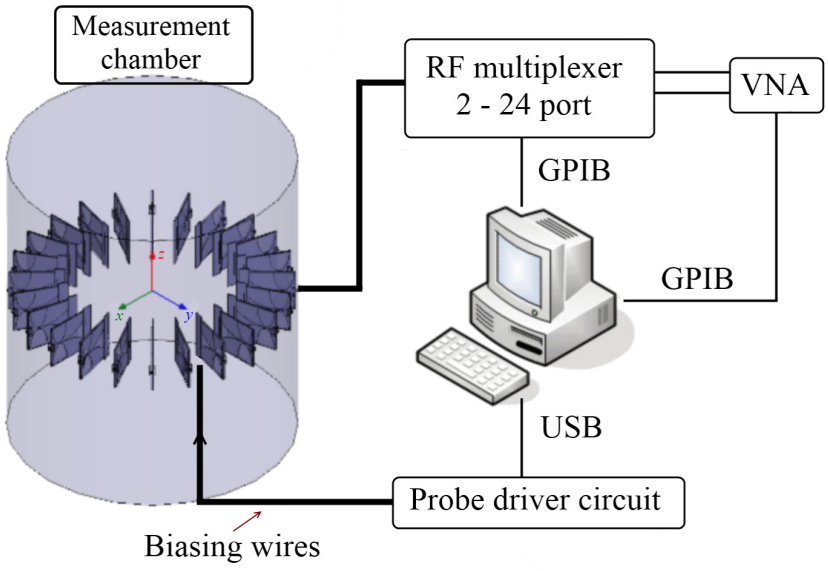

(b)

Figure 6.2: (a) Top-view of the hybrid measurement chamber (dimensions are in cm) and (b) the block diagram of the hybrid MWT system.

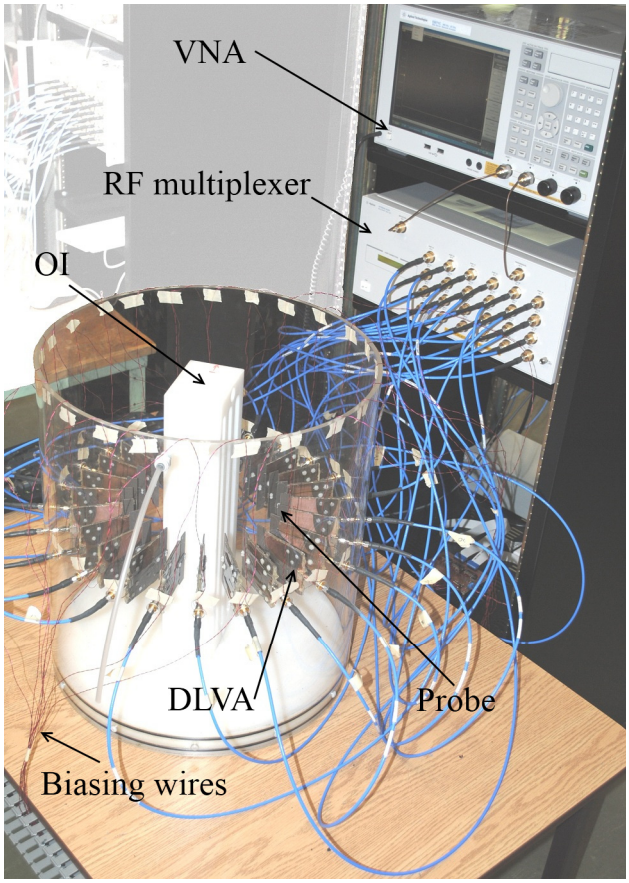

Figure 6.3: A picture of measurement system during collection of the e-phantom dataset (the complexity test).

only E_z exists. The overall size of each DLVA is 7 cm by 7 cm (see Chapter 3). The only difference with respect to the previous direct experimental system is that each DLVA is now equipped with a scatterer probe, located at a distance of 3 mm in front of it. The imaging region is a centered square, depicted in Figure 6.2 (a).

2. **RF Multiplexer and VNA**

   A 2 to 24 port RF electromechanical multiplexer (Agilent 85070A) is used to switch to a chosen active Tx or Rx antenna/collector. The isolation between ports is 95 dB. The multiplexer is connected to 2 ports of an Agilent 5071C VNA. The multiplexer and the VNA are both controlled by the data acquisition program via the controller computer unit. Their connection is established through a GPIB.

3. **Probe Driver Circuit**

   In order to switch the probes to close/open states, which correspond to forward/reversed biases of PIN diodes, respectively, a 24 Darlington-pair transistor array is used. The transistors are connected to a 24-port USB I/O card, which is controlled by the data acquisition program. Using high precision resistors, the forward bias current for all 24 probes are adjusted with less than 1% tolerance.

4. **Controller Unit**

   A data acquisition program controls all the instruments. A computer is directly connected to the "probe driver circuit" module via a USB connection. The multiplexer and the VNA are connected through a GPIB-Ethernet hub. For collecting each dataset, a Tx antenna is first chosen by switching it to one of

the VNA ports. For each Tx antenna, the other 23 Rx antennas are switched sequentially to the second port of the VNA, resulting in 24×23 = 552 measurements at each frequency. Each collector (Rx DLVA) collects two measurements, one with the nearest probe closed and one with the nearest probe opened. During these two measurements the remaining probes are kept open (thus they have minimal effects on the measurements). The total data acquisition time for each frequency is less than 4 minutes. Currently the acquisition time is limited to the mechanical RF-switch settling time.

6.2 Probe Design

Each scatterer probe consists of a printed dipole on a small piece of substrate of the same type as is used for the DLVA (Arlon DiClad 527, thickness 62.5 mil, relative permittivity of 2.5). The probe length and width are 42.8 mm and 0.5 mm, respectively. This corresponds to a half-wavelength at 3.505 GHz.

To open and close each probe, 5 PIN diodes are placed in series at equally spaced positions on the probe. Each probe substrate is attached to a DLVA using two small Nylon screws (2 mm). The distance between probe and DLVA is 3 mm with the probe aligned with the DLVA. This is because E_z is required for the imaging algorithm.

6.2.1 PIN Diode Characterization

The PIN diode equivalent circuit model for the forward and reversed bias cases is shown in Figure 6.4. Currently, BAR64-02V PIN diodes from Infineon are used in the system. In order to model the presence of the PIN diodes, one requires a simulation method that combines a full-wave solver and a circuit simulator. Developing

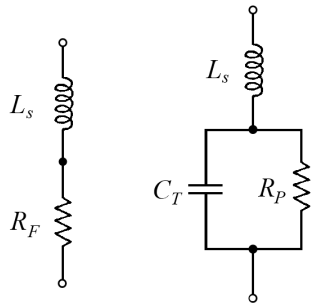

Figure 6.4: Equivalent circuit for the PIN diode, left: forward bias (close), right: reversed bias (open).

such a combined simulation tool enables us to calculate the equivalent circuit of the PIN diode using an optimization method. The S_{21} coefficient of the diode on a 50 Ω transmission line is provided by the factory. The Ansoft Nexxim circuit solver was used to simulate the circuit part (Figure 6.4) and Ansoft HFSS FEM solver to simulate a 50 Ω microstrip transmission line. Using the combined simulation, which is referred to as the *circuit-FEM* solver, and the quasi-Newton optimization technique, the equivalent circuit components were calculated. The optimized values are listed in Table 6.1. A comparison of the calculated S_{21} and the factory data is shown in Figure 6.5. There is a good agreement between the model used and the factory data.

Table 6.1: PIN diode calculated equivalent circuit parameters based on Figure 6.4.

Symbol	Value
R_F	0.5 Ω
L_s	0.6 nH
R_P	4.0 KΩ
C_T	0.0718 pF

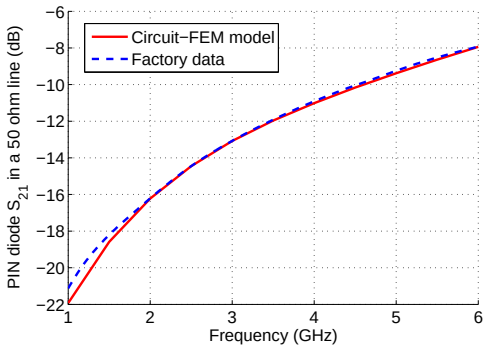

Figure 6.5: PIN diode reverse bias insertion loss from factory data and optimized circuit model.

6.2.2 Probe Configuration

Using the circuit-FEM solver, the reflection coefficient of the DLVA was simulated in two cases:

1. When the probe is closed (forward biased diodes).

2. When it is opened (reversed biased diodes).

The simulation geometry is shown in Figure 6.6. Also the effect of using different numbers of PIN diodes was studied. For this study, three different simulations were performed:

1. A probe with single diode located at its center.

2. A probe with three diodes in series.

3. A probe with five diodes in series.

In all cases, the diodes are located equally spaced along the probe. In the closed case, the changes of reflection coefficient for the 3 cases are negligible (less than 0.2 dB). This is due to the small insertion loss of the PIN diodes. In the open case,

increasing the number of PIN diodes resulted in a performance more similar to the DLVA alone. These results are compared in Figure 6.7. According to this comparison, it was concluded that increasing the number of PIN diodes decreases the interference of the generated fields of the DLVA in Tx mode; thus, the 5-PIN diode configuration was chosen.

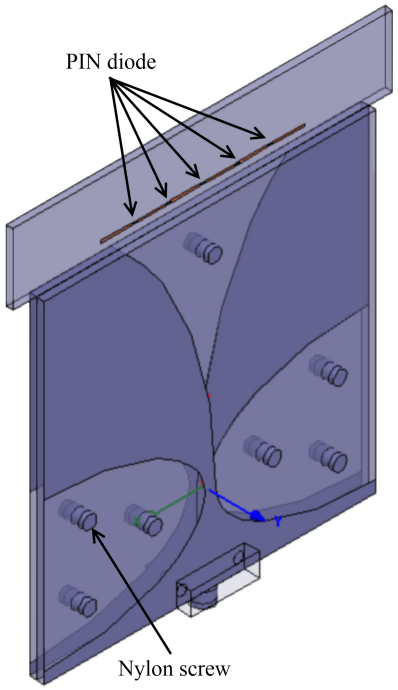

Figure 6.6: Simulating the probe-DLVA response, using the circuit-FEM solver.

6.2.3 Designing the Biasing Route

The bias current is a DC current and does not interfere with the RF signal, however, the biasing circuitry and wires must not significantly perturb the fields. Thus, FEM (Ansoft HFSS) was used to numerically model the field distribution in the vicinity of the DLVAs at various frequencies, so as to determine the optimal routing of the biasing circuitry and wires.

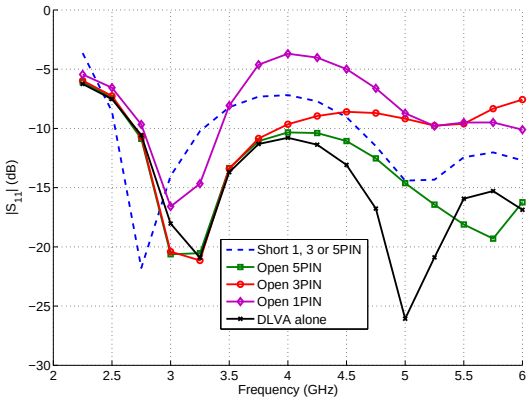

Figure 6.7: Simulated reflection coefficient of a DVLA near a probe loaded with 1, 3, and 5 PIN diodes, in series.

Figure 6.8 (a),(b) shows the distribution of fields at 3.5 GHz and 5.0 GHz, respectively. As shown in the figure, the field intensity is stronger at the corners of the DLVA and they are in different directions, however, the central region shows a smaller variation of fields and the field vectors are, mostly, along the z-axis. Based on these observations, and considering the probe length, a bias line parallel to the x-axis was chosen, between the nylon screws. Rosin is used as the adhesive to secure the biasing wires to the DLVA. A picture of the probe mounted in front of the DLVA is shown in Figure 6.9. Two surface mounted "termination" resistors are added to either side of the probe. These resistors "terminate" the RF current at both ends of the probe. Using this configuration, the measurements showed that the changes of the reflection coefficient due to the presence of the biasing wires is less than 2 dB within the frequency range of 1 GHz to 6 GHz. Also some other routes were tried, *e.g.* from the corners of the DLVA. Measurement results show that the biasing wires along other routes interfere with the DLVA by more than 5 dB.

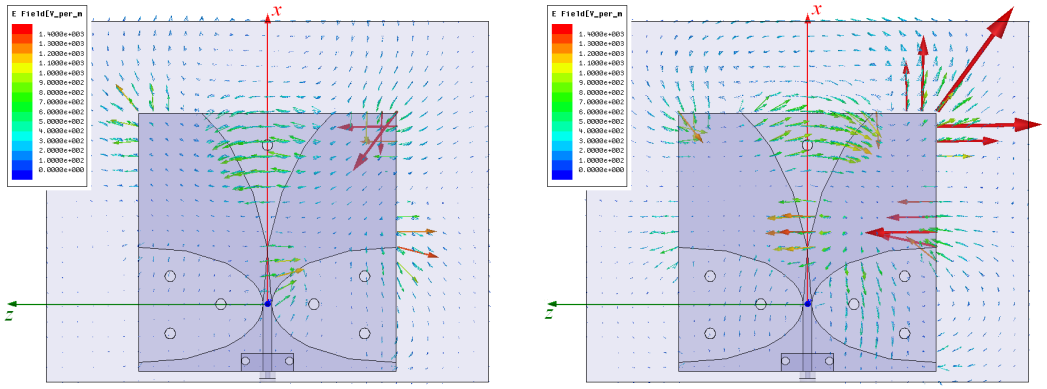

(a) (b)

Figure 6.8: Field distribution of single DLVA alone, (a) 3.5 GHz, (b) 5.0 GHz.

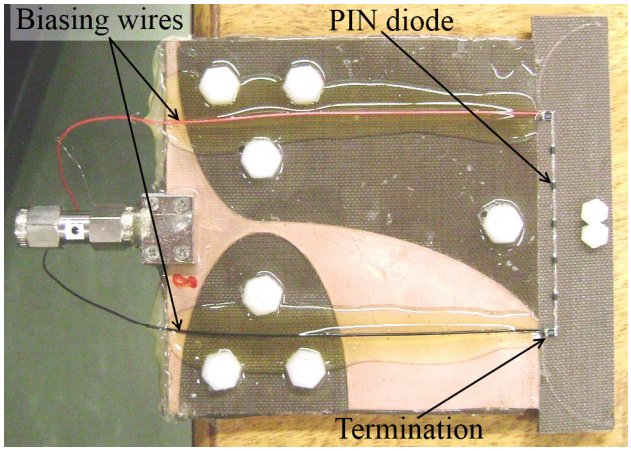

Figure 6.9: Fabricated DLVA and a probe.

6.3 Measurement Method and Data Collection

For the imaging algorithm, the field scattered by the OI is required at each probe location. Each measurement at a probe's location is performed by changing the impedance of that probe. The probe whose impedance is changing is called the active probe. When a probe is active, the remaining probes are kept "open" so as they remain "invisible" to electromagnetic fields. The impedance change produces a change in the measured voltage at the nearest collector (Rx DLVA) which is proportional to the field at the active probe's location. Here, this is called the *MST procedure*.

To measure the scattered field, the total field (*i.e.*, with the OI present in the measurement chamber) and the incident field (*i.e.*, with the OI absent in the measurement chamber) are collected using the MST procedure. Thus, with one Tx DLVA transmitting, the impedance of each active probe is changed by opening and closing its diodes, while keeping all of the remaining probes open. The Tx DLVA is connected to one port of the VNA while the nearest collector to the active probe (Rx DLVA) is connected to the second port of the VNA. The impedance change of the active probe in front of the collector, generates a change in VNA transmission coefficient S_{21} between the Tx DLVA and the collector. Denoting the measured scattering parameters in the two cases of closing and opening the active probe as S_{21}^{sc} and S_{21}^{oc}, respectively, the difference between these two measurements is defined as $\delta S_{21} = S_{21}^{sc} - S_{21}^{oc}$.

Once the incident (no OI present) and total (OI present) fields are measured by this technique, the scattered field generated by the OI is calculated by subtracting the total and incident fields: $E_z^{sct} = E_z^{tot} - E_z^{inc}$, see (2.6). The total and incident fields are thus proportional to δS_{21}^{tot} and δS_{21}^{inc}, respectively, thus the scattered field due to the object of interest satisfies: $E_z^{sct} \propto \delta S_{21}^{sct}$ where $\delta S_{21}^{sct} = \delta S_{21}^{tot} - \delta S_{21}^{inc}$.

In the experimental system, the thin probes are parallel to the z direction and

they interact mainly with E_z. A current is generated on the probe that is proportional to the E_z field component. The MST procedure is based on the assumption that the differential δS_{21}, is proportional to the field at the probe's location. The theoretical background of this statement is discussed in detail in [84] and Chapter 5.

Note that the MST procedure is effective in removing some sources of experimental error, *e.g.*, errors due to cable movement, as well as the noise generated in the multiplexer unit and the network analyzer. The time interval between the two MST measurements is very short and it is assumed that the cables remain stationary and unchanged during this interval.

6.3.1 Probe Calibration

As was discussed for the direct system, see Chapter 4, the 2D imaging algorithm models neither the antennas nor the entire 3D measurement system including the probes. Moreover, the field excitation is implemented by a line-source placed at the Tx antenna's location, instead of a DLVA in the presence of co-resident DLVAs. Finally, in addition to modeling error, measurement errors must also be taken into account. To reduce the effects of these errors, the data collected by the probes should be calibrated. To calibrate the data, a PEC cylinder, 3.5 inches in diameter, was used as the reference object. It is the same reference object used in the direct system. The scattered field produced by this reference object is collected using the MST procedure, as discussed in the previous section. For any active transmitter, an individual calibration factor is defined for each probe. That is $23\times24 = 552$ calibration factors are defined for each frequency of operation. For an active transmitter, the calibration factor at each probing site, CF^{MST}, is calculated similar to (4.3) and it is the ratio of analytical scattered field by the PEC cylinder to the measured scattered

field at that probe's location:

$$\mathcal{C_F}^{MST} = E_{z,ls}^{sct-PEC} / \delta S_{21,meas}^{sct-PEC} \tag{6.1}$$

where $E_{z,ls}^{sct-PEC}$ is the analytical solution of the scattered field by the PEC cylinder in the vicinity of a line source, and $\delta S_{21,meas}^{sct-PEC}$ is the measured data which is proportional to the actual scattered field in the presence of the PEC cylinder. A comparison of the amplitude and phase of $E_{z,ls}^{sct-PEC}$ and $\delta S_{21,meas}^{sct-PEC}$ at 4.5 GHz is shown in Figure 6.10. 552 calibration factors are stored in the column vector $\underline{CF^{MST}} \in \mathbb{C}^{552}$. The measured

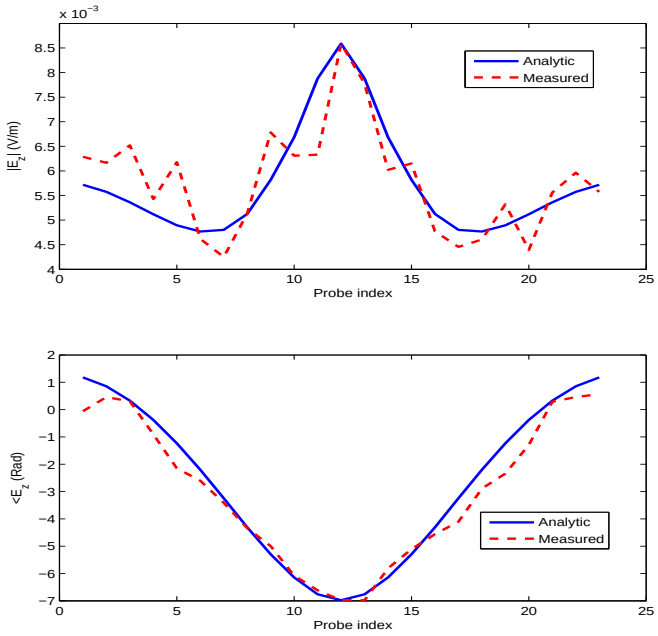

Figure 6.10: Comparison of the amplitude and phase of the scattered field by the reference PEC cylinder from the analytical solution and the scaled MST measurement at 4.5 GHz.

δS_{21}^{sct}, which represents the scattered field due to the OI at a specific frequency, is also stored in the column vector $\underline{\delta S_{21}^{sct}} \in \mathbb{C}^{552}$. The calibrated measured scattered field data, denoted by $\underline{E_{meas}}$, is then obtained as $\underline{E_{meas}} = \underline{CF^{MST}} \odot \underline{\delta S_{21}^{sct}}$ where $\odot$

denotes the Hadamard product between two vectors of the same size. This calibrated scattered field is then used by the inversion algorithm to reconstruct the relative complex permittivity of the OI.

6.3.2 Probe Sensitivity to the Incident Power

In order to measure the field at the probe location, the changes of the probe impedance should be detectable by the VNA. This parameter is referred to as the sensitivity of the probe to the input power to the chamber. The incident field was measured at each of the 24 DLVA locations, while the VNA output power was set to -5 dBm. For each measurement, the impedance of the nearest probe to the receiver DLVA was changed in order to record δS_{21}. Choosing the two antennas with greatest separation, that is, choosing antennas "1" and "13" (Figure 6.2 (a)) as the transmitter and the receiver, respectively, the lowest δS_{21} was observed to be greater than -50 dB. This measurement is shown in Figure 6.11 (a) over the bandwidth of interest. For the same Tx/Rx pair, which produced the lowest δS_{21}, the VNA output power was decreased from -5 dBm, in steps of 5 dB, down to the -35 dBm. At an output power level of -35 dBm the measurements reached the noise floor, and thus, it is concluded that the probes are sensitive to an input power as low as -30 dBm. For this measurement, none of averaging techniques were used to reduce the noise floor.

In addition to the δS_{21} measurement, the change of reflection coefficient of the receiver antenna was measured that is an indication of probe interaction with the receiver. The change of the reflection coefficient, δS_{22}, of one of the DLVAs was collected in the measurement chamber when the nearest probe impedance was changed. As shown in Figure 6.11 (b), the reflection coefficient is in the range of -15 dB to -23 dB, at the frequency range of 3 GHz to 6 GHz. Figure 6.7 illustrates the simu-

lated "open" and "short" cases of the idealized configuration shown in Figure 6.6. In simulation, the presence of the co-resident DLVAs nor the biasing circuitry were not considered. Therefore, Figure 6.6 and Figure 6.11 (b) are presented separately.

Averaging the measured data was also investigated, so as to improve the SNR. In this technique, the signal is averaged over a number of repeated measurements to obtain a higher SNR; *e.g.* 500 times averaging has improved SNR in the order of 25 dB in the MWT system reported in [75]. Several datasets were collected using the enhanced indirect measurement system. For each dataset, the field was collected by applying the averaging of 1, 5, 10, 100, and 1000 times. The change of MST signal in all cases was less than 0.2 dB, while the VNA output power was set to -5 dBm. There were negligible changes observed in the datasets or in the images resulted from these datasets. It is concluded that averaging is therefore not required, allowing faster one-shot data acquisition.

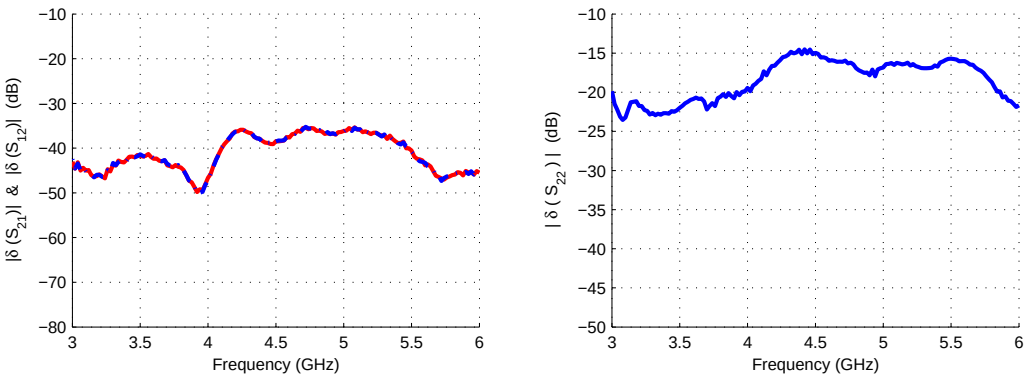

(a) (b)

Figure 6.11: (a) δS_{21} for the Tx:1 and the Rx: 13. Incident power is -5 dBm. (b) δS_{22} measurement in tomography system, as an indication of probe-DLVA interaction.

6.4 Inversion Algorithm for MST Dataset

Again, let's denote the imaging and measurement domains by $\mathcal{D}$ and $\mathcal{S}$, respectively; both of which are in $\mathbb{R}^2$, see Figure 6.1. In the direct system, $\mathcal{S}$ is not clearly defined, however here, $\mathcal{S}$ is precisely defined at the probes' locations. Let $\mathbf{r}$ denote the position vector in $\mathbb{R}$. The imaging domain is immersed in a known background having relative complex permittivity of ϵ_b, which contains a nonmagnetic OI with an unknown relative complex permittivity $\epsilon_r(\mathbf{r})$. (In this case, the background medium is air.) The contrast function $\chi(\mathbf{r})$ from equation (2.11), is to be found using the measured scattered field on $\mathcal{S}$. Once χ is found, the relative complex permittivity of the OI can be easily recovered. In this implementation, the contrast function is discretized into N square pulses; thus, the contrast function is represented by the complex vector $\underline{\chi} \in \mathbb{C}^N$. Assuming the two-dimensional transverse magnetic illumination, the electric field can be represented by a single component perpendicular to the measurement and imaging domains. Denoting $\underline{E_{meas-cal}}$ as the calibrated measured scattered field on $\mathcal{S}$ and $\underline{E_{sim}}$ as the simulated scattered field on $\mathcal{S}$ due to the predicted contrast $\underline{\chi}$, the MWT problem may be formulated as the minimization over $\underline{\chi}$ following data misfit cost-functional (2.26) in the GNI implementation. The method was introduced in Chapter 2.

6.5 Imaging Results

Using the proposed experimental system and the MR-GNI algorithm, the relative complex permittivity of three different dielectric OI tests are imaged. These tests include:

1. Resolution test: This test consists of two nylon rods, separated by 4 mm as

shown in Figure 6.12 (a). The dimensions are listed in Table 6.2. The relative permittivity of nylon is $\epsilon_r \approx 3.0 - j0.03$ [70]. For this test, the imaging region is a 12 cm square and is discretized to 60×60 pixels.

2. Combination test: Figure 6.12 (b) illustrates a combination of a PVC cylinder adjacent to a nylon rod, which is used for the combination test. The dimensions are listed in Table 6.2. PVC relative permittivity is $\epsilon_r \approx 2.5 - j0.01$ at 4.5 GHz [70]. For this test, the imaging region is a 17 by 17 cm square and is discretized to 70×70 pixels.

3. Complexity test: In this experiment, a complex e-phantom object, shown in Figure 6.12 (c) was used. Its relative permittivity is $\epsilon_r = 2.3$ [77]. For this test, the imaging region is a 13 cm square and is discretized to 80×80 pixels.

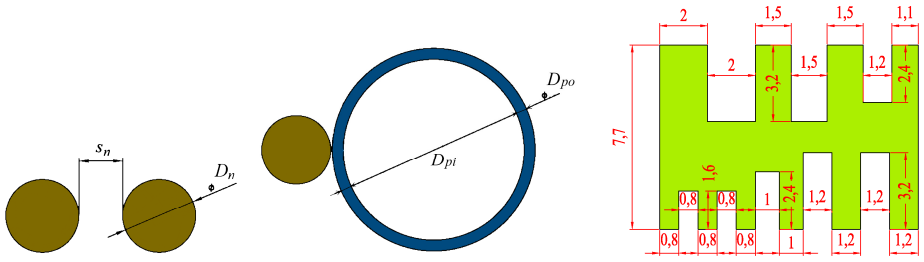

(a) (b) (c)

Figure 6.12: (a) Object for resolution test: 2 nylon cylinders with height of 44 cm. (b) Object of combination test, consisting of PVC and a nylon cylinder. (c) Object of complexity test: e-phantom made of UHMW. Dimensions in cm.

Table 6.2: Dimensions of OIs (cm) shown in Figure 6.12.

Symbol	D_n	s_n	D_{po}	D_{pi}
Dimension	3.8	0.4	13.0	10.2

These objects are positioned at the center of the measurement chamber. The MST dataset is collected at the frequencies of 3 GHz to 5 GHz with a step of 0.5 GHz. For

all cases, images of the OIs were reconstructed and we could see the OIs. In addition to the single frequency inversion, multiple frequency inversion was also utilized to reconstruct the OIs. In multiple frequency inversion, it is assumed that the dielectric properties of the OIs are invariant at all frequencies.

For the resolution test, results of the single frequency and the multiple frequency inversions are presented. For the complexity and the combination test, the single frequency image at 4.5 GHz and the multiple frequency image, are presented. It is speculated that the image at 4.5 GHz is the most uniform result due to minimum mismatch between the simulated and the measured data, corresponding to the reference object utilized for calibration at this frequency. Note that the images of other frequencies are not as uniform as 4.5 GHz.

Resolution test: Imaging results of this test using the single frequency inversion and the multiple frequency inversion are shown in Figure 6.13, where the separation changes from $\lambda/25$ at 3 GHz to $\lambda/15$ at 5 GHz. The real part of the nylons' reconstructed relative complex permittivity is close to its expected value (especially at 4.5GHz). Also note that the nylon rods are almost lossless; thus, the inversion algorithm is not capable of reconstructing the imaginary part of the relative complex permittivity of the nylon rods due to limited SNR ratio and dynamic range of the system.

Combination test: Imaging results of both multiple frequency reconstruction and single-frequency reconstruction are shown in Figure 6.14. For multiple-frequency inversion, the dataset at 3 GHz to 5 GHz with frequency step of 0.5 GHz is used.

Complexity test: Imaging results of single (4.5 GHz) and multiple frequencies are shown in Figure 6.15 (a)-(d). Similar to the results presented in [77] and [90], features with a minimum size of 1 cm and above are resolved while the two concave

features of 0.8 cm are not resolved.

In order to investigate the performance of the measurement system, a synthetic dataset is created with 3% additive white noise of the e-phantom (complexity test), according to the formula given in [91] as

$$\underline{E}^{sct}_{noise,t} = \underline{E_t}^{sct,fwd} + \max\left[\forall_t \underline{E_t}^{sct,fwd}\right] \frac{\eta}{\sqrt{2}} \left(\underline{\nu_1} + j\underline{\nu_2}\right) \tag{6.2}$$

where $\underline{E_t}^{sct,fwd}$ is the scattered field due to the t^{th} Tx on the measurement domain, $\mathcal{S}$, which is obtained by the forward solver. $\underline{\nu_1}$ and $\underline{\nu_2}$ are two vectors whose elements are random real numbers between -1 and 1 with zero-mean, and $\eta = 0.03$. $\underline{E}^{sct}_{noise,t}$ is the created synthetic dataset.

This synthetic data set is created with the Method of Moments, used for the forward solver, using 24 line sources positioned at the same location as the probes in the measurement system. Imaging results from this synthetic dataset are shown in Figure 6.15 (e)-(h).

6.6 Increasing the number of Probes per Collector

In the system discussed so far 24 DLVA collectors were utilized, each equipped with a single probe. In this system the probe-collector distance is constant, thus, their interaction does not change within the system. Due to the directive radiation pattern of the DLVA, it is interesting to study the performance of the system in a scenario with non-uniform distribution of probes with respect to the collectors.

In this section, the collectors are reduced while maintaining the number of probes. Thus, the number of probes is changed to be equal or greater than the collectors. Several systems were implemented where each collector interacts with 2 and up to 4

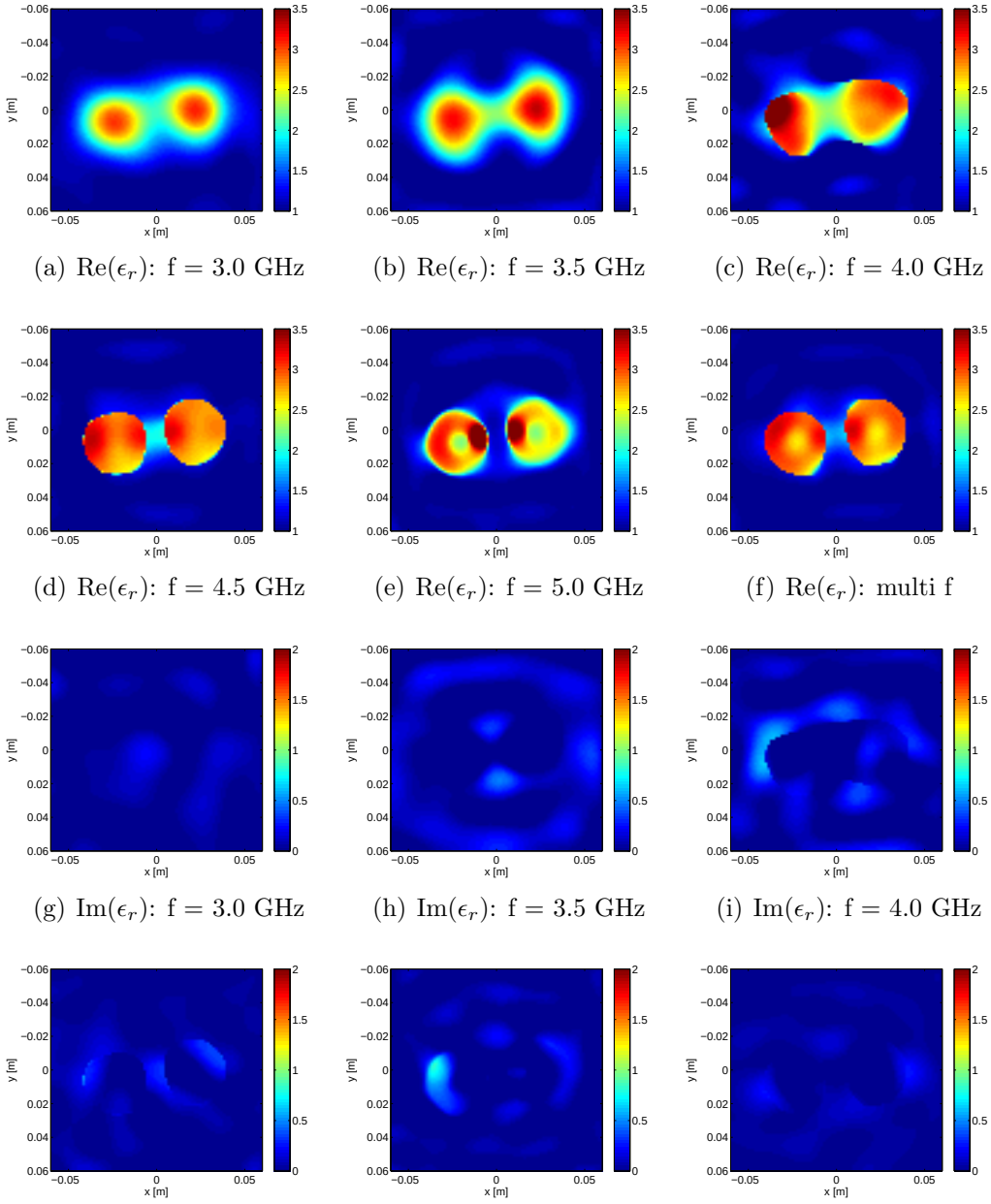

(a) Re(ϵ_r): f = 3.0 GHz (b) Re(ϵ_r): f = 3.5 GHz (c) Re(ϵ_r): f = 4.0 GHz

(d) Re(ϵ_r): f = 4.5 GHz (e) Re(ϵ_r): f = 5.0 GHz (f) Re(ϵ_r): multi f

(g) Im(ϵ_r): f = 3.0 GHz (h) Im(ϵ_r): f = 3.5 GHz (i) Im(ϵ_r): f = 4.0 GHz

(j) Im(ϵ_r): f = 4.5 GHz (k) Im(ϵ_r): f = 5.0 GHz (l) Im(ϵ_r): multi f

Figure 6.13: Reconstructed real, (a)-(f), and imaginary, (g)-(l), parts of the relative complex permittivity of the resolution test object with separation of 4 mm, at 3.0 GHz [(a) and (g)], 3.5 GHz [(b) and (h)], 4.0 GHz [(c) and (i)], 4.5 GHz [(d) and (j)], 5.0 GHz [(e) and (k)], and multiple frequency inversion [(f) and (l)], respectively.

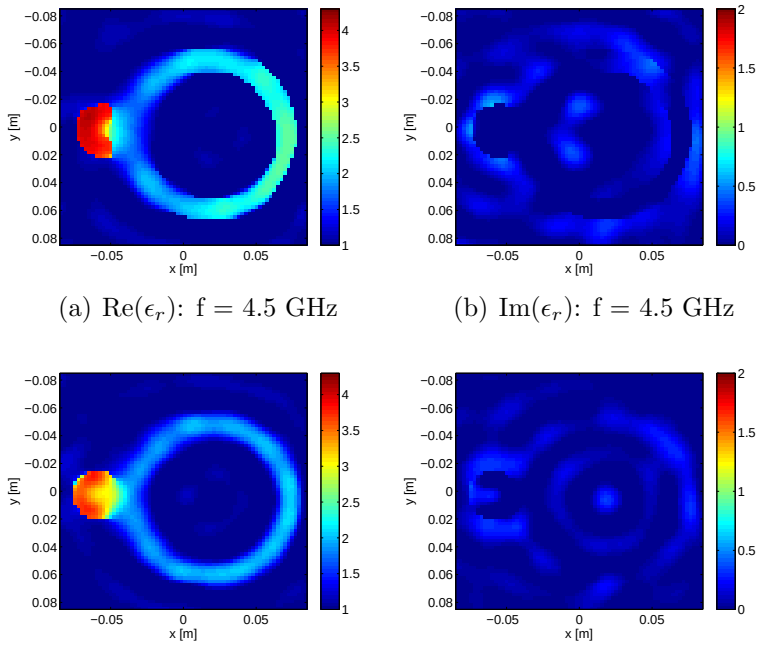

(a) Re(ϵ_r): f = 4.5 GHz

(b) Im(ϵ_r): f = 4.5 GHz

(c) Re(ϵ_r): multiple f

(d) Im(ϵ_r): multiple f

Figure 6.14: Reconstructed real and imaginary parts of the relative complex permittivity of the combination test object at 4.5 GHz, (a) and (b), and multiple frequency inversion, (c) and (d).

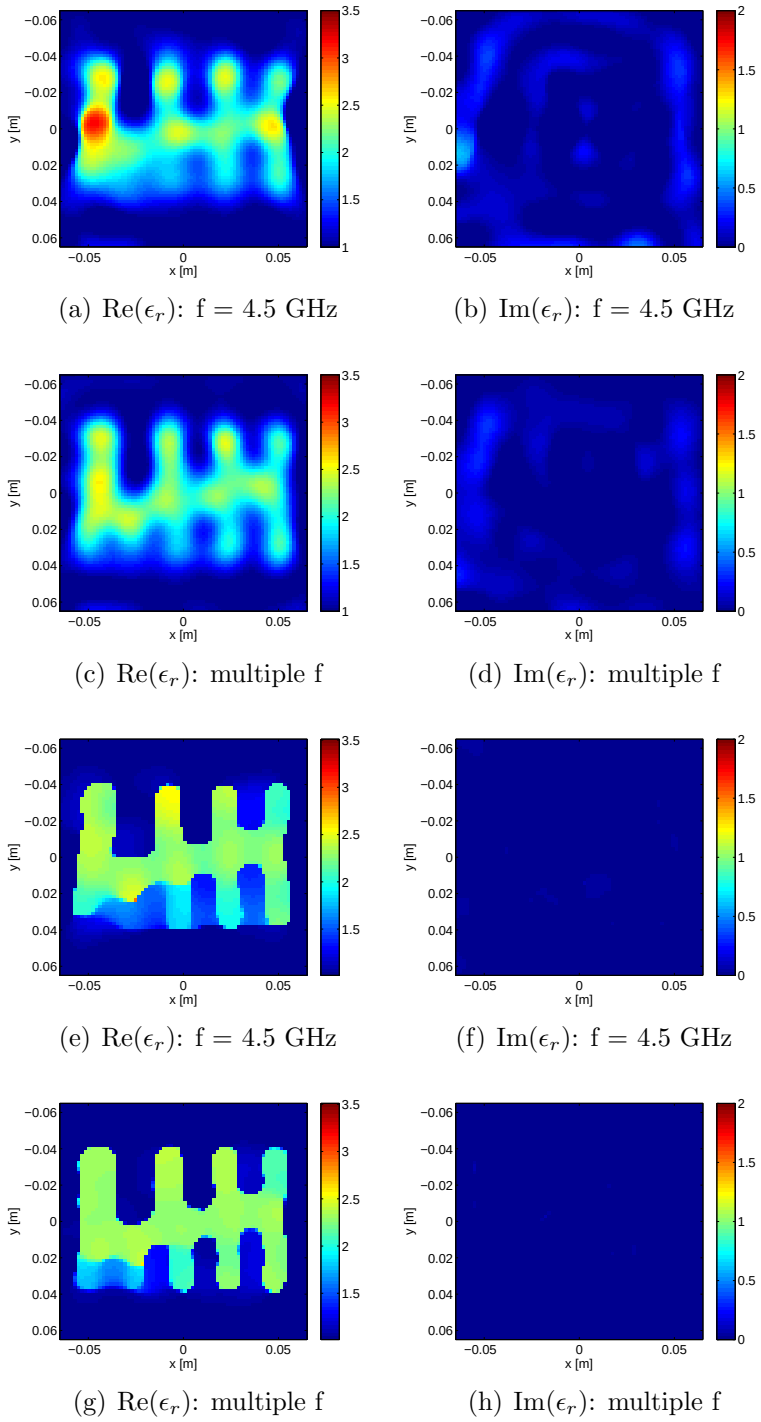

(a) Re(ϵ_r): f = 4.5 GHz (b) Im(ϵ_r): f = 4.5 GHz

(c) Re(ϵ_r): multiple f (d) Im(ϵ_r): multiple f

(e) Re(ϵ_r): f = 4.5 GHz (f) Im(ϵ_r): f = 4.5 GHz

(g) Re(ϵ_r): multiple f (h) Im(ϵ_r): multiple f

Figure 6.15: Reconstructed real and imaginary parts of the relative complex permittivity of the complexity test object at 4.5 GHz, and multiple frequency inversion. (a)-(d) Measured data, (e)-(h) synthetic data.

probes with various relative separations. It is shown that the probe data can be used for image reconstruction even if the probe-collector interaction changes significantly. In order to evaluate the probe data, the scattered fields of each system are also directly collected *e.g.* where the probes have not been used for the measurement. Four OIs are used to test these systems. Reconstructed real and imaginary parts of the dielectric properties are presented and the advantage of using extra probes are illustrated.

6.6.1 Description of Non-Uniform MWT System

A picture of the non-uniform measurement system is shown in Figure 6.16 (a). Once a Tx DLVA is illuminating the microwave signal, the probes are successively activated. The rest of probes are kept *opened*. In this experiment, some probes are attached to the DLVAs and the other probes are held by an Acrylic rod, 1.5 cm diameter and 10.0 cm long, see Figure 6.16 (b).

6.6.2 Near-Field of a DLVA

The near field E_z radiation of a single DLVA and the location of side and front probes are illustrated in Figure 6.17. The antenna's symmetrical radiation pattern is directive towards the end-fire direction as discussed in Chapter 3. The E_z field at the left and right probes' location are equal, however it is significantly lower than that at the front probe. Therefore, the DLVA-probe interaction for the side probes is the same but it is different from the front probe.

6.6.3 Measurement Systems

Five measurement systems were designed with 6 or 12 Tx DLVAs, including no-probe and probe-based systems. "Rx" and "probe" indicate the type of the receiving

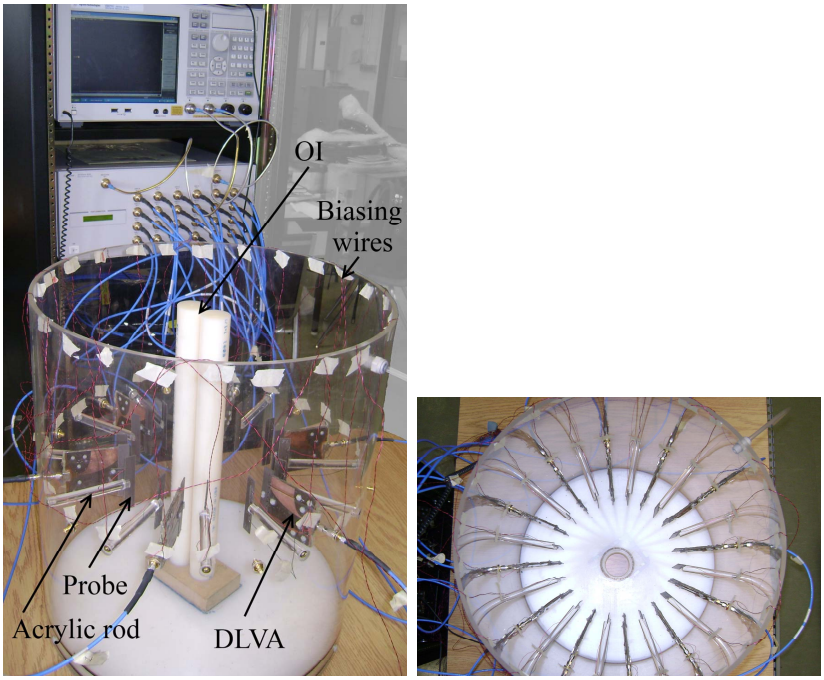

(a) (b)

Figure 6.16: (a) MWT measurement system with 6 collectors and 12 probes, (b) -top-view of 12 collectors and 24 probes setup.

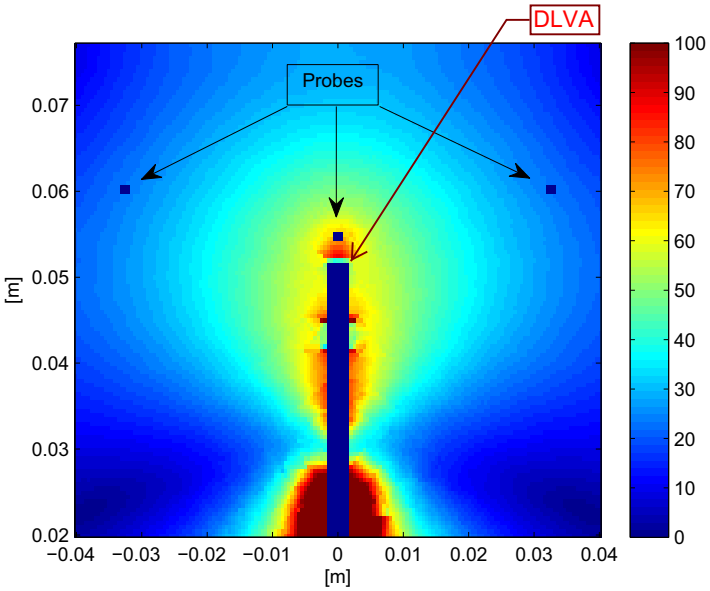

Figure 6.17: E_z near-field radiation of a single DLVA at 3.5 GHz (V/m). The dark blue rectangle represents the DLVA.

method used in these systems. “Rx” corresponds to a direct measurement system. In the probe-based systems, because the probes are located at different positions with respect to their corresponding collector, the probe-collector interaction changes for different probe-collector pairs. By presenting the imaging results of the two systems, using “Rx” or using “probe”, one is able to determine whether or not the probe data is useful for reconstruction. Due to the use of different numbers of probe and antennas, the size of the collected datasets are not same, and a variety of different OIs are utilized for testing the image reconstruction ability.

Figure 6.18 (a) shows a system with 6 DLVAs. Data is collected using the 6 Tx DLVAs and 5 Rx DLVAs for each Tx. Again, note that probes are not used in this system. The acquired dataset is $6\times5 = 30$.

Figure 6.18 (b) shows a system with 6 DLVAs and 10 probes. Each DLVA is used as a Tx with 5 collector DLVAs which collect the fields from their corresponding left and right probes. In this implementation, the probes are located symmetrically with respect to their collector. The probe-collector interaction is the same for both probes. The dataset is $6\times10 = 60$.

Figure 6.18 (c) shows a similar system with 6 DLVAs and 24 probes. Again, for each of the 6 Tx DLVAs there are 5 collector DLVAs which collect the fields from 4 corresponding probes: right, front, left and far-left (the one to the left side of the left probe). In this implementation, the probes-collector interaction change significantly. The dataset is $6\times20 = 120$.

In Figure 6.18 (d) the dataset size was increased by increasing the number of DLVAs up to 12. Here no probes are used and 11 Rx DLVAs collect the field for each Tx. The dataset is thus $12\times11 = 132$. The other option with this system is to use only 6 Tx DLVAs and 11 Rx DLVAs. The dataset would be $6\times11 = 66$ in this case.

Figure 6.18 (e) illustrates a system with 12 DLVAs and 24 probes. There are 11 collectors in this system for each Tx, each of which collects the field from its left and front probes. The dataset is 12×22 = 264.

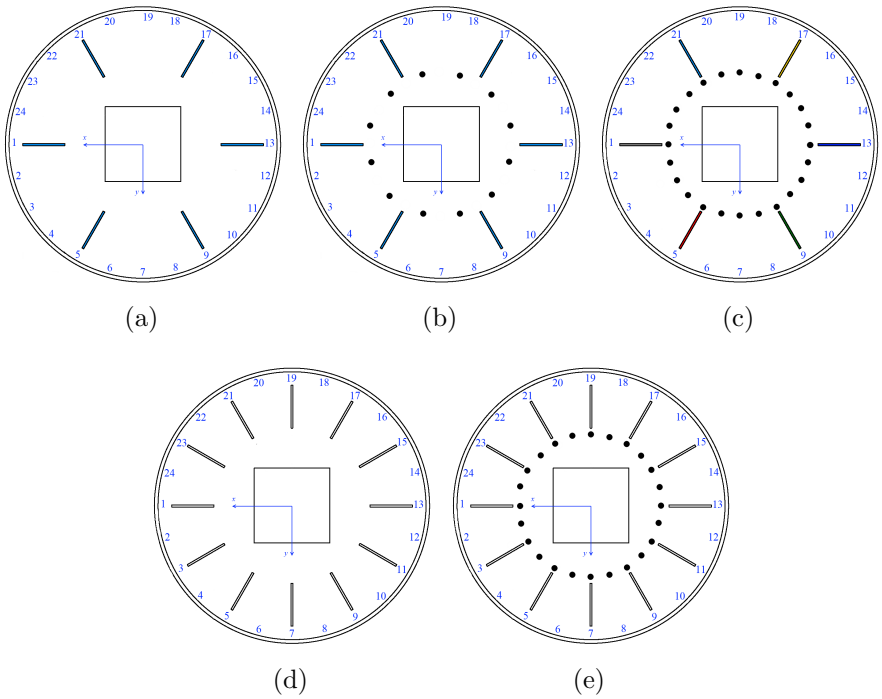

Figure 6.18: Block diagram of measurements:(a)6Tx-5Rx (b) 6Tx-10Probe (c) 6Tx-20Probe (d) 12Tx-11Rx or 6Tx-11Rx (e)12Tx-22Probe.

6.6.4 Objects for Imaging

The size of the collected datasets for the 5 systems is different. The more data that is collected, the more complicated OI that can be reconstructed. Figure 6.19 contains photos of the 4 different OIs which were used in this experiment. The reconstruction is performed at 3.5 GHz. In order to validate the results, the complex permittivity of each OI was measured, $\epsilon(\mathbf{r}) = \epsilon'(\mathbf{r}) - j\epsilon''(\mathbf{r})$, using the Agilent 85070E dielectric probe kit. The dimensions and measured ϵ are listed in Table 6.3. For the wood, the

permittivity is an average of measurements taken at the four faces.

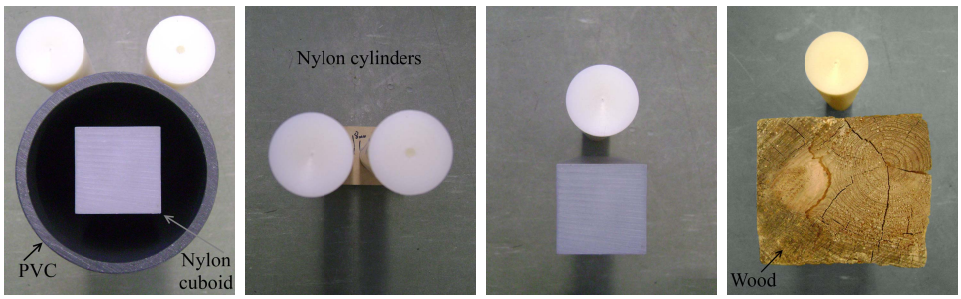

(a) (b) (c) (d)

Figure 6.19: The pictures of phantoms:(a)bear-face phantom (b) resolution test, 2 nylon rods separated by 8 mm (c) geometry test, nylon rod-cuboid (d) lossy OI test, wood-nylon rod.

Table 6.3: Measured permittivity at 3.5 GHz and dimensions of OIs (see Figure 6.19).

OI	**Dimension**	**Permittivity**
Nylon rod	Diameter $D = 3.8$ cm	$2.64 + j0.02$
Nylon cuboid	5.0×5.0 cm	$2.57 + j0.04$
PVC	$D_{in}, D_{out} = 10.2, 13.0$ cm	$2.20 + j0.01$
Wood	10.0×9.5 cm	$2.52 + j0.17$

6.6.5 Inversion Algorithm and Calibration

Similar to the previous MST system, the MR-GNI algorithm is utilized to reconstruct the permittivity images. The imaging domain D is discretized into $N \times N$ square pixels, here $N = 70$. Using the measured E_z by either the Rx DLVAs (in the framework of the *direct* method) or the probes, the contrast function $\chi(\mathbf{r})$ is calculated.

The collected scattered fields are calibrated to the scattered fields by a PEC cylinder, 3.5 inch diameter, as described previously. The calibration factor for each probe is defined separately and it is the ratio of the analytical to the measured scattered

field at each probe location. Herein, the probe-collector interaction is changing, thus a separate calibration factor for each probe was used, see (6.1).

6.6.6 Imaging Results using Non-Uniform System

In this section, the reconstructed images of different OIs are presented. In the first test, the results of the 6 DLVA system are presented once using 5 Rx DLVAs and once using 10 symmetrical probes on the left and right of each collector (Figure 6.18 (a) and (b)). Due to the small amount of information, only the simplest OI, the resolution test: Figure 6.19 (b), was imaged. For other OIs, the reconstructed image does not show any meaningful result. These images are depicted in Figure 6.20.

In the second test the results of the 12 DLVA system are presented once using 11 Rx DLVAs and once using 22 asymmetrical probes on the left and front of each collector (Figure 6.18 (d) and (e)). The dataset is large enough for imaging a complicated OI, the bear-face phantom: Figure 6.19 (a). The imaging results are depicted in Figure 6.21. Also lossy object of wood-Nylon was tried in this configuration (Figure 6.19 (d)) and its images are shown in Figure 6.22.

In the third test, the systems with similarly sized datasets were used for data collection where the data was collected by either Rx or probe. Once the 12 DLVA system was used with 6 Tx and 11 Rx DLVAs as shown in Figure 6.18 (d). Then the 6 DLVA system was used with 6 Tx and 10 Probes as shown in Figure 6.18 (b). These two experiments provide 66-point and 60-point datasets, respectively which are almost equal. The OI for this test is the resolution test (Figure 6.19 (b)) and the nylon rod-cuboid (Figure 6.19 (c)). The imaging results of these two OIs are shown in Figure 6.24 and Figure 6.23, respectively.

Finally the probe system with different number of probes was used. For this

experiment, the nylon rod-cuboid phantom, Figure 6.19 (c), was utilized as an OI. The images of the 6Tx-10Probe system are presented in Figure 6.18 (b), with the one obtained from the 6Tx-20Probe system, Figure 6.18 (d). The results are shown in Figure 6.25.

These reconstructions use data obtained from direct (Rx) and indirect (using probes) measurement systems having a varying probe/collector interaction distance. The calibration of each dataset is necessary. By increasing the number of data points, reconstruction of more complicated OIs was possible (the object is visible within the reconstructed image).

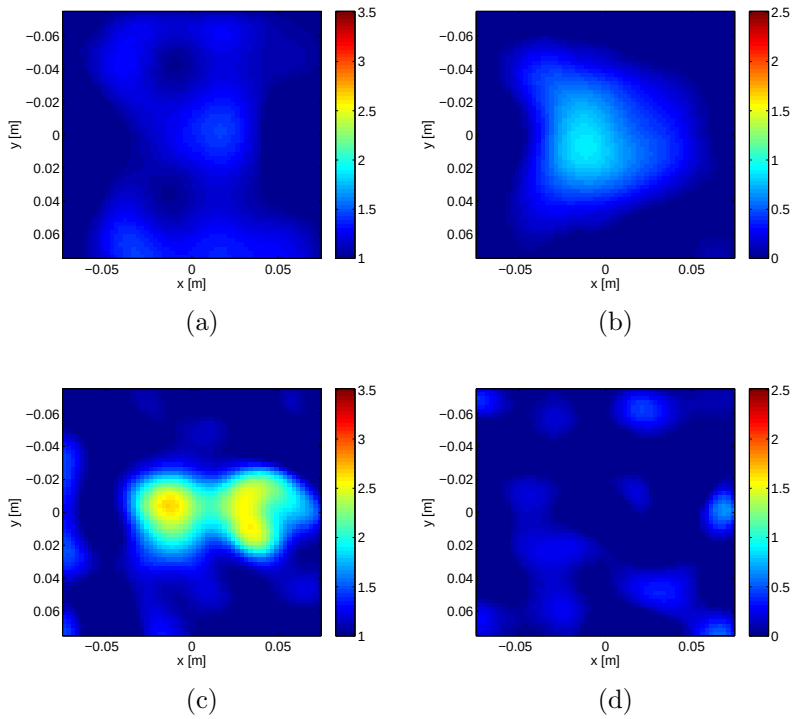

Figure 6.20: Reconstructed Re(ϵ) (left) and Im(ϵ) (right) of 2-nylon rods at 3.5 GHz. (a),(b): 6Tx-5Rx, (c),(d): 6Tx-10Probe.

From the reconstruction results presented in this section, it was made clear that the non-uniform distribution of probes with respect to the collectors can image differ-

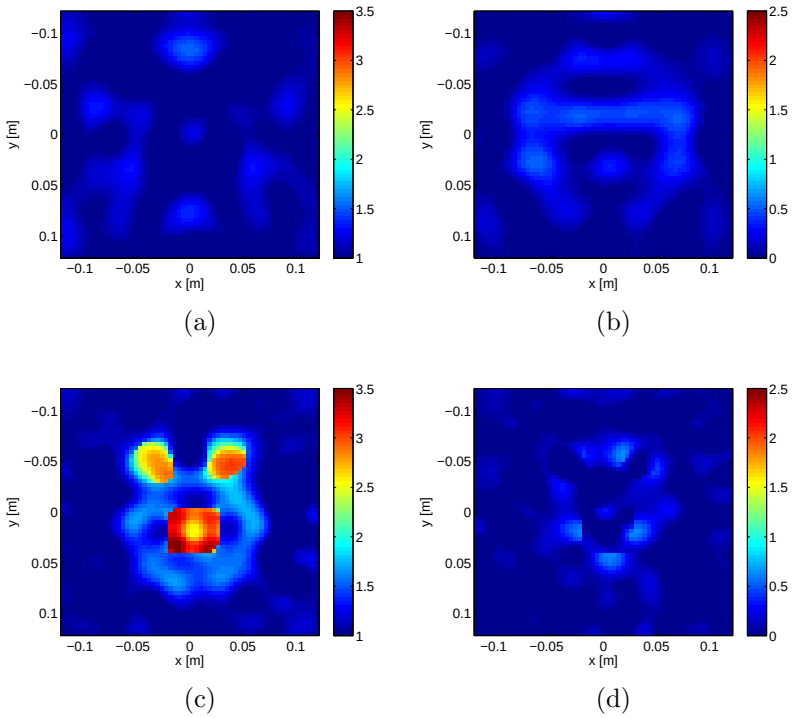

Figure 6.21: Reconstructed Re(ϵ) (left) and Im(ϵ) (right) of the bear-face phantom. (a),(b): 12Tx-11Rx, (c),(d): 12Tx-22Probe.

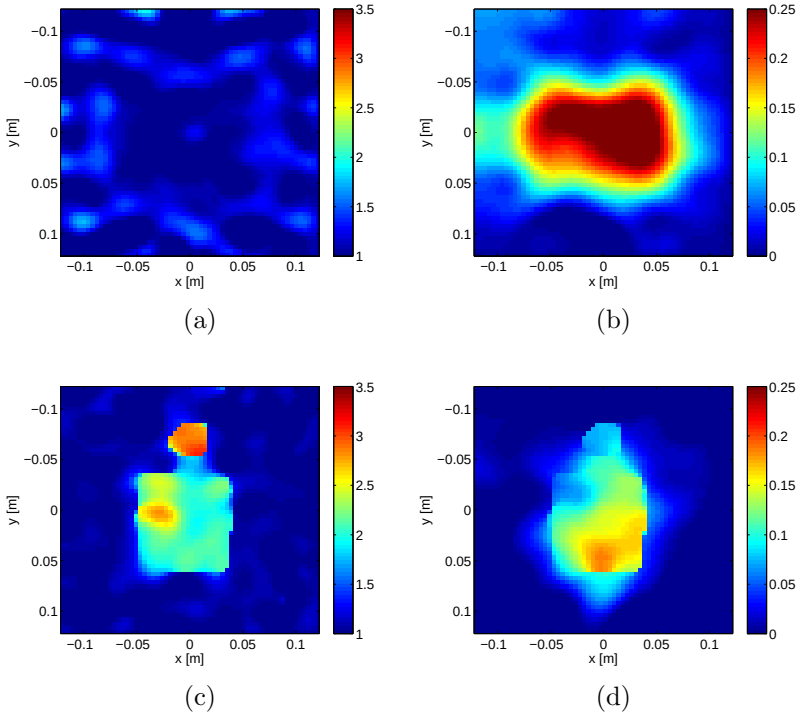

Figure 6.22: Reconstructed Re(ϵ) (left) and Im(ϵ) (right) of the wood-Nylon phantom. (a),(b): 12Tx-11Rx, (c),(d): 12Tx-22Probe.

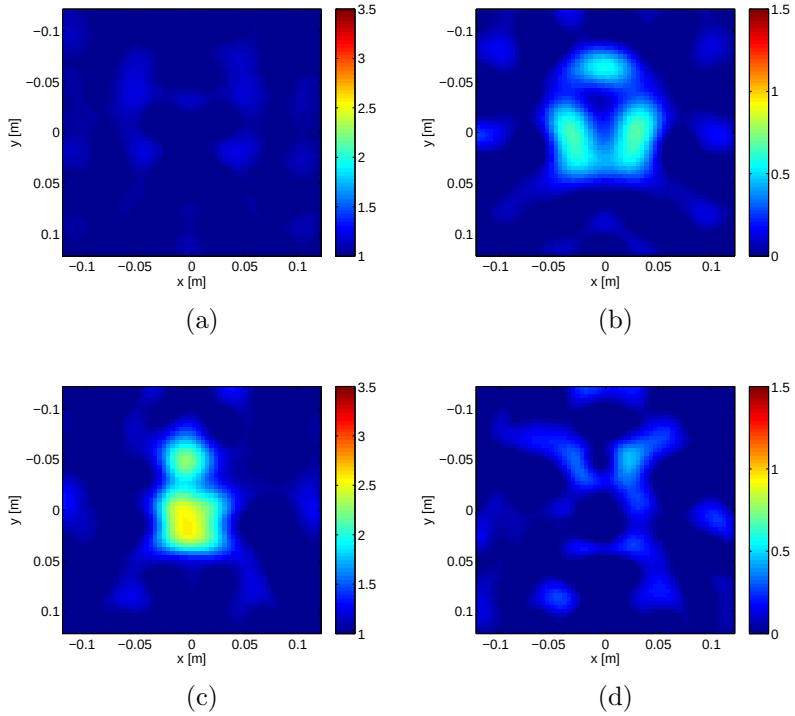

Figure 6.23: Reconstructed Re(ϵ) (left) and Im(ϵ) (right) of the Nylon rod-cuboid phantom. (a),(b): 6Tx-11Rx, (c),(d): 6Tx-10Probe.

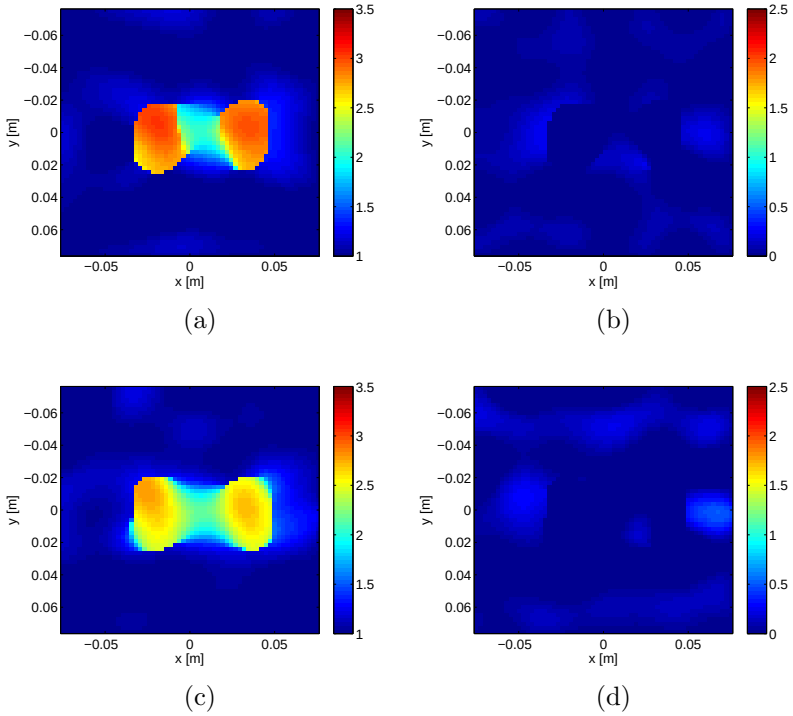

Figure 6.24: Reconstructed Re(ϵ) (left) and Im(ϵ) (right) of the 2-Nylon rods. (a),(b): 6Tx-11Rx, (c),(d): 6Tx-10Probe.

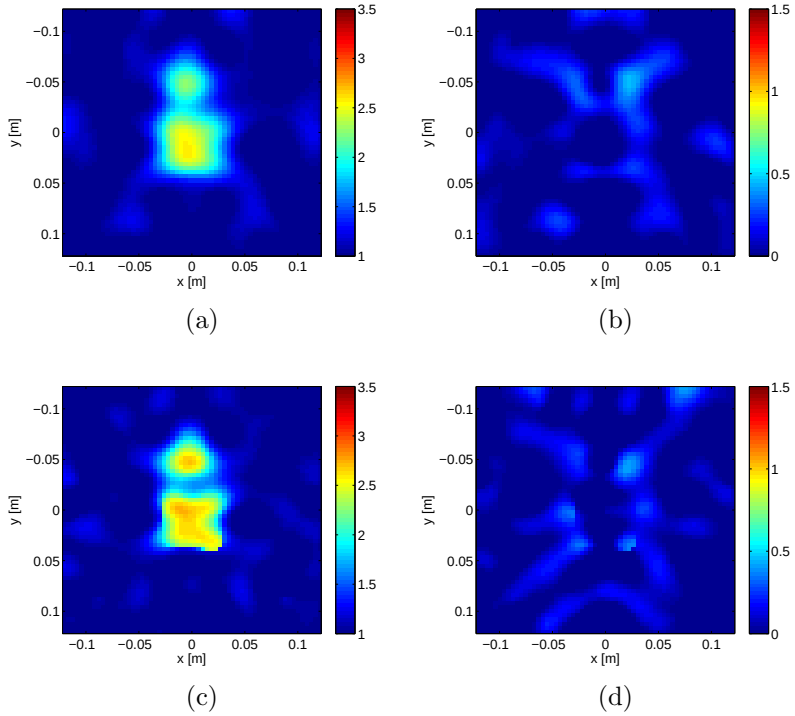

Figure 6.25: Reconstructed Re(ϵ) (left) and Im(ϵ) (right) of the Nylon rod-cuboid phantom. (a),(b): 6Tx-10Probe, (c),(d): 6Tx-20Probe.

ent objects. Although the distance of probe-collector and their interaction is varying in such system, the extra amount of data generated by these probes is critical for image reconstruction. For example from the results of Figure 6.20, one can see that the image reconstruction of 6Tx-5Rx system, ((a),(b)), fails and the image does not have any information but the the image from the 6Tx-10Probe system, ((c),(d)), shows the OI. Note that these two systems use equal number of antennas for measurement (6 DLVAs). Similar results obtained for reconstruction of a more complicated phantom, the bear-face, shown in Figure 6.21. In both cases only 12 antennas are used for measurement. The 12Tx-11Rx, (Figure 6.21 (a),(b)), system fails in image reconstruction while the 12Tx-22Probe system, (Figure 6.21 (c),(d)), can reconstruct the OI and the one can see the bear face. Similar results for wood-Nylon phantom was observed that are shown in Figure 6.22. In these three experiments, the extra probes, introduce more data points for image reconstruction.

Also the systems with relatively similar sized datasets were tested that use probes or Rx. Datasets of 6Tx-11Rx and 6Tx-10Probes were used for image reconstruction of either the resolution test (Figure 6.19 (b)) or the nylon rod-cuboid test (Figure 6.19 (c)). Their image reconstruction is depicted in Figure 6.24 and Figure 6.23, respectively. 6Tx-10Probe system has lower amount of data compared to 6Tx-11Rx system, however the image reconstruction for nylon rod-cuboid OI fails in the 6Tx-11Rx system while it is visible in the 6Tx-10Probe system, see Figure 6.23. These results were not observed for resolution test images, shown in Figure 6.24. Again, it is shown that the probe data can be used for image reconstruction, but if they provide any advantage needs careful error analysis for different results.

Finally, the systems with different number of probes were studied. The nylon rod-cuboid in a 6 DLVA system was used where the number of probes increased from 10

to 20. The imaging results of this measurement is shown in Figure 6.25 and one can see that the object is clearly resolved for the 6Tx-20Probe, compared to 6Tx,10Probe system. Thus, increasing the number of probes, improves the image reconstruction to some extent.

6.7 Summary and Discussion

The configuration of the "air-based" MWT system introduces two major sources of measurement error: instrumentation error, and polarization error. The polarization error is due to the antennas not being able to differentiate between different polarizations of field within the chamber whereas instrumentation error is introduced by the measurement system being used.

In the experimental system the antennas remain stationary and thus, the polarization error remains constant throughout the measurements. Instrumentation error is a function of several factors which may be time-varying: room temperature, imperfection in the cables being used which may vary due to cable movement, and VNA calibration errors between measurements.

In the direct measurement system (no probe), the time difference between different data collections, introduces a time-varying instrumentation error that mostly is due to the cables. This is because the cables are not necessarily stationary and their stress and bending may change in time. Reducing this error requires repeating the incident-field and the calibration measurements for each data collection. As mentioned earlier, the incident-field and calibration measurements are required by the inversion algorithm.

In the system being proposed, every field measurement is performed twice by repeating the S_{21} measurement, when the probes are open and when they are closed.

The two measurements are performed within a short period of each other during which it is assumed that the cables remain unchanged. This applies to the incident field, total field and the PEC cylinder calibration measurements. Due to the collection of differential signals at each measurement, the cable errors almost vanish. Having said that, there is no need to repeat the incident field or the PEC measurement for each OI, since the new system is less sensitive to instrumentation error and the error due to the cables. This is one of the advantages of this system.

One disadvantage of the direct measurement system is the limitation of the number of possible measurement locations. In such a system an increase in measurement locations requires the presence of more co-resident antennas. This increases mutual coupling, especially in a air-based environment such as the one considered herein. Furthermore, adding more antennas to the co-resident array requires the use of more expensive RF switches. On the other hand, using fewer antennas reduces the number of field sampling points. One of the advantages of the proposed system is its potential for decreasing the number of antennas and increasing the number of probes, thereby increasing the number of field sampling points.

In the proposed MST technique, the simple scattering probes are the primary measurement devices that surround the OI and are impedance-modulated successively to collect the field. The DLVAs produce the initial field and are only a secondary receiving device. Due to the use of the differential measurement, the instrumentation error is reduced. In addition, since the cable error is removed, it is possible to rotate parts of the measurement system in order to collect more data. Moreover, it is not needed to repeat the incident and calibration measurement even if there is a long time gap between measurements. As long as the position of antennas and probes inside the chamber remains unchanged, the incident and calibration measurements

are valid. This is an advantage for possibly future clinical systems. For the image reconstructions presented here, the datasets were collected over an interval of several days without repeating the incident or the calibration measurement. The cables were moved during this period.

For future study, because this system has the ability to measure (infer) any field at a scattering-probe site, it can also be used with an "incident field" type calibration, as opposed to the scattered-field calibration described herein. There may be advantages to such a calibration technique. In terms of increasing the number of probing locations, because the proposed technique is less expensive to implement, the use of more scattering probes per antenna/collector was investigated. It was shown that in spite of significant difference of probe-collector interaction, the probes data in a non-uniform system can be used for image reconstruction. It was shown that for some OIs, a direct system with equal number of antennas compared to the proposed system, is not able to reconstruct images, however, introducing more probes generates useful information which results in a successful image reconstruction.

Comparing the direct and indirect methods, one can benefit from the advantages of both methods. Averaging did not show any improvement. The MR-GNI algorithm was used to successfully reconstruct images of different objects.

6.8 Conclusion

A novel measurement system based on the MST technique was introduced. In this system, measurements were performed in the near field region using a primary array of scattering probes in front of a secondary array of receiving antennas. Prior to this system, a direct measurement system with 24 DLVA was developed, see Chapter 3. Compared to the direct system, the probes can measure the E_z component at

the receiving stations very accurately. As discussed in chapter 3, in an experimental tomography system different field polarizations exist. Even by illuminating the OI by a single polarized incident field, the scattered field may have all field polarizations, depending on the OI. The cross-polarization component of the Tx antennas may generate unwanted E_z component. Furthermore, the co-polarization component of the Tx antennas may generate a cross-polarization component at the receiver antennas. In a direct system, all these components contribute in the received voltage by the Rx antenna and generate the polarization error. Using the probes, an accurate single polarized field measurement is possible at the receiver stations that reduces the polarization error. However, in order to reduce the error due to the Tx antenna, an antenna with zero or negligible cross polarization must be used (here a DLVA has been utilized). There are other sources of error *e.g.* resulting from 2D modeling of a 3D wave propagation phenomenon. Calibration techniques can be developed specifically to minimize some of these specific errors. Some of these techniques were discussed in chapter 4. Measuring the field in two orthogonal polarizations and combining TE-TM in the inverse algorithm can further reduce the polarization error.

In order to test the feasibility of the proposed system, for the first implementation, a minimum number of scattering probes (equal to number of DLVAs) were incorporated into the system. For MST implementation, each scattering-probe was opened and closed, by biasing the PIN diodes positioned in series along the probe. A careful analysis of the system was performed for choosing the optimum biasing route.

The sensitivity of the probe was measured by decreasing the VNA output power. Using the MR-GNI inversion algorithm, successful images of different objects, were reconstructed.

The proposed system features a number of advantages: incident-field and calibra-

tion measurements are performed only once. The system reduces instrumentation error as well as measurement errors due to the cables. Moreover, it is possible to increase the number of probes, without a need for RF switches, in order to collect more data.

A non-uniform implementation of this system was also presented where the data was collected using more than one scattering probes for each collector. It was shown that the probe data is useful and, in some cases critical, for image reconstruction.

Chapter 7

Conclusions and Future Work

> *We really haven't got any great amount of data on the subject, and without data how can we reach any definite conclusions?* (Thomas A. Edison [92])

In this chapter, the main results of this thesis are summarized. Then possible future directions are outlined.

7.1 Conclusions

The main contribution of the research described in this dissertation was the development of novel MWT systems. One of the most important design factors in developing an MWT system is to measure a substantial amount of electromagnetic scattering data to ensure a robust and quantitatively accurate inversion. This is usually performed by utilizing co-resident antennas, which are located at specific measurement sites. In this method, referred to as the *direct* method, the number of antenna elements used in existing MWT systems varies, for example 16 [6], 24 [70,72] or 64 [48] antennas. Unfortunately, the need for a high density of measurement points is in direct conflict with another important design consideration: the adequate spatial separation of antennas so as to minimize the mutual coupling. Thus, in the *direct* method, the number of antenna elements is usually determined by balancing these two important design factors.

This thesis provides different antenna designs used for an air-based direct system. In other direct systems, the background is a lossy medium thus, they can be approximated as homogeneous system of infinite extent; calibration in such systems is relatively simple. The calibration and modeling error of the direct system were investigated and image reconstructions of dielectric phantoms were obtained.

One way to increase the number of measurement points without significant increase in mutual coupling is to use near-field probes, where the fields are measured indirectly based on the MST. The near-field measurement techniques were reviewed as well as the MST standard implementation techniques for imaging applications.

The direct and indirect methods were also combined to show the feasibility of using multiple collectors in the framework of MST. Having multiple collectors enables this system to have full circular scanning capability at even intervals of 15° in a circular array [89]. In this system, 24 collectors were utilized; each of which was a DLVA equipped with a printed-wire as the probe. Instead of modulation and using coherent detectors, the collectors were connected to a VNA through a switch network. By activating individual probes, successively, the MST signals were collected. However, in this system the number of the probes and the collectors were equal, each collector corresponding to one probe, and the probe-collector distance remained unchanged. The performance of systems with a non-uniform distribution of scatterer probes and collectors was also studied.

The number of collectors was then reduced while the number of probes was changed to be equal or greater than the collectors. Several systems were implemented where each collector interacts with from 2 to 4 probes with various relative separations. It was shown that the probe data can be used for image reconstruction even if the probe-collector interaction changes significantly. In order to evaluate the

usefulness of the probe data, the scattered fields of each system were also *directly* collected, where the probes were not used for the measurement. Due to the different sizes of the datasets, 4 OIs were used to test these systems. The larger datasets were required to image the more complex OI. Reconstructed real and imaginary parts of the OI dielectric properties were presented and the advantage of using extra probes were illustrated.

7.2 Future Work

One unique feature of MWT compared to other imaging modalities such as X-ray and ultra-sound is the use of information carried by the polarization of interrogating fields. Current MWT systems in existence do not take advantage of this feature and throughout this work, the preliminary investigation of using probes for specific polarization collection was accomplished . As pointed out in Chapter 2, the proposed tomography system collects only one field component, E_z. In a near-field system one great challenge is to obtain all polarizations and this is feasible using the scatterer probe technique. One important direction for future work is to collect different polarizations using the scatterer probe technique.

Currently, MWT systems are implemented assuming a 2D approximation. In order to reconstruct a 3D image of an object using such systems, one needs to change the cross-section of the OI being imaged in the system. This requires a long data acquisition time. Using the scatterer probes, 3D imaging can be achieved by implementing a distribution of probes over a 3D surface of measurement locations.

The proposed MST is utilizing a VNA to capture the change in each activated probe using the collector antenna. Current indication of this system is that the probe cannot be located very far from the collector. The farthest distance implemented in

this work was the probe next to the neighboring probe (left or right) of the collector within 30°. One direction for future work is to employ a coherent detector instead of the VNA and modulate the probe at a low frequency.

In the scatterer probe system proposed here, 5 PIN diodes were utilized to reduce the interference of passive probes, but still some interference exists. In future one may use optical fibers for modulating the probes. Introduction of optical fibers does not interfere substantially with the integrating microwave fields.

For the non-uniform scatterer probe system the same calibration approach as the uniform system was used. In future weighted coefficients for probes at farther distances from the collector can be introduced. This task should be simple to implement in the inversion algorithm, but the actual weights to use, requires further research.

Currently the MST system uses air as the background medium which is not an appropriate background for biological objects. A system with high permittivity background medium is required for biomedical applications.

A study to investigate the probe design and optimize system performance to archive the highest sensitivity during the MST procedure is also required. This goal could be achieved by utilizing other probe and probe array geometries that satisfies different polarizations as well as a wide frequency range.

The current measurement system is designed for objects that fit inside the chamber and might be suitable for biological objects. One can also investigate the MWT systems for non-destructive testing in industrial applications. For such applications, the antenna locations should change to meet the imaging environment physical constraints.

Appendix A

Phantoms and Dielectric Measurement

Complex permittivity (equation (2.5)) measurement of biological tissues is particularly important due to the different aspects of electromagnetic interaction with human body at various frequencies. Health hazard due to some microwave radiations such as cell phones, therapeutic applications of microwave, and microwave imaging are some of the existing interests to study the dielectric properties of the tissues, and to make phantoms to be used for research. Biological tissues are usually very dispersive at microwave frequencies and this is due to their water content and dipolar absorption.

Permittivity of dispersive materials depends on frequency and it is possible to mathematically model this behavior by a well-known first order (single pole) Debye model:

$$\epsilon = \epsilon' - j\epsilon'' = \epsilon_\infty + \frac{\epsilon_s - \epsilon_\infty}{1 + j\omega\tau} \tag{A.1}$$

where ϵ_s and ϵ_∞ are the static and optical (very high microwave frequency) dielectric constant and τ is the relaxation time or the time constant of the first order system. Because single time constant cannot predict dielectric behavior of most materials, different distribution functions are introduced in literature [93].

The dielectric properties of biological tissues have been investigated by a number of researchers. Some early and highly cited publications provided information for permittivity and conductivity of different human body tissues, over a wide frequency

range [94,95] and [96]. Of particular interest, for the breast tissue and breast cancer, there had been a limited number of reports. Early studies, showed that there is a contrast ratio of 5 to 10 between normal and malignant tissues [6] and this was the general assumption until 2007, that in a joint research conducted by the University of Wisconsin and the University of Calgary, a large scale study was performed to measure the dielectric properties of breast tissues including normal, malignant and benign tumors [97, 98]. In this study, tissue composition was quantified in terms of the percentage of adipose, fibroconnective and glandular tissues. They showed that the dielectric properties of breast tissue are primarily determined by the adipose and water content of each tissue sample. It was concluded that the secondary factors such as patient's age, tissue temperature and time between excision and measurement had only negligible effects on the observed dielectric properties. Based on their observations, the difference between the normal adipose tissue and the cancerous tissue was large with up to a 10:1 contrast ratio, while the contrast between the malignant and the normal fibroconnective/glandular breast tissues was considerably lower, no more than approximately 10%. Although this large scale study was very useful to investigate some facts about breast tissue and it almost changed the direction of research especially on breast cancer detection, recent studies show that these results are not accurate enough to be generalized for breast tissue. All the measurements of this study were *ex vivo* and there was a delay of 5 to 50 minutes between the tissue removal and its measurement. Further investigation by Dartmouth Medical Center [99], showed that the amount of blood changes in tissues after being excised, significantly affects the dielectric properties. They measured the *in vivo* dielectric properties of 6 women for their study.

A.1 Tissue Phantoms

Phantoms for brain, muscle, bones, adipose, and glandular breast tissues have been proposed for ultrasound to microwave frequencies [100–104].

For the breast tissue, traditionally, phantoms that closely mimic the physical properties of breast tissues have been invaluable for the development and testing of medical imaging modalities. Many different tissue-mimicking phantom materials have been developed to simulate the properties of high- and low-water-content biological tissues at discrete frequencies. Most of these methods are reviewed in [102]. However, none of these phantoms include the heterogeneity and dispersive properties of a real human breast.

Gelatin-based materials are attractive to be used in biological phantoms due to their stable mechanical properties and ease of fabrication. In [105] experiments are performed on a phantom made out of agar gel with varying concentrations of low dielectric solutions mixed with agar powder to control the relative permittivity. Agar is a gelling agent or thickener. The most convenient low-permittivity liquid was corn syrup with relative permittivity of $\epsilon_r = 13$ and conductivity of $\sigma = 0.2$ S/m at 900 MHz. Mixtures of corn syrup and water in varied proportions can be produced with ϵ_r ranging from 13 at the low end to 77 in liquid form. However, because the ability of agar to thicken degrades significantly at higher corn-syrup proportions, a practical lower bound on the permittivity of the gel is roughly $\epsilon_r = 35$ at 900 MHz. The recipe for this phantom material was 78% corn syrup, 21% water, and 1% agar, which produced a gel with $\epsilon_r = 35$ and $\sigma = 0.7$ S/m at 900 MHz. The gel was formed in a 1000-mL glass beaker heated to $120°C$ for 40 min in an autoclave. The electrical properties were measured by using an Agilent 85070B dielectric probe kit in conjunction with an Agilent 8753C Network Analyzer [105].

One of the simplest phantoms for MI was developed by [31] to represent bone and fatty tissue. They used Polyester resin with hardener, aluminum powder, and acetylene black to make the phantom. Three phantoms were made in cylindrical shape with diameters of 1.55, 2.51, 4.23 cm, and height of 18.23 cm.

A.1.1 Dielectric Measurement

There are different methods to measure dielectric properties. Sensitivity and accuracy of measurement, significantly depends on the frequency range and type of material. Some of these methods are free-space techniques, resonant cavity for different kinds of transmission lines, open resonators, open-ended transmission line, *etc.* [93].

In this research open-ended method was employed which uses coaxial probe and is commercially available by *e.g.* Agilent 85070 kit. This probe is compatible with most network analyzers. To achieve better accuracy of this probe, a sample with diameter greater than 20 mm and thickness greater than $20/\sqrt{\epsilon_r}$ mm is required.

To calibrate the probe, it is possible to use known standard references like traditional open, load and short termination but it is recommended to use a well defined liquids for calibrating these probes that its dielectric properties are known [93, 106]. Water, which is a major part of biological tissues, is one of the best references for calibration. Our measurement setup is shown in Figure A.1.

A.1.2 Phantom Design

To make a tissue mimicking phantom, a good understanding of dielectric properties of materials is important. As mentioned earlier in this appendix, measuring dielectric properties of biological tissues, both *in vivo* and *ex vivo*, has been the topic of many studies in the literature.

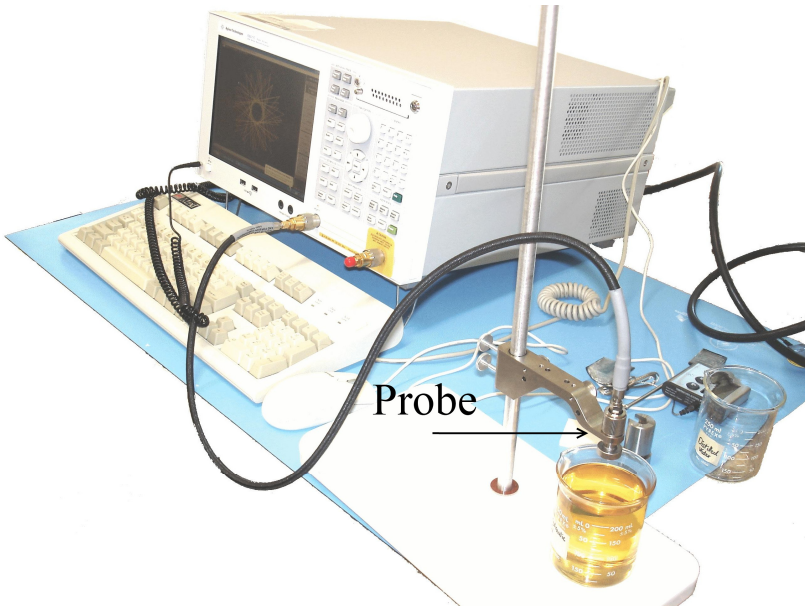

Figure A.1: Agilent 85070E dielectric measurement probe connected to VNA.

The linear combination materials does not necessarily generate a linear combination of their dielectric properties. This issue was investigated for several combination of water with other materials and the results are completely nonlinear. This is the most challenging part of making a phantom with specific characteristics.

Most breast phantoms developed for microwave imaging do not include the heterogeneity of the breast. In addition, they are mostly liquid and cannot be formed into different shapes. Herein, a procedure for fabricating a heterogeneous breast phantom is discussed. To make this phantom, widely available and non-toxic materials have been used. The steps are simple and phantom has elasticity similar to solids or gelatin [107].

A procedure given in [102] can be used to fabricate a breast phantom which is valid for wide frequency range. Oil and water are the main ingredients of this phantom. As suggested in [103], by increasing surfactant, emulsification improves and the resulting mixture is more uniform. Another procedure reported in [104] can provide a phantom

for heterogeneous ultrasound and MRI application.

For this study, based on [102, 103], and [104], we have developed a new procedure that provides more elasticity to build a heterogeneous phantom. The method is simple and fast. The resulting material has dielectric properties similar to the real breast tissues.

The phantom in [103] was proposed for MRI and ultrasound. We measured the dielectric properties at microwave frequency and found that it has a permittivity similar to fibroglandular tissue. The suggested phantom in [102] was modified to provide better elasticity and matching with the tissue properties. In summary, we replaced gelatin by agar and changed some of the preparation steps.

The following are the steps for the fibroglandular tissue [104]:

1. In a 1 liter (L) beaker at room temperature, add 42 grams (g) of propylene glycol and 675.5 mL of 18 megohm-cm double deionized water.

2. Slowly add, while stirring, 107.8 g of gelatin.

3. Cover the beaker with polyethylene food wrap and insert small hole in the top. Hold in place with a rubber band.

4. Place the beaker in a larger, metal or Pyrex container of hot water which in turn is placed on a heat source.

5. Heat the water until the gelatin mixture reaches 90oC and becomes transparent. Remove bubbles at the meniscus. This is the molten gelatin.

6. Remove the molten gelatin from the hot water bath and immerse partially in cold water bath.

7. As molten gelatin is cooling, heat 700 mL of safflower oil to $50°C$ in a 2 L beaker.

8. Add 700 mL of the 50oC molten gelatin to the $50°C$ safflower oil and mix vigorously with a table spoon that is bent at a right angle to minimize disturbances on the surface.

9. Add 7.7 mL of Ultra Ivory liquid surfactant (anionic and nonionic surfactants with no phosphate) and continue stirring until the emulsion is nearly white and a separation of oil does not occur when stirring is stopped.

10. Cool in cold water bath to $40°C$ and slowly add, while stirring, 5.292 g of formalin (37% formaldehyde solution).

11. Cool the emulsion to $\approx 34°C$ and pour into molds for further cooling and congealing. Congealing temperature is approximately $26°C$.

12. Cross-linking between formaldehyde and gelatin takes about 8 hours.

For skin, tumor and fat the procedure is as follows:

1. Mix oil and surfactant by the amount mentioned in Table A.1.

2. Mix formaldehyde and p-toluic acid in a separate beaker and shake it to get a uniform light blue solution.

3. Heat up the water and add oil-surfactant while stirring the solution.

4. Add formaldehyde-p-toluic acid to the solution and stir continuously.

5. Add agar pinch by pinch (1tbsp per time). Mix to make a uniform solution.

6. Add Alizarin to change the color for different parts of phantom.

7. Cover the main container of phantom material with non-stick cooking and baking paper. Make the partitions using different pipe sizes.

8. Pour the cooked materials into the container and put them in the fridge.

Table A.1: Material weight percentage for skin, fat, tumor, and glandular tissue.

	Skin	Fat	Tumor	Gland
Water	66.588	14.412	74.627	45.654
Oil	17.152	62.959	7.679	43.526
Surfactant	1.094	11.808	0.711	0.338
Formaldehyde	0.280	0.061	0.313	0.358
p-toluic acid	0.070	0.016	0.078	0
Agar	11.915	9.990	13.357	0
1-propanol	2.801	0.755	3.140	0
Alizarin	0.100	0	0.100	0
Propylene glycol	0	0	0	2.839
Gelatin	0	0	0	7.286

The dielectric properties of each tissue mimicking phantom were measured individually. A sample of each tissue was made in the form of a disk with minimum diameter of 10 cm and a thickness of 4 cm. One of the samples (skin) during measurement and glandular part of phantom are shown in Figure A.2 (a) and (b). The completed phantom is shown in Figure A.2 (c). To create the heterogeneous background, the fibroglandular phantom was shaped in different molds and was inserted inside the fat phantom. The measured dielectric properties of assembled phantom versus the Debye estimate of dielectric properties of real breast tissue are depicted in Figure A.3. In this figure, the upper region belongs to very dense fibroglandular tissue and malignant tumors. The low water content tissue phantoms, followed by the transitional region containing 31-84% fat are in the lower regions. The lowest region is for adipose or

fatty tissues. As shown in Figure A.3, the permittivity of the phantom follows the permittivity of the real breast tissues. While there is a good contrast between the conductivities of the various phantom materials, the measured conductivity has a different frequency response and is significantly higher than the real breast tissues. The Debye parameters for real breast were used from [108] and are shown in Table A.2.

(a) (b) (c)

Figure A.2: Photo of tissue phantom: (a) skin, (b) glandular tissue, and (c) breast phantom.

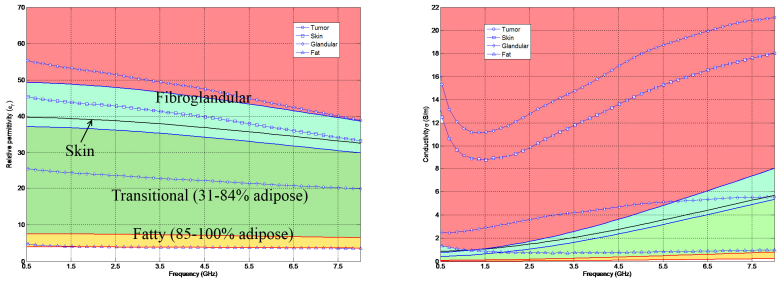

(a) (b)

Figure A.3: Relative permittivity and conductivity of phantom materials compared with the distribution of real tissue permittivity: (a) ϵ_r, (b) σ.

Table A.2: Debye parameters for real tissue [108].

	ϵ_∞	ϵ_s	σ_s (S/m)	τ_0 (psec)
Skin	15.93	39.76	0.83	13.00
Gland	13.81	49.36	0.738	13.00
Transitional	12.99	37.19	0.397	13.00
Fat upper	3.987	7.535	0.080	13.00
Fat lower	2.848	3.952	0.005	13.00

Appendix B

Time-Domain versus Frequency-Domain Measurement

The experimental MI systems can be implemented in time or frequency-domains. In a time-domain approach, a pulse generator is connected to the Tx antenna and an oscillioscope collectes the received signal of the Rx antenna. The frequency domain setup is implemented by the use of a VNA whose task is to record the scattering parameters between the two antennas.

Pulse generators and oscilloscopes typically have lower dynamic ranges than the network analyzer. There is no filtering at the input port of an oscilloscope while there are IF and resolution bandwidth filters at the entrance port of a network analyzer. For comparison, a 2-port Agilent 8363B PNA series network analyzer was employed. By using 10 Hz IF bandwidth, noise floor is less than -132 dBm at 500 MHz - 10 GHz frequency range. Knowing the maximum input power for receiver, which is -11 dBm, it provides a 120 dB dynamic range for measurement *.

On the other hand, a digital sampling oscilloscope, Tektronix TDS 8200, was employed. The detector module we used was 80E03 plug-ins which operate up to 20 GHz. Vertical sensitivity range of this module is 10 mV to 1.0 V in full scale † which corresponds to -27 dBm to 13 dBm with respect to 50 Ω reference. The noise floor

*Agilent Technologies technical note: PNA series network analyzers E8362B/C, E8363B/C, and E8364B/C technical specifications, 2008.

†Tektronix technical note: Technical specifications, DSA 8200, 2007.

for this module is 300 μV, corresponding to -57.45 dBm. This provides only 70 dB dynamic range for measurement. The oscilloscope performance can be improved by using digital filtering and data averaging techniques. This oscilloscope is a sampling oscilloscope and is capable of probing a train of incoming pulses. In practice, the pulse generator is not able to generate perfectly similar pulses at different times. Knowing this fact, and improving the trigger signal of oscilloscope by pulse generator, the incoming pulses to oscilloscope are not 100% the same. This means that the dynamic range cannot reach to the ones of a VNA. Moreover, the data averaging imcreases the data acquisition time.

For this reason, we chose a frequency-domain approach to implement our MWT systems.

Appendix C

Selected Publications Arisen from this Thesis

The contributions of this thesis have been refereed reviewed in different journal and conference publications. A selected list of these publications is as follows:

- **JP-I** [109]: Majid Ostadrahimi, Puyan Mojabi, Sima Noghanian, Joe LoVetri, and Lotfollah Shafai, "A multiprobe-per-collector modulated scatterer technique for microwave tomography," *Antennas and Wireless Propagation Letters, IEEE*, vol. 10, pp. 1445-1448, 2011.

  Abstract: Scattering probes with collector antennas can be utilized for microwave tomography (MWT) applications based on the modulated scatterer technique. Using this technique, we previously demonstrated a novel tomography system that utilizes a single printed-wire probe in front of each collector of a multicollector MWT system. Each collector is implemented as a multilayer Vivaldi antenna. In this letter, the number of collector antennas is reduced while maintaining the number of probes. This results in a nonuniform distribution of probes with respect to the collectors and requires special calibration techniques to infer the scattered-field at the probe location. The advantages of using such a configuration for MWT are investigated. Image reconstructions for a number of targets using data collected from this system are shown and compared to results obtained from data collected using a standard MWT system that uses only the Vivaldi antennas. It is shown that the new configuration successfully extracts useful data at the locations of the probes, resulting in good tomographic constructions.

- **JP-II** [110]: Majid Ostadrahimi, Puyan Mojabi, Colin Gilmore, Amer Zakaria, Sima Noghanian, Stephen Pistorius, and Joe LoVetri, "Analysis of incident field modeling and incident/scattered field calibration techniques in microwave tomography," *Antennas and Wireless Propagation Letters, IEEE*, vol. 10, pp. 900-903, 2011.

Abstract: Imaging with microwave tomography systems require both the incident field within the imaging domain as well as calibration factors which convert the collected data to corresponding data in the numerical model used for inversion. The numerical model makes various simplifying assumptions, *e.g.* 2D vs. 3D wave propagation, which the calibration coefficients are meant to take into account. For an air-based microwave tomography system, we study two types of calibration techniques: incident and scattered field calibration, combined with two different incident field models: a 2D line-source, and an incident field from full-wave 3D simulation of the tomography system. Although the 2D line-source approximation does not accurately model incident field in our system, the use of scattered field calibration with the 2D line-source provides similar or better images to incident and scattered field calibration with an accurate incident field. Thus, if scattered field calibration is used, a simple (but inaccurate) incident field is acceptable for our microwave tomography system. While not strictly generalizable, we expect our methodology to be applicable to most other microwave tomography systems.

- **JP-III** [111]: Majid Ostadrahimi, Sima Noghanian, and Lotfollah Shafai, "A novel antenna design technique using finite element method and transmission line theory," *Microwave and Optical Technology Letters*, vol. 54, no. 1, pp. 126-133, 2012.

  Abstract: A combination method is utilized to design Eagle feed Vivaldi antenna. The Antenna structure is discretized into arbitrary number of sections whose characteristic impedances and their corresponding dimensions are evaluated using transmission line theory and finite element method, respectively. The proposed antenna is compared with two classical designs, theoretically and experimentally.

- **JP-IV** [89]: Majid Ostadrahimi, Puyan Mojabi, Sima Noghanian, Lotfollah Shafai, Stephen Pistorius, and Joe LoVetri, "A novel microwave tomography system based on the scattering probe technique," *Instrumentation and Measurement, IEEE Transaction on*, accepted in June 2011.

  Abstract: In this paper, we introduce a novel microwave tomography system which utilizes twenty-four double layered Vivaldi antennas, each of which is equipped with a diode-loaded printed-wire probe. By biasing a probes diodes, the impedance of the probe is modified, allowing an indirect measurement of the electric field at the probes locations. Each printed-wire probe is loaded with five equally-spaced PIN diodes, in series. We show that the electric-field data collected in this way within the proposed tomography system can be used to reconstruct the dielectric properties of an object of interest. Reconstructions for various objects are shown. Although the results are still preliminary, sufficient

experimentation has been done to delineate the advantages of such an indirect method of collecting scattered-field data for tomographic imaging purposes.

- **JP-V** [70]: Colin Gilmore, Puyan Mojabi, Amer Zakaria, Majid Ostadrahimi, Cam Kaye, Sima Noghanian, Lotfollah Shafai, Stephen Pistorius, and Joe LoVetri, "A wideband microwave tomography system with a novel frequency selection procedure," *Biomedical Engineering, IEEE Transactions on*, vol. 57, pp. 894-904, 2010.

  Abstract: In this paper, we describe a 2-D wideband microwave imaging system intended for biomedical imaging. The system is capable of collecting data from 3 to 6 GHz, with 24 coresident antenna elements connected to a vector network analyzer via a 2×24 port matrix switch. As one of the major sources of error in the data collection process is a result of the strongly coupling 24 coresident antennas, we provide a novel method to avoid the frequencies where the coupling is large enough to prevent successful imaging. Through the use of two different nonlinear reconstruction schemes, which are an enhanced version of the distorted born iterative method and the multiplicative regularized contrast source inversion method, we show imaging results from dielectric phantoms in free space. The early inversion results show that with the frequency selection procedure applied, the system is capable of quantitatively reconstructing dielectric objects, and show that the use of the wideband data improves the inversion results over single-frequency data.

- **JP-VI** [65]: Majid Ostadrahimi, Sima Noghanian, Lotfollah Shafai, Amer Zakaria, Cam Kaye, and Joe LoVetri, "Investigating a double layer Vivaldi antenna design for fixed array field measurement," *International Journal of Ultra Wideband Communications and Systems*, vol. 1, no. 4, pp. 282-290, 2010.

  Abstract: Vivaldi antenna is widely known as a broadband antenna. In this paper, we investigate a modified Vivaldi antenna with improved cross polarization working in the ultra-wideband (UWB) frequency range (3.110.6 GHz) to be used as multiple probes for microwave tomography system. Our study includes investigation of radiation characteristics of the antenna, antenna design steps, fabrication sensitivity effects on the antenna performance and proposing and implementing a twenty-four antenna element system for fast data acquisition, including a novel method for frequency selection in microwave tomography applications. We also studied the fidelity parameter of the antennas inside the twenty-four element setup. The mutual coupling of adjacent elements, in spite of close proximity, is less than 17 dB and fidelity variations for the antennas located in front of transmitter are less than 10%.

- **CP-I** Puyan Mojabi, Colin Gilmore, Majid Ostadrahimi, Amer Zakaria, Ian Jeffrey, Joe LoVetri, Stephen Pistorius, and Lotfollah Shafai, "Reduction of

modeling error in microwave tomography: A review," *IEEE International Symposium on Antennas and Propagation and USNC/URSI National Radio Science Meeting,* Spokane, USA, July 2011.

- **CP-II** Majid Ostadrahimi, Puyan Mojabi, Sima Noghanian, Joe LoVetri, Stephen Pistorius, and Lotfollah Shafai, "On the feasibility of a novel microwave tomography system based on the scattering probe technique," *IEEE International Symposium on Antennas and Propagation and USNC/URSI National Radio Science Meeting,* Spokane, USA, July 2011.

- **CP-III** Colin Gilmore, Amer Zakaria, Puyan Mojabi, Majid Ostadrahimi, Stephen Pistorius, and Joe LoVetri, "A 2D near-field multi-static wideband microwave scattering repository for the testing of calibration and inversion algorithms," *IEEE International Symposium on Antennas and Propagation and USNC/URSI National Radio Science Meeting,* Spokane, USA, July 2011.

- **CP-IV** [112]: Colin Gilmore, Puyan Mojabi, Amer Zakaria, Majid Ostadrahimi, Cam Kaye, Sima Noghanian, Lotfollah Shafai, Stephen Pistorius and Joe LoVetri, "An ultra-wideband microwave tomography system: preliminary results," *IEEE Engineering in Medicine and Biology Society (EMBS)*, Minneapolis, Minnesota, USA, September, 2009.

  Abstract: We describe a 2D ultra-wideband microwave imaging system intended for biomedical imaging. The system is capable of collecting data from 2-10 GHz, with 24 antenna elements connected to a vector network analyzer via a 2×24 port matrix switch. Through the use of two different nonlinear reconstruction schemes: the Multiplicative-Regularized Contrast Source Inversion method and an enhanced version of the Distorted Born Iterative Method, we show preliminary imaging results from dielectric phantoms where data were collected from 3-6 GHz. The early inversion results show that the system is capable of quantitatively reconstructing dielectric objects.

- **CP-V** [107]: Majid Ostadrahimi, Rayan Reopelle, Sima Noghanian, Stephen Pistorius, Arman Vahedi, and Faezeh Safari, "A heterogeneous breast phantom for microwave breast imaging," *IEEE Engineering in Medicine and Biology Society (EMBS)*, Minneapolis, Minnesota, USA, September, 2009.

  Abstract: Recently there has been a great amount of attention to imaging the biological tissues using microwave radiation. In order to verify microwave imaging algorithms, realistic body models are needed to measure and simulate the penetration of microwave energy into the tissue and also reconstruct the image. In this study, a phantom is created which its dielectric properties are close to the properties of the real breast tissue. The proposed phantom includes materials that resemble skin, fat, gland and tumor tissues. The phantom is

fabricated out of materials that are widely available and easy to make. In addition the elasticity of the materials enables us to shape the phantom in a two dimensional (2D) or three dimensional (3D) forms.

- **CP-VI** [35]: Majid Ostadrahimi, Sima Noghanian, and Lotfollah Shafai, "On the accuracy of two dimensional solvers for three dimensional imaging," *IEEE International Symposium on Antennas and Propagation (AP-S)*, North Charleston, South Carolina, USA, June, 2009.

  Abstract: Microwave Imaging (MI) has been used for non-destructive testing and biomedical imaging. MI is a non-linear ill-posed inverse scattering problem. In the past several two dimensional (2D) and three dimensional (3D) methods are presented to provide a 3D image of the unknown object. Reconstructing a 3D image from slices of 2D images is attractive due to its less computational requirements. However, the accuracy of the 3D image obtained using 2D slices is under questions, especially when the dielectric properties of the objects is not uniform. In this paper the 2D and 3D scattering problems are investigated. It is shown that only for special cases; these two methods provide the same unique answer. The level of error for other cases is investigated. In MI, both plane wave and infinite line sources are important. In this paper the line source excitation is considered. The results and the detailed proof will be provided during the presentation at the conference.

- **CP-VII** [62]: Majid Ostadrahimi, Sima Noghanian, and Lotfollah Shafai, "A modified double layer tapered slot antenna with improved cross polarization," *13th International Symposium on Antenna Technology and Applied Electromagnetics (ANTEM)*, Banff, Alberta, Canada, February, 2009.

  Abstract: A method for improving polarization purity of the Tapered Slot Antenna (TSA) is investigated. The conventional TSA antenna and the proposed new design are investigated. Simulation and measurement results show a significant improvement in the cross polarization level of the proposed geometry, within a wide frequency bandwidth.

References

[1] I. Newton, "Letter to robert hooke," http://en.wikiquote.org/wiki/Isaac_Newton, February 1676.

[2] A. Abubakar, T. Habashy, V. Druskin, L. Knizhnerman, and D. Alumbaugh, "2.5 D forward and inverse modeling for interpreting low-frequency electromagnetic measurements," *Geophysics*, vol. 73, p. F165, 2008.

[3] E. Marengo, R. Hernandez, and H. Lev-Ari, "Intensity-only signal-subspace-based imaging," *JOSA A*, vol. 24, no. 11, pp. 3619–3635, 2007.

[4] R. Zoughi, *Microwave non-destructive testing and evaluation*. Springer Us, 2000.

[5] A. Abubakar and P. Van Den Berg, "Non-linear three-dimensional inversion of cross-well electrical measurements," *Geophysical prospecting*, vol. 48, no. 1, pp. 109–134, 2000.

[6] P. Meaney, M. Fanning, D. Li, S. Poplack, and K. Paulsen, "A clinical prototype for active microwave imaging of the breast," *Microwave Theory and Techniques, IEEE Transactions on*, vol. 48, no. 11, pp. 1841 – 1853, Nov. 2000.

[7] S. Semenov, "Microwave tomography: review of the progress towards clinical applications," *Philosophical transactions. Series A, Mathematical, physical, and engineering sciences*, vol. 367, no. 1900, p. 3021, 2009.

[8] A. R. Webb, *Introduction to biomedical imaging*. Wiley-Interscience, 2003.

[9] P. Gøtzsche and M. Nielsen, "Screening for breast cancer with mammography (review)," *Cochrane Database of Systematic Reviews*, pp. 1–90, 2009.

[10] P. Meaney, M. Fanning, T. Raynolds, C. Fox, Q. Fang, C. Kogel, S. Poplack, and K. Paulsen, "Initial clinical experience with microwave breast imaging in women with normal mammography," *Academic Radiology*, vol. 14, no. 2, pp. 207–218, 2007.

[11] T. Rubæk, O. Kim, and P. Meincke, "Computational validation of a 3-D microwave imaging system for breast-cancer screening," *Antennas and Propagation, IEEE Transactions on*, vol. 57, no. 7, pp. 2105–2115, 2009.

[12] S. Hagness, A. Taflove, and J. Bridges, "Two-dimensional fdtd analysis of a pulsed microwave confocal system for breast cancer detection: Fixed-focus and

antenna-array sensors," *Biomedical Engineering, IEEE Transactions on*, vol. 45, no. 12, pp. 1470–1479, 1998.

[13] E. Fear, X. Li, S. Hagness, and M. Stuchly, "Confocal microwave imaging for breast cancer detection: Localization of tumors in three dimensions," *Biomedical Engineering, IEEE Transactions on*, vol. 49, no. 8, pp. 812–822, 2002.

[14] M. Klemm, I. Craddock, J. Leendertz, A. Preece, and R. Benjamin, "Radar-based breast cancer detection using a hemispherical antenna arrayexperimental results," *Antennas and Propagation, IEEE Transactions on*, vol. 57, no. 6, pp. 1692–1704, 2009.

[15] D. Winters, J. Shea, E. Madsen, G. Frank, B. Van Veen, and S. Hagness, "Estimating the breast surface using UWB microwave monostatic backscatter measurements," *Biomedical Engineering, IEEE Transactions on*, vol. 55, no. 1, pp. 247–256, 2008.

[16] X. Li, E. Bond, B. Van Veen, and S. Hagness, "An overview of ultra-wideband microwave imaging via space-time beamforming for early-stage breast-cancer detection," *Antennas and Propagation Magazine, IEEE*, vol. 47, no. 1, pp. 19–34, 2005.

[17] Q. Fang, P. Meaney, and K. Paulsen, "Viable three-dimensional medical microwave tomography: theory and numerical experiments," *Antennas and Propagation, IEEE Transactions on*, vol. 58, no. 2, pp. 449–458, 2010.

[18] T. Habashy, R. Groom, and B. Spies, "Beyond the Born and Rytov approximations: A nonlinear approach to electromagnetic scattering," *Journal of Geophysical Research*, vol. 98, no. B2, pp. 1759–1775, 1993.

[19] Y. Wang and W. Chew, "An iterative solution of the two-dimensional electromagnetic inverse scattering problem," *International Journal of Imaging Systems and Technology*, vol. 1, no. 1, pp. 100–108, 1989.

[20] W. Chew and Y. Wang, "Reconstruction of two-dimensional permittivity distribution using the distorted born iterative method," *Medical Imaging, IEEE Transactions on*, vol. 9, no. 2, pp. 218–225, 1990.

[21] N. Joachimowicz, C. Pichot, and J. Hugonin, "Inverse scattering: An iterative numerical method for electromagnetic imaging," *Antennas and Propagation, IEEE Transactions on*, vol. 39, no. 12, pp. 1742–1753, 1991.

[22] P. Mojabi, "Investigation and development of algorithms and techniques for microwave tomography," Ph.D. dissertation, University of Manitoba, Winnipeg, MB, 2010.

[23] C. Gilmore, "Towards an improved microwave tomography system," Ph.D. dissertation, University of Manitoba, Winnipeg, MB, 2009.

[24] J. Jacobi, L. Larsen, and C. Hast, "Water-immersed microwave antennas and their application to microwave interrogation of biological targets," *Microwave Theory and Techniques, IEEE Transactions on*, vol. 27, no. 1, pp. 70–78, 1979.

[25] L. Larsen and J. Jacobi, "Microwave scattering parameter imagery of an isolated canine kidney," *Medical Physics*, vol. 6, p. 394, 1979.

[26] J. Bolomey, L. Jofre, and G. Peronnet, "On the possible use of microwave-active imaging for remote thermal sensing," *Microwave Theory and Techniques, IEEE Transactions on*, vol. 31, no. 9, pp. 777–781, 1983.

[27] J. Bolomey and C. Pichot, "Microwave tomography: from theory to practical imaging systems," *International Journal of Imaging Systems and Technology*, vol. 2, no. 2, pp. 144–156, 1990.

[28] L. Jofre, M. Hawley, A. Broquetas, E. de los Reyes, M. Ferrando, and A. Elias-Fuste, "Medical imaging with a microwave tomographic scanner," *Biomedical Engineering, IEEE Transactions on*, vol. 37, no. 3, pp. 303–312, 1990.

[29] D. Lynch, K. Paulsen, and J. Strohbehn, "Hybrid element method for unbounded electromagnetic problems in hyperthermia," *International journal for numerical methods in engineering*, vol. 23, no. 10, pp. 1915–1937, 1986.

[30] K. Paulsen, M. Moskowitz, and T. Ryan, "Temperature field estimation using electrical impedance profiling methods. i. reconstruction algorithm and simulated results," *International journal of hyperthermia*, vol. 10, no. 2, pp. 209–228, 1994.

[31] P. Meaney, K. Paulsen, A. Hartov, and R. Crane, "An active microwave imaging system for reconstruction of 2-D electrical property distributions," *Biomedical Engineering, IEEE Transactions on*, vol. 42, no. 10, pp. 1017–1026, 1995.

[32] S. Semenov, R. Svenson, A. Boulyshev, A. Souvorov, V. Borisov, Y. Sizov, A. Starostin, K. Dezern, G. Tatsis, and V. Baranov, "Microwave tomography: two-dimensional system for biological imaging," *Biomedical Engineering, IEEE Transactions on*, vol. 43, no. 9, pp. 869–877, 1996.

[33] J. Geffrin, P. Sabouroux, and C. Eyraud, "Free space experimental scattering database continuation: experimental set-up and measurement precision," *inverse Problems*, vol. 21, p. S117, 2005.

[34] J. Geffrin and P. Sabouroux, "Continuing with the Fresnel database: experimental setup and improvements in 3D scattering measurements," *Inverse Problems*, vol. 25, p. 024001, 2009.

[35] M. Ostadrahimi, S. Noghanian, and L. Shafai, "On the accuracy of two dimensional solvers for three dimensional imaging," in *Antennas and Propagation Society International Symposium, 2009. APSURSI'09. IEEE*. IEEE, pp. 1–4.

[36] R. F. Harrington, *Time-harmonic electromagnetic fields*. New York: IEEE Press : Wiley-Interscience, 2001.

[37] C. A. Balanis, *Advanced engineering electromagnetics*. New York: Wiley, 1989.

[38] R. Kress, *Linear integral equations*. Springer Verlag, 1999.

[39] M. Pastorino, *Microwave imaging*. Wiley, 2010, vol. 208.

[40] A. Devaney, "A computer simulation study of diffraction tomography," *Biomedical Engineering, IEEE Transactions on*, no. 7, pp. 377–386, 1983.

[41] J. De Zaeytijd, A. Franchois, C. Eyraud, and J. Geffrin, "Full-wave three-dimensional microwave imaging with a regularized gauss–newton methodtheory and experiment," *Antennas and Propagation, IEEE Transactions on*, vol. 55, no. 11, pp. 3279–3292, 2007.

[42] P. Mojabi and J. LoVetri, "Microwave biomedical imaging using the multiplicative regularized gauss-newton inversion," *Antennas and Wireless Propagation Letters, IEEE*, vol. 8, pp. 645–648, 2009.

[43] A. Massa, D. Franceschini, G. Franceschini, M. Pastorino, M. Raffetto, and M. Donelli, "Parallel ga-based approach for microwave imaging applications," *Antennas and Propagation, IEEE Transactions on*, vol. 53, no. 10, pp. 3118–3127, 2005.

[44] P. Van Den Berg and R. Kleinman, "A contrast source inversion method," *Inverse problems*, vol. 13, p. 1607, 1997.

[45] A. Abubakar, P. Van den Berg, and J. Mallorqui, "Imaging of biomedical data using a multiplicative regularized contrast source inversion method," *Microwave Theory and Techniques, IEEE Transactions on*, vol. 50, no. 7, pp. 1761–1771, 2002.

[46] C. Gilmore, P. Mojabi, and J. LoVetri, "Comparison of an enhanced distorted born iterative method and the multiplicative-regularized contrast source inversion method," *Antennas and Propagation, IEEE Transactions on*, vol. 57, no. 8, pp. 2341–2351, 2009.

[47] P. Meaney, K. Paulsen, A. Hartov, and R. Crane, "Microwave imaging for tissue assessment: Initial evaluation in multitarget tissue-equivalent phantoms," *Biomedical Engineering, IEEE Transactions on*, vol. 43, no. 9, pp. 878–890, 1996.

[48] N. Joachimowicz, J. Mallorqui, J. Bolomey, and A. Broquets, "Convergence and stability assessment of Newton-Kantorovich reconstruction algorithms for microwave tomography," *Medical Imaging, IEEE Transactions on*, vol. 17, no. 4, pp. 562–570, 1998.

[49] S. Semenov, A. Bulyshev, A. Abubakar, V. Posukh, Y. Sizov, A. Souvorov, P. van den Berg, and T. Williams, "Microwave-tomographic imaging of the high dielectric-contrast objects using different image-reconstruction approaches," *Microwave Theory and Techniques, IEEE Transactions on*, vol. 53, no. 7, pp. 2284–2294, 2005.

[50] P. Gibson, "The vivaldi aerial," in *Microwave Conference, 1979. 9th European*. IEEE, 1979, pp. 101–105.

[51] L. Lewis, M. Fassett, and J. Hunt, "A broadband stripline array element," in *Antennas and Propagation Society International Symposium, 1974*, vol. 12. IEEE, 1974, pp. 335–337.

[52] C. A. Balanis, *Antenna theory : analysis and design*. Hoboken, NJ: John Wiley, 2005.

[53] K. Yngvesson, D. Schaubert, T. Korzeniowski, E. Kollberg, and T. Thungren, "Endfire tapered slot antennas on dielectric substrates," *IEEE transactions on antennas and propagation*, vol. 33, pp. 1392–1400, 1985.

[54] K. Yngvesson, T. Korzeniowski, Y. Kim, E. Kollberg, and J. Johansson, "The tapered slot antenna-a new integrated element for millimeter-wave applications," *Microwave Theory and Techniques, IEEE Transactions on*, vol. 37, no. 2, pp. 365–374, 1989.

[55] R. Simons and R. Lee, "On-wafer characterization of millimeter-wave antennas for wireless applications," *Microwave Theory and Techniques, IEEE Transactions on*, vol. 47, no. 1, pp. 92–96, 1999.

[56] E. Guillanton, J. Dauvignac, C. Pichot, and J. Cashman, "A new design tapered slot antenna for ultra-wideband applications," *Microwave and optical technology letters*, vol. 19, no. 4, pp. 286–289, 1998.

[57] J. Zhang, E. Fear, and R. Johnston, "Cross-Vivaldi antenna for breast tumor detection," *Microwave and Optical Technology Letters*, vol. 51, no. 2, pp. 275–280, 2009.

[58] D. Woten, M. Hajihashemi, A. Hassan, and M. El-Shenawee, "Experimental microwave validation of level set reconstruction algorithm," *Antennas and Propagation, IEEE Transactions on*, vol. 58, no. 1, pp. 230–233, 2010.

[59] J. Bourqui, M. Okoniewski, and E. Fear, "Balanced antipodal Vivaldi antenna with dielectric director for near-field microwave imaging," *Antennas and Propagation, IEEE Transactions on*, vol. 58, no. 7, pp. 2318–2326, 2010.

[60] A. Abbosh, H. Kan, and M. Bialkowski, "Compact ultra-wideband planar tapered slot antenna for use in a microwave imaging system," *Microwave and optical technology letters*, vol. 48, no. 11, pp. 2212–2216, 2006.

[61] J. Langley, P. Hall, and P. Newham, "Novel ultrawide-bandwidth vivaldi antenna with low crosspolarisation," *Electronics letters*, vol. 29, no. 23, pp. 2004–2005, 1993.

[62] M. Ostadrahimi, S. Noghanian, and L. Shafai, "A modified double layer tapered slot antenna with improved cross polarization," in *Antenna Technology and Applied Electromagnetics and the Canadian Radio Science Meeting, 2009. ANTEM/URSI 2009. 13th International Symposium on*. IEEE, 2009, pp. 1–4.

[63] "Ansoft-hfss simulator package," May 2011. [Online]. Available: www.ansoft.com

[64] D. M. Pozar, *Microwave engineering*. Hoboken, NJ: J. Wiley, 2005, david M. Pozar.; Includes bibliographical references and index.

[65] M. Ostadrahimi, S. Noghanian, L. Shafai, A. Zakaria, C. Kaye, and J. LoVetri, "Investigating a double layer vivaldi antenna design for fixed array field measurement," *International Journal of Ultra Wideband Communications and Systems*, vol. 1, no. 4, pp. 282–290, 2010.

[66] C. R. Paul and Knovel, *Analysis of multiconductor transmission lines*. Wiley-Interscience, 1994, clayton Paul; Includes bibliographical references and index.

[67] "Multiphysics modeling and simulation software (comsol)," May 2011. [Online]. Available: http://www.comsol.com/

[68] B. Schiek and J. Kohler, "An Improved Microstrip-to-Microslot Transition (Letters)," *Microwave Theory and Techniques, IEEE Transactions on*, vol. 24, no. 4, pp. 231–233, 1976.

[69] A. Lai, A. Sinopoli, and W. Burnside, "A novel antenna for ultra-wide-band applications," *Antennas and Propagation, IEEE Transactions on*, vol. 40, no. 7, pp. 755–760, 1992.

[70] C. Gilmore, P. Mojabi, A. Zakaria, M. Ostadrahimi, C. Kaye, S. Noghanian, L. Shafai, S. Pistorius, and J. LoVetri, "A wideband microwave tomography system with a novel frequency selection procedure," *Biomedical Engineering, IEEE Transactions on*, vol. 57, no. 4, pp. 894–904, 2010.

[71] X. Li, S. Davis, S. Hagness, D. Van Der Weide, and B. Van Veen, "Microwave imaging via space-time beamforming: Experimental investigation of tumor detection in multilayer breast phantoms," *Microwave Theory and Techniques, IEEE Transactions on*, vol. 52, no. 8, pp. 1856–1865, 2004.

[72] S. Semenov, J. Kellam, Y. Sizov, A. Nazarov, T. Williams, B. Nair, A. Pavlovsky, V. Posukh, and M. Quinn, "Microwave tomography of extremities: 1. dedicated 2d system and physiological signatures," *Physics in Medicine and Biology*, vol. 56, p. 2005, 2011.

[73] P. Mojabi and J. LoVetri, "Comparison of TE and TM inversions in the framework of the Gauss-Newton method," *Antennas and Propagation, IEEE Transactions on*, vol. 58, no. 4, pp. 1336–1348, 2010.

[74] L. Crocco, M. D'Urso, and T. Isernia, "Testing the contrast source extended born inversion method against real data: the tm case," *Inverse problems*, vol. 21, p. S33, 2005.

[75] T. Henriksson, N. Joachimowicz, C. Conessa, and J. Bolomey, "Quantitative microwave imaging for breast cancer detection using a planar 2.45 ghz system," *Instrumentation and Measurement, IEEE Transactions on*, vol. 59, no. 10, pp. 2691–2699, 2010.

[76] P. Meaney, K. Paulsen, and J. Chang, "Near-field microwave imaging of biologically-based materials using a monopole transceiver system," *Microwave Theory and Techniques, IEEE Transactions on*, vol. 46, no. 1, pp. 31–45, 1998.

[77] S. Semenov, R. Svenson, A. Bulyshev, A. Souvorov, A. Nazarov, Y. Sizov, V. Posukh, A. Pavlovsky, P. Repin, and G. Tatsis, "Spatial resolution of microwave tomography for detection of myocardial ischemia and infarction-experimental study on two-dimensional models," *Microwave Theory and Techniques, IEEE Transactions on*, vol. 48, no. 4, pp. 538–544, 2000.

[78] A. Yaghjian, "An overview of near-field antenna measurements," *Antennas and Propagation, IEEE Transactions on*, vol. 34, no. 1, pp. 30–45, 1986.

[79] R. Justice and V. Rumsey, "Measurement of electric field distributions," *Antennas and Propagation, IRE Transactions on*, vol. 3, no. 4, pp. 177–180, 1955.

[80] A. Cullen and J. Parr, "A new perturbation method for measuring microwave fields in free space," *Proceedings of the IEE-Part B: Radio and Electronic Engineering*, vol. 102, no. 6, pp. 836–844, 1955.

[81] R. Harrington, "Small resonant scatterers and their use for field measurements," *Microwave Theory and Techniques, IRE Transactions on*, vol. 10, no. 3, pp. 165–174, 1962.

[82] H. Memarzadeh-Tehran, J. Laurin, and R. Kashyap, "Optically modulated probe for precision near-field measurements," *Instrumentation and Measurement, IEEE Transactions on*, vol. 59, no. 10, pp. 2755–2762, 2010.

[83] J. Richmond, "A modulated scattering technique for measurement of field distributions," *Microwave Theory and Techniques, IRE Transactions on*, vol. 3, no. 4, pp. 13–15, 1955.

[84] J. Bolomey and F. Gardiol, *Engineering applications of the modulated scatterer technique*. Artech House Publishers, 2001.

[85] R. J. King, *Microwave homodyne systems*. Stevenage, Eng.: P. Peregrinus on behalf of the Institution of Electrical Engineers, 1978, vol. 3.

[86] E. C. Jordan, *Electromagnetic Waves and Radiating Systems*. Englewood Cliffs, N.J.: Prentice-Hall, 1964, x, 710 P. Diagrs; Includes Bibliography.

[87] R. E. Collin, *Antennas and radiowave propagation*. New York: McGraw-Hill, 1985.

[88] M. Ghasr, M. Abou-Khousa, S. Kharkovsky, R. Zoughi, and D. Pommerenke, "A novel 24 ghz one-shot, rapid and portable microwave imaging system," in *Instrumentation and Measurement Technology Conference Proceedings, 2008. IMTC 2008. IEEE*. IEEE, 2008, pp. 1798–1802.

[89] M. Ostadrahimi, P. Mojabi, S. Noghanian, L. Shafai, S. Pistorius, and J. LoVetri, "A novel microwave tomography system based on the scattering probe technique," *Instrumentation and Measurement, IEEE Transactions on*, vol. PP, no. 99, pp. 1 –12, 2011.

[90] C. Gilmore, P. Mojabi, A. Zakaria, S. Pistorius, and J. LoVetri, "On super-resolution with an experimental microwave tomography system," *Antennas and Wireless Propagation Letters, IEEE*, vol. 9, pp. 393–396, 2010.

[91] A. Abubakar, P. van den Berg, and S. Semenov, "A robust iterative method for born inversion," *Geoscience and Remote Sensing, IEEE Transactions on*, vol. 42, no. 2, pp. 342–354, 2004.

[92] F. Miller, *Thomas A. Edison, Benefactor of mankind; the romantic life story of the world's greatest inventor*. Kessinger Publishing, 2005.

[93] R. Bansal, *Handbook of engineering electromagnetics*. New York: Marcel Dekker, 2004.

[94] C. Gabriel, S. Gabriel, and E. Corthout, "The dielectric properties of biological tissues: I. literature survey," *Physics in Medicine and Biology*, vol. 41, p. 2231, 1996.

[95] S. Gabriel, R. Lau, and C. Gabriel, "The dielectric properties of biological tissues: Ii. measurements in the frequency range 10 hz to 20 ghz," *Physics in Medicine and Biology*, vol. 41, p. 2251, 1996.

[96] ——, "The dielectric properties of biological tissues: Iii. parametric models for the dielectric spectrum of tissues," *Physics in medicine and biology*, vol. 41, p. 2271, 1996.

[97] M. Lazebnik, L. McCartney, D. Popovic, C. Watkins, M. Lindstrom, J. Harter, S. Sewall, A. Magliocco, J. Booske, M. Okoniewski *et al.*, "A large-scale study of the ultrawideband microwave dielectric properties of normal breast tissue obtained from reduction surgeries," *Physics in Medicine and Biology*, vol. 52, p. 2637, 2007.

[98] M. Lazebnik, D. Popovic, L. McCartney, C. Watkins, M. Lindstrom, J. Harter, S. Sewall, T. Ogilvie, A. Magliocco, T. Breslin *et al.*, "A large-scale study of the ultrawideband microwave dielectric properties of normal, benign and malignant breast tissues obtained from cancer surgeries," *Physics in Medicine and Biology*, vol. 52, p. 6093, 2007.

[99] R. Halter, T. Zhou, P. Meaney, A. Hartov, J. Richard Jr, K. Rosenkranz, W. Wells, C. Kogel, A. Borsic, E. Rizzo *et al.*, "The correlation of in vivo and ex vivo tissue dielectric properties to validate electromagnetic breast imaging: initial clinical experience," *Physiological measurement*, vol. 30, p. S121, 2009.

[100] P. Liu, C. Rappaport, Y. Wei, and S. Sridhar, "Simulated biological materials at microwave frequencies for the study of electromagnetic hyperthermia," in *Engineering in Medicine and Biology Society, 1988. Proceedings of the Annual International Conference of the IEEE*, vol. 1. IEEE, 1992, pp. 272–273.

[101] D. Andreuccetti, M. Bini, A. Ignesti, R. Olmi, N. Rubino, and R. Vanni, "Use of polyacrylamide as a tissue-equivalent material in the microwave range," *Biomedical Engineering, IEEE Transactions on*, vol. 35, no. 4, pp. 275–277, 1988.

[102] M. Lazebnik, E. Madsen, G. Frank, and S. Hagness, "Tissue-mimicking phantom materials for narrowband and ultrawideband microwave applications," *Physics in medicine and biology*, vol. 50, p. 4245, 2005.

[103] J. Croteau, J. Sill, T. Williams, and E. Fear, "Phantoms for testing radar-based microwave breast imaging," in *Antenna Technology and Applied Electromagnetics and the Canadian Radio Science Meeting, 2009. ANTEM/URSI 2009. 13th International Symposium on.* IEEE, 2009, pp. 1–4.

[104] E. Madsen, M. Hobson, G. Frank, H. Shi, J. Jiang, T. Hall, T. Varghese, M. Doyley, and J. Weaver, "Anthropomorphic breast phantoms for testing elastography systems," *Ultrasound in medicine & biology*, vol. 32, no. 6, pp. 857–874, 2006.

[105] D. Li, P. Meaney, and K. Paulsen, "Conformal microwave imaging for breast cancer detection," *Microwave Theory and Techniques, IEEE Transactions on*, vol. 51, no. 4, pp. 1179–1186, 2003.

[106] A. Nyshadham, C. Sibbald, and S. Stuchly, "Permittivity measurements using open-ended sensors and reference liquid calibration-an uncertainty analysis," *Microwave Theory and Techniques, IEEE Transactions on*, vol. 40, no. 2, pp. 305–314, 1992.

[107] M. Ostadrahimi, R. Reopelle, S. Noghanian, S. Pistorius, A. Vahedi, and F. Safari, "A heterogeneous breast phantom for microwave breast imaging," in *31st Annual International Conference of the IEEE Engineering in Medicine and Biology Society (EMBC).* IEEE, 2009, pp. 2727–2730.

[108] A. Sabouni, S. Noghanian, and S. Pistorius, "Water content and tissue composition effects on microwave tomography results," in *Applied Computational Electromagnetics Society (ACES) Conference*, Niagara Falls, Canada, 2008.

[109] M. Ostadrahimi, P. Mojabi, S. Noghanian, J. LoVetri, and L. Shafai, "A multiprobe-per-collector modulated scatterer technique for microwave tomography," *Antennas and Wireless Propagation Letters, IEEE*, vol. 10, pp. 1445 –1448, 2011.

[110] M. Ostadrahimi, P. Mojabi, C. Gilmore, A. Zakaria, S. Noghanian, S. Pistorius, and J. LoVetri, "Analysis of incident field modeling and incident/scattered field calibration techniques in microwave tomography," *Antennas and Wireless Propagation Letters, IEEE*, vol. 10, pp. 900–903, 2011.

[111] M. Ostadrahimi, S. Noghanian, and L. Shafai, "A novel antenna design technique using finite element method and transmission line theory," *Microwave and Optical Technology Letters*, vol. 54, no. 1, pp. 126–133, 2012.

[112] C. Gilmore, P. Mojabi, A. Zakaria, M. Ostadrahimi, C. Kaye, S. Noghanian, L. Shafai, S. Pistorius, and J. LoVetri, "An ultra-wideband microwave tomography system: preliminary results," in *Engineering in Medicine and Biology Society, 2009. EMBC 2009. Annual International Conference of the IEEE.* IEEE, 2009, pp. 2288–2291.